SLIDING MODE CONTROL STRATEGIES FOR ROBOTIC SYSTEMS

by

Aritra Mitra
(13104019)

DEPARTMENT OF ELECTRICAL ENGINEERING

INDIAN INSTITUTE OF TECHNOLOGY KANPUR
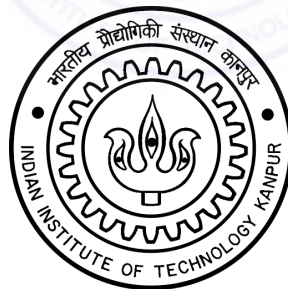
July, 2015

SLIDING MODE CONTROL STRATEGIES FOR ROBOTIC SYSTEMS

A Thesis Submitted

in Partial Fulfilment of the Requirements
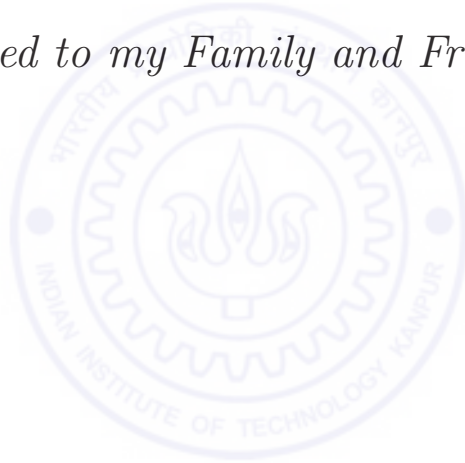
for the Degree of

MASTER OF TECHNOLOGY

by

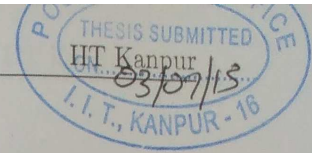## Aritra Mitra

(13104019)

DEPARTMENT OF ELECTRICAL ENGINEERING

INDIAN INSTITUTE OF TECHNOLOGY KANPUR

July, 2015
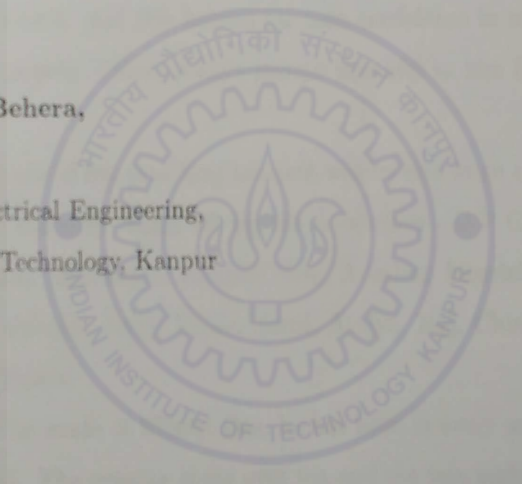
Dedicated to my Family and Friends

CERTIFICATE

It is certified that the work contained in this thesis entitled "*Sliding Mode Control Strategies for Robotic Systems*", by Mr. Aritra Mitra (Roll No. 13104019), has been carried out under my supervision and this work has not been submitted elsewhere for a degree.

July, 2015

IIT Kanpur

Dr. Laxmidhar Behera,

Professor,

Department of Electrical Engineering,

Indian Institute of Technology, Kanpur

Kanpur, 208016.

ACKNOWLEDGEMENTS

to her mere presence, which I believe has done wonders to my life. She has lent a patient ear to all my troubles, and her constant humour and lively spirit has kept me going at all times. I have no words to express my gratitude towards her.

Aritra Mitra

July, 2015

ABSTRACT

In this thesis, we investigate the feasibility of applying Sliding Mode Control (SMC), one of the best known robust control techniques, to two applications - Targeted drug delivery inside the human body using a ferromagnetic micro-robot steered by a MRI, and Modeling and Control of a 4 Degree of Freedom (DOF) Barrett Whole Arm Manipulator (WAM). It is extremely difficult to obtain exact mathematical models of each of the systems under study, leading to unavoidable modeling errors. The problem statement for both the applications can be formulated as trajectory tracking problems of nonlinear dynamical systems with uncertainties. This motivates the use of SMC.

First, we develop an Adaptive Fuzzy Sliding Mode Control (AFSMC) scheme for the MRI based drug delivery system, based on a highly nonlinear model available in literature. Simulation results illustrate that the proposed technique is able to reject disturbances, and achieve perfect tracking of the micro-robot along the centre line of a blood vessel. The 'chattering' phenomenon observed in conventional SMC is completely eliminated. Another significant merit of this framework, is its ability to estimate the dielectric density of blood on-line. Comparisons are drawn with a state-of-the-art backstepping approach.

Next, we develop a rigid body model of a 4 DOF Barrett WAM using the recursive Newton-Euler technique. This is a major contribution as Barrett does not disclose its dynamic model. The precision achieved in rigorous trajectory tracking experiments performed in the joint space, validates the accuracy of the developed model. A variant of SMC, known as Nonsingular Fast Terminal SMC (NFTSMC), which guarantees fast finite-time convergence of the error trajectories to zero, has also been proposed for control of the WAM. We derive an analytical expression for the error settling time and demonstrate that the NFTSMC indeed guarantees faster performance as compared to a standard Nonsingular Terminal SMC (NTSMC). A detailed comparative study of simulation and experimental results is presented.

Finally, aiming to integrate the robustness of SMC with optimal control theory, we integrate conventional SMC with Adaptive Dynamic Programming, to obtain a novel optimal sliding mode control framework. We present the general design procedure, stability analysis, and simulation results for both regulation and tracking problems, the latter being performed on a simplified model of the MRI guided micro-robot system.

Contents

x

List of Tables

List of Figures

Chapter 1

Introduction

1.0.1 Motivation

Often, it is difficult to derive an exact mathematical model for a real physical system. This is mainly because some of the parameters of the system might be unknown, or part of the system dynamics is difficult to model, leading to simplifying approximations, or the system might be subject to disturbances which are difficult to estimate. Since its inception in the 1950's, Sliding Mode Control (SMC) has been widely used by researchers in a variety of applications, owing to its robustness against a large class of perturbations or model uncertainties. It is a discontinuous feedback control strategy which often requires a reduced amount of information in comparison to classical control techniques and also holds the potential of stabilizing some nonlinear systems (such as mechanical systems with friction) which are otherwise not stabilizable by continuous state feedback laws [61].

In this thesis, motivated by these attractive features of SMC, we investigate the feasibility of applying SMC to two major applications - Automated drug delivery inside the human body using a MRI-guided micro-robot and Computed Torque Control of a 4 Degree of Freedom Barrett Whole Arm Manipulator. Finally, we attempt to develop an Optimal Sliding Mode Control scheme by drawing from the concept of Approximate Dynamic Programming, the underlying motivation being the integration of the robustness feature of conventional SMC with optimal control theory. Although the final goals of each of the two aforementioned applications are completely different, the dynamic models which represent the concerned systems have similar state space representations. Both the systems under study are extremely difficult to model exactly, leading to modeling errors and system uncertainties. In the first application, the micro-robot is expected to follow a specified path inside a human blood vessel. In the second application, each of the 4 joints

of the Barrett WAM are expected to track desired commands so as to execute a particular motion. Thus, the problem statements of each of these applications can be formulated as trajectory tracking control problems of nonlinear dynamical systems with uncertainties. Keeping these similarities in mind, the robust control techniques developed in this thesis will be applicable to each of the two systems under consideration. Specifically, the main contributions of this thesis are:

1. Development of an Adaptive Fuzzy Sliding Mode Control (AFSMC) scheme for steering a ferromagnetic micro-robot inside the human blood vessel using the magnetic field generated by an MRI. The developed scheme achieves perfect tracking, rejects disturbances, removes the chattering phenomenon observed in conventional SMC, and is able to estimate a key uncertain parameter of the model on-line.

2. Combining the Continuous Time Single Network Adaptive Critic architecture with SMC, to obtain a novel optimal sliding mode control framework. This framework can be used for both regulation and tracking problems, for a wide class of nonlinear systems with uncertainties.

3. Developing a rigid body dynamic model for 4 Degree of Freedom operation of the Barrett Whole Arm Manipulator (WAM). This is a major contribution as Barrett does not disclose the model of the WAM. However, for applying any model-based controller, knowledge of the model is necessary. The derived model is validated using rigorous experimentation. This is followed up by computed torque control using a variant of the conventional SMC known as Nonsingular Fast Terminal Sliding Mode Control (NFTSMC). This variant, which uses a nonlinear sliding surface, ensures fast finite-time convergence of the error trajectories to zero. The conventional SMC on the other hand is based on a linear sliding surface, and only guarantees asymptotic stability i.e. theoretically, the error states take infinite time to settle to zero.

1.1   Literature Survey

1.1.1   Literature in Sliding Mode Control

Over the past few decades, the concept of Sliding Mode Control has attracted a lot of attention. The concept of SMC is based on Variable Structure Systems (VSS), in which the control input switches between two control signals. The discontinuous nature of the SMC technique is its most intriguing property. This peculiar system characteristic leads

to extremely robust control systems ; often systems which are completely insensitive to parametric uncertainties in the model and external disturbances [36], [83].

In general, the dynamics of a Variable Structure Control (VSC) system consists of two modes - a 'reaching mode' or nonsliding mode, followed by a 'sliding mode' [27]. In the reaching mode, the state trajectories are driven by an appropriately designed variable structure controller, from anywhere in the phase plane, towards a sub-manifold of the state space, known as the switching manifold or sliding manifold. This is achieved in finite time. This is followed by the sliding mode, which is characterized by asymptotic convergence of the state trajectories to the equilibrium state of the system. Once the system states reach the sliding manifold, the system dynamics remain invariant to a class of parameter uncertainties and disturbances (specifically known as 'matched disturbances'). This so called 'invariance' property of sliding mode control is its main advantage. Once the matching conditions are met, the invariance property holds true for systems represented by both linear and nonlinear high-order differential equations [36].

The basic ideas of sliding mode control can be illustrated by considering a simple example. Let us take the example of a simple second-order nonlinear system represented by the following differential equations

$$\dot{x}_1 = x_2$$
$$\dot{x}_2 = -x_1^3 + u \tag{1.1.1}$$

Let the control problem be the regulation of the state x_1 to the origin. Let the output be $y = x_1$; thus, the output error is $e = x_1$. The switching function for this system is defined as

$$s = \dot{e} + ce, \tag{1.1.2}$$

where c is a positive constant. Assuming the existence of the sliding mode, once the state trajectory is brought to the sliding manifold $s = 0$, the system dynamics is represented by the following first-order differential equation

$$\dot{e} + ce = 0 \tag{1.1.3}$$

The solution of the above differential equation gives $e(t) = e(t_0)\exp[-c(t - t_0)]$. This shows that for $c > 0$, the system's output error $e(t)$ exponentially converges to zero. The condition for existence of the sliding mode is defined as

$$s\dot{s} \leq 0 \tag{1.1.4}$$

The condition for existence of the sliding mode (1.1.4), leads to the design of a discontinuous control u, which switches between two control values, and drives the system states to the sliding manifold. For the system (1.1.1), the sliding condition is satisfied by the following choice of control law

$$u = x_1^3 - cx_2 - Msgn(s), \tag{1.1.5}$$

where M, a positive constant, is the sliding mode gain which is chosen by the designer, and $sgn(\cdot)$ is the signum function. Known bounds on the system uncertainties and disturbances facilitate the choice of M. Later on in the thesis, we will investigate in detail, the procedure to choose M based on Lyapunov stability theory. With a properly chosen M value, the existence of the sliding mode can be achieved even in the presence of modeling errors and disturbances. Figure 1.1 depicts the phase plane portrait and Figure 1.2 depicts the control effort for the system (1.1.1). The main ideas are summarized as follows

- The dynamics of the original system (1.1.1) was of second-order. However, once the sliding mode was reached, the dynamics was reduced to that of a first-order differential equation (1.1.3). In general, the sliding mode dynamics is of a lower order as compared to the dynamics of the original model.

- During the sliding mode, the system dynamics is solely governed by the structure of the sliding manifold $s = 0$, which is independent of modeling errors and disturbances. Thus robustness is guaranteed once the system trajectory is brought to the sliding surface.

- The thick band which one observes in the control input u in Figure 1.2, is representative of a phenomenon known as 'chattering', one of the major sources of criticism against the practical implementation of SMC. This phenomenon is generally thought of as a motion which oscillates about the sliding manifold. As a consequence, the control input switches at very high frequency due to the signum function typically present in a sliding mode control law. Infact, the width of the high frequency band is precisely equal to $2M$, where M is the gain associated with the signum function. This can be seen in Figure 1.2, where the band has a thickness of 10, and $M = 5$. Thus, although high gains are necessary to reject disturbances, they also lead to the problem of chattering, which in turn leads to wear and tear of actuators. A lot of research has gone into the chattering-mitigation problem. The most commonly cited technique to suppress the chattering phenomenon is the Boundary layer
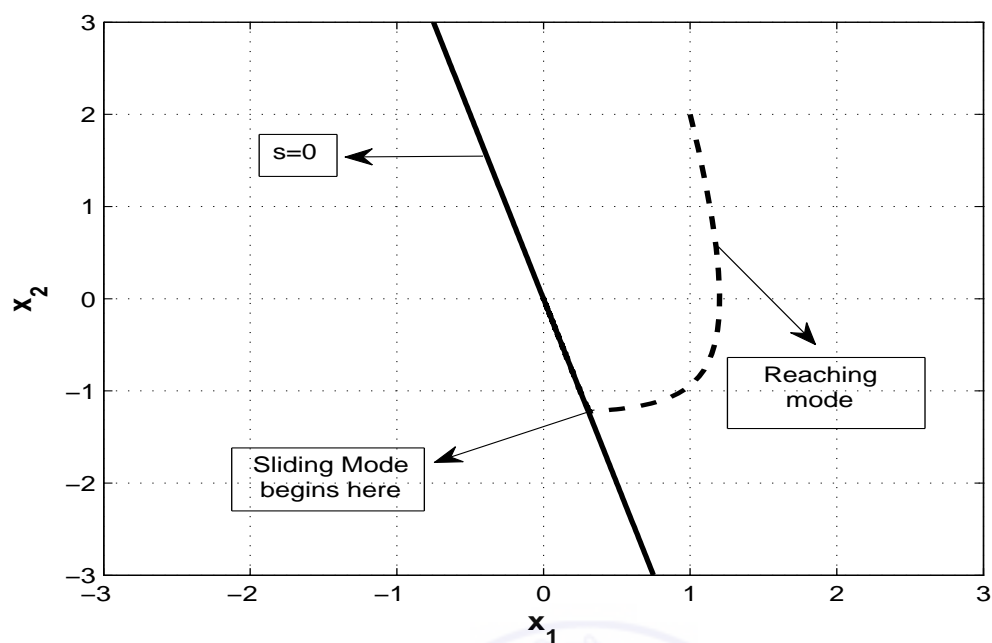
Figure 1.1: The phase plane portrait
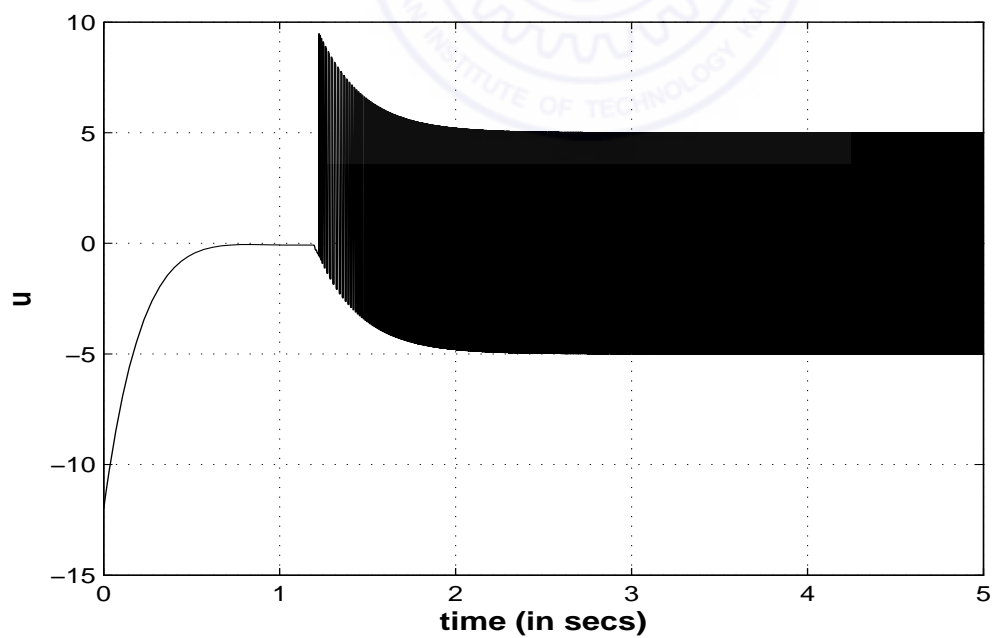
Figure 1.2: The control input

technique [16], [84]. In this approach, the switching function is approximated by a piecewise linear or smooth function. In order for the system to retain the ideal sliding mode behaviour, particularly when an unknown disturbance is to be rejected, sufficiently high gains are required. However, this method too has received criticism from many researchers, the main point of contest being that the system loses the inherent robustness associated with the sliding mode. Thus, although this approximation works favourably in many implementations, it has its own shortcomings. We will discuss another technique of chattering suppression in detail in Chapter 3.

Over the years, sliding mode control has been applied to a variety of systems, including linear systems [83], nonlinear systems [35], multi-input/multi-output systems [51], discrete-time systems [26], large-scale and infinite-dimensional systems [58], systems with input and/or state delays [44], and stochastic systems [25]. Although SMC was originally mostly used for the purpose of stabilization, its objectives have greatly extended. SMC based approaches have also been used to construct state observers [70] and distance estimators [31] .

The control algorithms developed by control engineers are implemented mostly on digital computers. This has motivated the study of Discrete Sliding Mode Control (DSMC) in the past two decades [50]. In the case of DSMC design, the control input is applied to the plant at certain sampling instants and the control effort is assumed to be constant throughout a sampling period. DSMC is one of the most active areas of research for the sliding mode community, owing to its practical relevance. In this thesis, we will confine ourselves to the use of the conventional continuous time SMC.

1.1.2 Literature in MRI-guided nano-robotic systems for therapeutic and diagnostic applications

Targeted Drug Delivery and Nano-robotics

Targeted drug delivery, also known as smart drug delivery, is the method of delivering medication to a patient in a way such that the concentration of the medication increases in certain parts of the body relative to others [52]. The main objective of a targeted drug delivery system is to prolong, localize, target and ensure a protected drug interaction with the diseased tissue. Conventional drug delivery systems such as oral ingestion or intravascular ingestion rely on systemic blood circulation for distributing the drug throughout the body. For most therapeutic agents, this often results in only a small fraction of the

drug reaching the targeted organ. This is a major reason why targeted drug delivery is preferred over the traditional drug delivery systems. Other advantages of targeted drug delivery over traditional methods include reduction in the frequency of the dosages taken by the patient, having a more uniform effect of the drug, reduction of drug side-effects, and reduced fluctuation in circulating drug levels.

Nano-robots are defined as machines composed of nano-scale components, which can be controlled at the nano-meter scale, and which respond to input forces and information [69]. These particles are conceptualised to have sizes comparable to that of human cells. Thus, if these nano-robots acquire simple functionalities to sense and target specific cells, and to release drug molecules when triggered by a control signal, then it can lead to a paradigm shift in medical research. Conducting curative and reconstructive treatment in the human body at the cellular and sub-cellular level, in a controllable manner, would then be a realizable concept [71]. Such a ground-breaking development would usher in a new era in medical diagnosis and lead to better treatment of cardiovascular diseases, diabetes and most importantly, cancerous tumours.

Over the last two decades, a variety of nano-particles and nano-vesicle technologies have been employed for diagnostic and therapeutic purposes [13, 19, 39, 57]. Although these novel methodologies possess excellent physiochemical properties, possess prolonged circulation times and improved absorption rates, they are distributed through systemic circulation, and hence suffer from poor targeting capabilities [68]. Enhancement of targeting capabilities with the aim of minimizing side-effects and improving diagnostic efficiency, necessitates the use of guidance techniques.

Control Strategies

Autonomous untethered micro-robots are a possible solution to the guidance problem. However, it is extremely difficult to embed actuators which are powerful enough to propel such robots in the human cardiovascular system, especially when the robot is swimming against the blood flow. Magnetic micro/nano-particles, equipped with sensing and actuation mechanisms, have been studied by several groups. The developed techniques mostly involved the use of static magnetic fields generated by magnets [28, 29] or superconducting magnets [15, 53] to attract the micro-particles towards the targeted region. However, all these techniques were open loop, with no tracking and no feedback mechanism. Consequently, these open loop methods had poor localization accuracy and proved to be efficient only in regions near the body surface.

This motivated the development of a precise closed-loop nano-particle localization system. In the most recent literature, spanning the development which has occurred in this field over the last decade, two methods have been advocated to achieve targeted drug delivery using magnetic micro/nano-particles - the use of external Maxwell coils [4, 5, 81] and the use of a MRI device. The MRI-based localization scheme was developed by Sylvain Martel at the Ecole Polytechnique de Montreal, Canada [14, 20, 66]. This approach has three main advantages

- It is non-invasive.

- It allows for simultaneous actuation/propulsion and tracking. Thus, a closed loop real time control scheme can be implemented.

- Commercial MRI devices are available in most hospitals.

The first systematic approach towards MRI-based guidance of functionalized nano-robot capsules began as part of the European Project NANOMA in the summer of 2008. This innovative idea is based on the concept of using the magnetic field generated by the MRI to propel the nano-particles to the target, using feedback of the position of the nano-particles, by processing the MRI image data. This navigation methodology, in combination with appropriate chemical modification of the surfaces of the nano-particles, is expected to yield a more localized and controlled treatment.

Remark - *The control objective is to determine the direction and magnitude of the magnetic field gradients to be generated by the MRI, based on position feedback obtained from MRI-imaging.*

In our work, we make use of the model proposed in [6], which takes into account wall effects, wall interactions and the Non-Newtonian behaviour of blood. This results in a highly non-linear model. The vast majority of related literature deals with synthesizing control laws using linear tools. For instance, the PID controller proposed in [66], suffered from instabilities and sensitivity to noise or to unmodeled dynamics. The backstepping approach used in [9], is the state-of-the-art control technique which has been used for this model. We will compare our results with this technique.

Comments on the size and nature of the particles

To get a more realistic feel of the particles under consideration, we present a report on the composition and sizes of the particles, which have been used in simulation and experiments so far in literature.

The list is as follows

- In 2006 [47], Martel *et al.* performed experiments on **ferromagnetic spheres made up of 1010/1020 carbon steel with a diameter of 3.14 mm**. The saturation magnetization of this alloy is $M_{sat} = 1.376 \times 10^6$ A/m with a saturating magnetizing induction of $B_{sat} = 0.734$ T. The experiment involved magnetic levitation of these spheres in a rigid cylindrical tube made up of polymethylmethacylate (PMMA) against a flow of water. The sphere was placed vertically inside the bore of a 1.5 T Siemens Magnetom Vision MRI scanner capable of producing maximum gradients of 25 mT/m. The spheres were saturated when placed inside the MRI scanner (As $B_0 = 1.5$ T $> B_{sat} = 0.734$ T). Figure 1.3 shows the setup used by Martel *et al.* for conducting their experiments.

- In 2007 [48], Martel *et al.* performed both, in vitro and in vivo experiments using **a ferromagnetic sphere made up of chrome steel, having a diameter of 1.5 mm (0.0136 grams)**. The material has a saturation magnetization of $M_{sat} = 1.35 \times 10^6$ A/m, and the MRI used was a 1.5 T MRI with a maximum magnetic field gradient of 40 mT/m. The in vitro experiment involved propulsion on a Plexiglass plate, and the in vivo experiment involved propulsion inside the carotid artery (inner diameter of 5 mm) of a living swine.

- In 2008 [66], Martel *et al.* used a simple PID controller for rectilinear navigation of a ferromagnetic sphere of **1.5 mm diameter** in a 2-D path within a pulsatile flow. The material used was **chrome steel** and the actuator was a 1.5 T MRI.

- Since 2010, Ferreira *et al.* have performed simulation studies on **ferromagnetic spheres of diameter 0.25 mm** [9, 10]. The reduction in size of the particles was possible owing to use of 3 T MRI's, having maximum magnetic field gradients of 80mT/m. Backstepping control has been used to construct the feedback law in these endeavors.

Having formed an idea about the sizes of the particles which have been reported in literature, it is important to have a clear idea of the sizes of blood vessels they are expected to navigate within. Table 1.1 lists different types of blood vessels and their respective diameters [9].
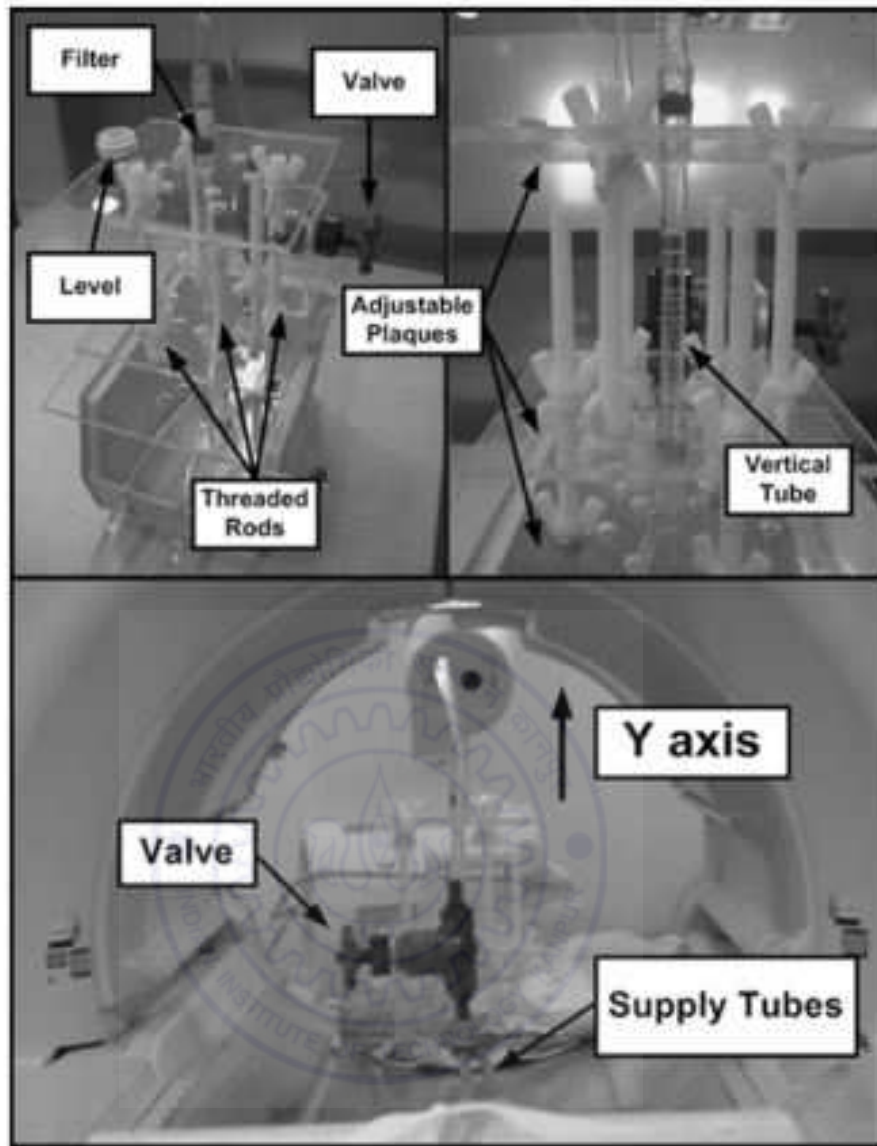
Figure 1.3: Experimental setup used by Martel *et al.* [47]

Table 1.1: Blood vessels and their diameters

Vessel	Diameter (mm)
Artery	10
Small Artery	1
Arteriole	0.1
Capillary	0.01

Remark - *From the preceding discussion, it is apparent that with the current technology available in terms of maximum magnetic field gradients which can generated by MRI's, navigation is possible in vessels no smaller than small arteries. In our study, we assume the availability of a 3 T MRI which can generate a maximum of 80 mT/m magnetic gradient. The particles under consideration will have diameters varying within 0.25-0.3 mm (ferromagnetic spheres).*

Overview of MRI-Drug Delivery System

Figure 1.4 shows the architecture of a MRI based Drug Delivery System . One can appreciate the fact that the complexity involved in implementing such a system in real time, necessitates expertise in several engineering domains. Some of the main issues in real time implementation are summarized below

- As discussed earlier, constraints on the maximum magnetic gradients that can be generated by commercial MRI's, puts a limit on the size of ferromagnetic particles which can be used for navigation. At lower scales, it is necessary to use additional coils to supply higher gradients.

- Spatial resolutions of current medical imaging techniques is also a limitation [67,89]. The image processing module needs to be designed in a way such that communication latencies and delays are avoided. In [46], the authors have implemented a tracking routine in real time within 20 ms.

- Imaging and propulsion cannot be done simultaneously. Hence, it is necessary to have a time-division-multiplexing scheme.

- Typically, the cooling system for the gradient coils of a MRI are designed for imaging purpose only. Propulsion requires the MRI coils to work at maximum amplitudes and higher duty cycles. The excess heat generated due to propulsion cannot be evacuated by the available cooling system. Thus, during experiments, lower gradient amplitudes need to be applied in order to increase the duty cycles of operation, and check the temperatures of the MRI coils from rising beyond prescribed values.

In our work, we specifically concentrate on the development of the High Level Controller module, as shown in Figure 1.4. With the assumption that a perfect position feedback is obtained, this module generates the values of the MRI gradients required to keep the ferromagnetic particle on a specified path. These values are passed on to the Low Level
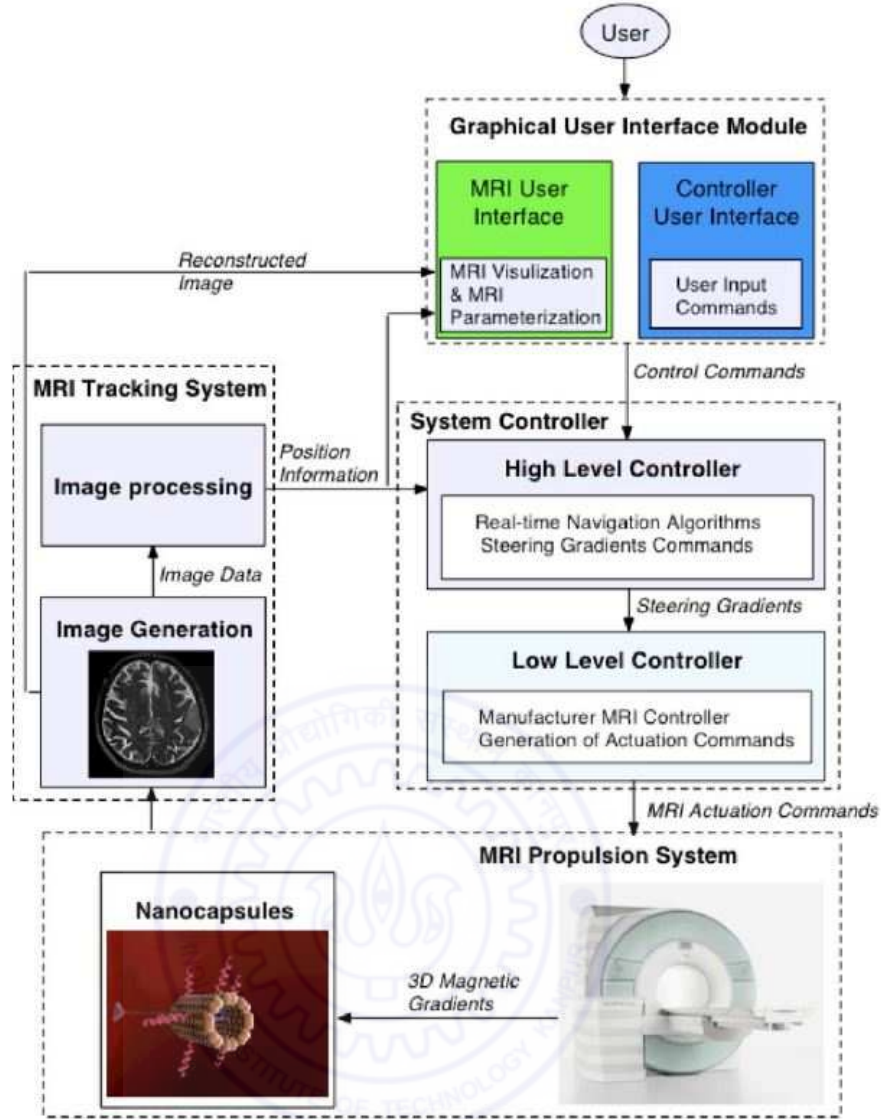
Figure 1.4: Architecture of MRI-Drug Delivery system [71]

Controller. This controller then generates appropriate electrical signals which generate the required gradients.

1.1.3 Literature in Modeling and Control of robotic manipulators

The trajectory tracking control problem for robotic manipulators involves the determination of joint inputs required to make the end-effector execute a commanded motion, which may be specified as a sequence of end-effector positions and orientations or as a continuous path. To achieve this control objective, an accurate model $f : \mathbf{q}, \dot{\mathbf{q}}, \ddot{\mathbf{q}} \rightarrow \mathbf{u}$ is necessary. Here, $\mathbf{q}, \dot{\mathbf{q}}, \ddot{\mathbf{q}}$ represent the joint position, velocity and acceleration vectors respectively, $\mathbf{u}$ represents the control input (which are the joint torque values) and the function $f(\cdot)$ is

Figure 1.5: The Barrett WAM robot

termed as the *Inverse Dynamics Model (IDM)* .

Thus, determining the IDM forms the first step towards solving the trajectory tracking problem. The Newton-Euler recursive technique and the Euler-Lagrange technique are the conventional ways of deriving the robot model analytically, based on rigid body dynamics [18], [23]. However, unknown nonlinearities present in real physical systems, which cannot be modeled by rigid body dynamics, often lead to poor tracking performance. This has led to a lot of research over the past decade on statistical machine learning techniques which try to learn the model of the system by treating it as a nonparametric nonlinear regression problem which does not use the rigid body dynamic model of the system [56,73]. The large volume of training data required for such techniques results in high computational complexity. Thus, the dynamic model is learned offline for pre-sampled trajectories. However, this results in some disadvantages. These methods might not prove to be very accurate for cases when either the robot dynamics change or the robot navigates in an unexplored part of the state space. Moreover, obtaining a suitable training data set for a robot with several degrees of freedom is also a challenging task. To overcome these difficulties, some recent research has been dedicated towards the development of fast online learning techniques [55,72].

We adopt a more conventional route. A nominal model of the system is first developed using the Newton-Euler approach. Next, we use two popular nonlinear control tools - Backstepping and SMC, to experimentally validate the model. The Backstepping ap-

proach is a recursive control technique applicable to nonlinear dynamical systems which can be expressed in the strict-feedback form and has been used extensively in literature for tracking problems [41]. A more robust control technique which serves as an ideal candidate for robotic systems is the Sliding Mode Control (SMC). As discussed earlier, the main advantages of this powerful tool are its simplicity of design and invariance of the system dynamics to matched disturbances once the system states reach the sliding surface . These features have made SMC a very attractive tool for researchers focusing on nonlinear mechanical systems [11, 65] . However, the vast majority of study on SMC and Backstepping, as applied to robotic manipulators, is limited to simulations. As has been mentioned earlier, the unknown nonlinearities existing in real robotic systems make the step from simulation to experimental validation a very challenging one. The precision achieved through our experiments validates the accuracy of the developed model.

This work forms a part of a research initiative where the main goal of ours is to build autonomous learning manipulators which will collaborate with humans, aiding them in their work. Motion modeling forms a part of our work where we model the arm motion of a Barrett WAM robot through Kinesthetic teaching. Motion models which are represented through dynamical systems, generate task specific suitable joint trajectories or end effector trajectories. Hence, we require proper control modules that would enable us to track those generated trajectories with precision. This work is an effort in that direction where we are exploring model based controllers through actual implementation. In our work, we assume that the motion modeling module generates joint trajectories which are fed to the controller. The development of the motion modeling module is a topic of research in itself. Figure 1.5 shows the Barrett WAM robot which we will be working with.

1.2   Thesis Organization

In Chapter 2, we provide the nonlinear model of the ferromagnetic micro-robot in the human vasculature. This exists in literature and has been presented for the sake of completeness. In Chapter 3, we discuss the development of the Adaptive Fuzzy Sliding Mode Control (AFSMC) scheme for the MRI based micro-robot navigation system. Design, stability analysis and simulation studies are included. In Chapter 4, we take up the rigid body modeling of the WAM robot. A detailed description of the modeling procedure is presented. This is followed up by experimental validation of the model through tracking experiments. In Chapter 5, we develop a Nonsingular Fast Terminal Sliding Mode Control (NFTSMC) scheme for control of the WAM. The basic theory is developed, an

analysis of the convergence time is presented, and simulations are presented to illustrate the main ideas. This is followed up by rigorous experimentation results on the Barrett WAM. Comparisons are made between simulation and experimental results, to give a feel of the differences existing between the two environments. In Chapter 6, we combine the continuous time Single Network Adaptive Critic (SNAC) architecture with SMC in an attempt to merge the robustness of SMC with optimal control theory. Theory, stability analysis, general design steps, and simulations to illustrate the applicability of the proposed technique are presented in this chapter. In Chapter 7, we conclude by giving a summary of the work done in this thesis and by listing the directions of future research.

Chapter 2

Nonlinear model of the ferromagnetic micro-robot in the human vasculature

2.1 Introduction

This chapter presents a detailed 2D nonlinear model of a micro-robot (which is a polymer bound aggregate of ferromagnetic particles) immersed inside the human blood vessels. A preliminary model for this system was established in [7], and was later further developed in [6] . In this chapter, we re-produce the latter for completeness. The model forms an essential part for control synthesis, which is dealt with in the next chapter.

2.2 The Model

The translational and rotational motions of the robot are expressed by [6]

$$m\frac{d\vec{v}}{dt} = \vec{F}_m + \vec{W}_a + \vec{F}_d + \vec{F}_c + \vec{F}_{vdw} + \vec{F}_e \qquad (2.2.1)$$

$$J\frac{d\vec{w}}{dt} = \vec{T}_m + \vec{T}_d + \vec{M}_c \qquad (2.2.2)$$

where $\vec{v}$ and $\vec{w}$ are the translational and rotational velocities of the robot and m and J are its mass and moment of inertia respectively. $\vec{F}_m, \vec{W}_a, \vec{F}_d, \vec{F}_c, \vec{F}_{vdw}$, and $\vec{F}_e$ denote respectively the magnetic force produced by the MRI gradient coils, the apparent weight, the blood hydrodynamic drag force, the robot-to-wall contact force, the Van der Waal's force and the electrostatic force. $\vec{T}_m, \vec{T}_d$ and $\vec{M}_c$ denote respectively the magnetic torque, the hydrodynamic drag torque and the robot-to-wall contact moment. It is assumed that

17

the orientation of the robot does not change due to the magnetic torque which aligns the magnetization of the robot along the external field ($B_0 = 3T$) as $\vec{T}_d$ and $\vec{M}_c$ are of much smaller order than $\vec{T}_m$. Figure 2.1 shows the parabolic profile of blood inside a blood vessel and the forces acting on the micro-robot.

2.2.1 Hydrodynamic Drag Force

The robot's motion is analysed using generic Navier-Stokes equations. Working under the assumption that fluid flow is mainly laminar, a drag force model can be used to approximate the hydrodynamic forces. The hydrodynamic drag force $\mathbf{F}_d$, that the fluid exerts on a spherical body is given by

$$\mathbf{F}_d = -\frac{1}{2}\rho_f \left(\frac{||\mathbf{v} - \mathbf{v}_f||}{\beta} \right)^2 AC_d \frac{(\mathbf{v} - \mathbf{v}_f)}{||\mathbf{v} - \mathbf{v}_f||} \tag{2.2.3}$$

Here, $\mathbf{v} - \mathbf{v}_f$ denotes the relative velocity of the micro-robot with respect to the fluid, A represents the frontal area of the core, ρ_f is the density of the fluid, and β , a dimensionless ratio related to the wall effect caused by the vessel's occlusion by the robot, is given by [38].

$$\beta = \frac{1 - \lambda^{\alpha_0}}{1 + (\frac{\lambda}{\lambda_0})^{\alpha_0}} \tag{2.2.4}$$

Here, $\lambda = \frac{2r}{D}$ and D denotes the vessel's diameter (in meter). The parameters α_0 and λ_0 are functions of the Reynold's number, but are commonly set to 1.5 and 0.29, respectively. The drag coefficient C_d, a function of the Reynolds number $Re = \frac{2r\rho_f|\mathbf{v}-\mathbf{v}_f|}{\beta\eta}$, is given by [76]

$$C_d = \frac{24}{Re} + \frac{6}{1 + \sqrt{Re}} + 0.4 \tag{2.2.5}$$

As blood is a non-newtonian fluid, its viscosity η is a function of the vessel's diameter d (in micron) and hematocrit rate h_d, and it is related to these quantities according to following empirical relation [62]

$$\eta = \frac{\eta_{plasma}d^2}{(d - 1.1)^2} \left(1 + \frac{(\eta_{0.45} - 1)d^2}{(d - 1.1)^2} \frac{(1 - h_d)^c - 1}{(1 - 0.45)^c - 1} \right) \tag{2.2.6}$$

Here, the parameter η_{plasma} denotes plasma's viscosity. $\eta_{0.45}$ represents the relative apparent blood's viscosity for a fixed discharge hematocrit rate of 0.45 and is given by

$$\eta_{0.45} = 6e^{-0.085d} + 3.2 - 2.44e^{-0.06d^{0.645}} \tag{2.2.7}$$

The shape of the viscosity dependence on hematocrit is given by

$$c = \frac{10^{11}}{d^{12}} - (0.8 + e^{-0.075d}) \left(\frac{d^{12}}{d^{12} + 10^{11}} \right) \tag{2.2.8}$$
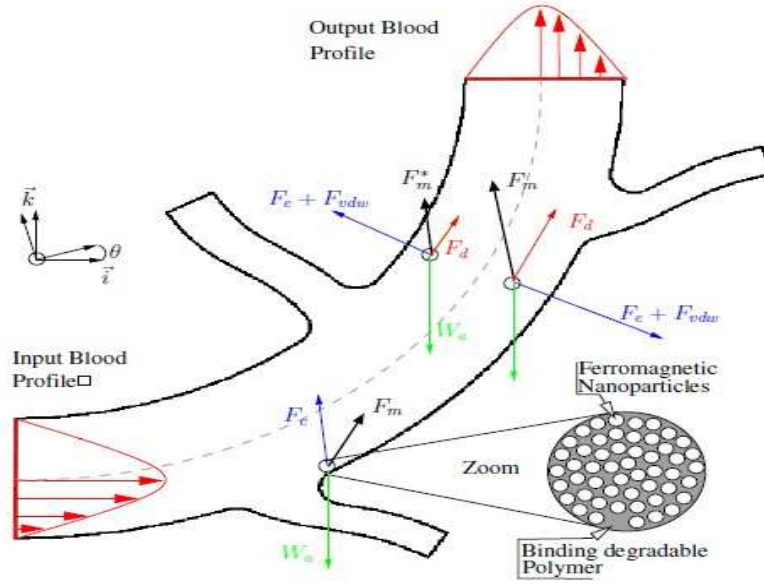
Figure 2.1: Schematic of a blood vessel with minor bifurcations [9]

The spatio-temporal variations in the velocity of blood are modeled using an affine combination of a time-varying periodic flow with a spatial parabolic shape. It is given by

$$v_f(t) = V_f(1 + a_f \sin(w_f t + \phi_f)) \times \left[1 - \left(\frac{\frac{D}{2} - h - r}{R}\right)^2\right] \qquad (2.2.9)$$

A periodic 10% deformation of the diameter of the blood vessel $D(t)$, synchronized with the blood velocity $v_f(t)$, is induced by pulsatile flow caused by cardiac pumping in arteries. This effect is taken into consideration by using the following equation

$$D(t) = D(1 + 0.1 \sin(w_f t + \phi_f)) \qquad (2.2.10)$$

Although a parabolic blood velocity profile has been assumed in this study, the presence of minor and major bifurcations (as one can see in Figure 2.1) can strongly affect the parabolic profile. An interested reader is referred to [10] for more analysis on this topic.

Remark - *The designed controller should be sufficiently robust to compensate the effect of bifurcations which might be thought of as a disturbance to the nominal model.*

2.2.2 Apparent Weight

The apparent weight (combined effect of buoyancy and weight) that acts on the micro-robot is given by

$$\mathbf{W}_a = V(\rho - \rho_f)g \qquad (2.2.11)$$

Here, V is the total volume of the robot, $\rho = \tau_m \rho_m + (1 - \tau_m)\rho_{poly}$ where ρ_m and ρ_{poly} are the magnetic material's and polymer's densities respectively, and $\tau_m = \frac{V_m}{V}$ where V_m is the ferromagnetic volume.

2.2.3 Contact Force

The contact force comes into play whenever there is an impact between the robot and the wall. Owing to the low velocity of the robot, the duration of the impact is not more than a few milliseconds. Thus, the contact force is expressed by a modified Hertzian contact law as given in [17]. Under the assumption of no friction between the robot and the wall during the impact period, the contact force is given by

$$\mathbf{F}_c = k\delta^{\frac{3}{2}} H(\delta)\mathbf{n} : \text{loading} \tag{2.2.12}$$

Here, δ is the elastic deformation of the wall at the point of contact, H represents the Heaviside function, $\mathbf{n}$ is the unit normal vector pointing from the robot to the contact surface, and k is the stiffness given by

$$k = \frac{\frac{4\sqrt{3}}{3}}{\frac{1-\sigma_p{}^2}{E_p} + \frac{1-\sigma_w{}^2}{E_w}} \tag{2.2.13}$$

Here, $E_p(E_w)$ is the Young's modulus of the robot (wall) and $\sigma_p(\sigma_w)$ is the Poisson's ratio of the robot (wall).

The contact force during unloading is different from the one during loading and is given by

$$\mathbf{F}_c = F_{cm} \left(\frac{\delta - \delta_0}{\delta_m - \delta_0} \right)^q H(\delta)\mathbf{n} : \text{unloading} \tag{2.2.14}$$

Here, F_{cm} and δ_m are the maximum contact force and corresponding maximum deformation of the wall during impact. δ_0 is the permanent deformation of the wall from loading/unloading cycles, and the exponent q varies between 1.5 and 2.5.

2.2.4 Van der Waals and Electrostatic Forces

The robot and the wall interact with each other through Van der Waals and Electrostatic forces. The Van der Waals potential between the walls of the blood vessel and the spherical micro-robot is given by [37]

$$\mathbf{V}_{vdw} = -\frac{A_h}{6} \left(\frac{1}{\bar{h}} + \frac{1}{2 + \bar{h}} + \ln\frac{\bar{h}}{2 + \bar{h}} \right) \mathbf{n} \tag{2.2.15}$$

Here, A_h is the Hamaker constant and $\bar{h} = \frac{h}{r}$ is the normalized distance between the robot and the wall, h represents the actual distance between the robot and the wall and

r represents the radius of the spherical micro-robot. The Van der Waals interaction force
is obtained by differentiating equation (2.2.15) and is given by

$$\mathbf{F}_{vdw} = -\nabla \mathbf{V}_{vdw} H(h) \tag{2.2.16}$$

The electrostatic force between the robot and the wall (which is considered to be an
uncharged surface) is given by [32]

$$\mathbf{F}_{el} = \frac{q^2}{4\pi\epsilon\epsilon_0(r+h)^2} H(h)\mathbf{n} \tag{2.2.17}$$

Here q is the charge of the robot, ϵ is the dielectric density of the medium of interaction,
and ϵ_0 is the permittivity of vacuum. The expression for the maximum allowable charge
of a spherical body of radius r, as given by Hays, [33] is

$$q(\mu C) = S \times Q = 4\pi r^2 \times 30(100r)^{-0.3} \tag{2.2.18}$$

2.2.5 Magnetic Force

The magnetic force F_m, that acts on the ferromagnetic micro-robot due to the magnetic
gradients produced by the gradient coils of the MRI system is given by

$$\mathbf{F}_m = \tau_m V(\mathbf{M}.\nabla)\mathbf{B} \tag{2.2.19}$$

Here $\mathbf{M}$ represents the magnetization of the material of the micro-robot, μ_0 is the perme-
ability of free space, and ∇B is the magnetic field gradient.

   Note - *The static field B_0 of an MRI device suffices to ensure saturation magnetization
M_{sat} of the material of the robot.*

2.3   Summary

In this chapter, we have presented a detailed nonlinear model of the micro-robot, outlining
the forces that act on it. A suitable SMC based control strategy has been developed for
this model in the next chapter.

Chapter 3

Development of a Fuzzy Sliding Mode Controller with Adaptive Tuning Technique for a MRI-guided robot

3.1 Introduction

In this chapter, we develop a control strategy based on the nonlinear model that was presented in Chapter 2. We primarily contribute towards the design of a Fuzzy Sliding Mode Controller (FSMC) for trajectory tracking of the micro robot in the human vasculature . An adaptive algorithm based on Lyapunov stability theory is used to estimate the parameters associated with the FSMC. The proposed FSMC is able to eliminate the chattering phenomenon completely which is present in conventional sliding mode control. Since the system in consideration is a biological one, many parameters are difficult to estimate, resulting in parametric uncertainties. A significant merit of the proposed framework is its ability to estimate the dielectric density of blood on-line with great accuracy.

We begin our study by presenting a state space representation of the model under consideration. This is followed up by development of the proposed control strategy and its stability analysis. Next, simulation results are presented, which indicate perfect tracking with very fast dynamical response. To illustrate the efficacy of our controller, a detailed comparison is made between the performances of a state-of-the-art adaptive backstepping control and our proposed control action, in the presence of bounded model uncertainties,

for micro-robots made up of different ferromagnetic materials .

3.2 State Space Representation

Let (x, z) represent the position of the robot in the blood vessel with respect to a given frame of reference $F(O, \vec{i}, \vec{k})$. The state space model is derived based on the differential equation (2.2.1) which defines the dynamical behaviour of the robot along the $\vec{i}$ and $\vec{k}$ axes

$$\begin{cases} m\ddot{x} = F_{mx} + F_{dx} + F_{cx} + F_{vdwx} + F_{ex} \\ m\ddot{z} = F_{mz} + F_{dz} + W_a + F_{cz} + F_{vdwz} + F_{ez} \end{cases} \tag{3.2.1}$$

where indexes x and z represent projections onto the $\vec{i}$ and $\vec{k}$ axes respectively. (Refer to Figure 2.1).

Let $x_1, x_2, (x_3, x_4)$ denote, respectively, the particle's position and velocity along the $\vec{i}$ axis (respectively along the $\vec{k}$ axis). Under the assumption that the positions x_1 and x_3 can be measured thanks to the MRI imaging system, let y denote the measured state. Using (3.2.1) , and taking into account modeling errors, we obtain the following set of state space equations

$$\begin{aligned} (S1) &\begin{cases} \dot{x}_1 = x_2 \\ \dot{x}_2 = f_2 + g_2\theta + U_1 + D_1 \end{cases} \\ (S2) &\begin{cases} \dot{x}_3 = x_4 \\ \dot{x}_4 = f_4 + g_4\theta + U_2 + D_2 \end{cases} \end{aligned} \tag{3.2.2}$$

where $f_2 = F_{dnx} + F_{cnx} + F_{vdwnx}$ and $f_4 = F_{dnz} + F_{cnz} + F_{vdwnz} + W_{an}$. The index n indicates that the forces are normalized with respect to the robot's mass m. Both f_2 and f_4 are highly non-linear functions of the full state. These forces are expressed as

$$F_{dn_x} = -\left(\frac{9\eta \cos(\phi)}{2r^2\beta\rho}||v - v_f|| + \frac{3\rho_f \cos(\phi)}{20r\beta^2\rho}||v - v_f||^2 + \frac{9\rho_f \cos(\phi)}{4r\beta^2\rho} \frac{||v - v_f||^2}{1 + \sqrt{\frac{2\rho_f r}{\beta\eta}}||v - v_f||} \right)$$

$$F_{eln_x} = \frac{3q^2 \sin(\psi)}{16\pi^2 r^3 \rho\epsilon\epsilon_0} \left(\frac{H(h_1)}{(r + h_1)^2} - \frac{H(h_2)}{(r + h_2)^2} \right)$$

$$F_{vdwn_x} = \frac{A_h \sin(\psi)}{8\pi r^2 \rho} \left[\left(\frac{1}{h_1^2} + \frac{1}{(2r + h_1)^2} - \frac{2}{h_1(2r + h_1)} \right) H(h_1) \right. \tag{3.2.3}$$
$$\left. - \left(\frac{1}{h_2^2} + \frac{1}{(2r + h_2)^2} - \frac{2}{h_2(2r + h_2)} \right) H(h_2) \right]$$

$$F_{cn_x} = \frac{3k \sin(\psi)}{4\pi r^3 \rho} \delta^{\frac{3}{2}} H(\delta)$$

24

Here h_1 and h_2 are the distances of the robot from the lower and the upper walls of the blood vessel respectively. ϕ represents the angle which the relative velocity of the robot (with respect to the blood's velocity) makes with the x-axis, and ψ represents the angle which the normal from the robot to the wall makes with the z-axis. These expressions are similar along the z axis and can be obtained as follows

$$F_{dn_z} = F_{dn_x} \tan(\phi)$$
$$F_{eln_z} = -F_{eln_x} \cot(\psi)$$
$$F_{vdwn_z} = -F_{vdwn_x} \cot(\psi) \tag{3.2.4}$$
$$F_{cn_z} = -F_{cn_x} \cot(\psi)$$

g_2 and g_4 represent the normalized electrostatic forces along the x and z directions without the uncertain dielectric density ϵ term . The uncertain dielectric density of blood which needs to be estimated is given by θ. Let $\mathbf{U} = (U_1, U_2)^T = (au_1, au_2)^T$, where the control inputs $u_1 = \nabla B_x$ and $u_2 = \nabla B_z$, are the magnetic gradients and parameter $a = \frac{\tau_m M}{\rho}$. $\mathbf{D} = (D_1, D_2)^T$ is the vector representing modeling errors , such that $|D_i| \leq \rho_i$, $i = 1, 2$, where ρ_i's are the known bounds on the modeling errors . Let $\mathbf{Y} = (x_1, x_3)^T$ and $\mathbf{Z} = (x_2, x_4)^T$ represent the position and velocity vectors respectively of the micro-robot. Let $\mathbf{X}_d = (x_d, z_d)^T$ represent the desired position trajectory of the micro-robot in the blood vessel. The position and velocity trajectory tracking errors are defined as follows

$$\mathbf{e} = (e_1, e_2)^T = \mathbf{Y} - \mathbf{X_d} \tag{3.2.5}$$

$$\dot{\mathbf{e}} = (\dot{e}_1, \dot{e}_2)^T = \dot{\mathbf{Y}} - \dot{\mathbf{X_d}} \tag{3.2.6}$$

Let the estimation error be defined as

$$\tilde{\theta} = \theta - \hat{\theta} \tag{3.2.7}$$

where θ represents the uncertain dielectric density term and $\hat{\theta}$ represents its estimate.

Note- *The dielectric density of blood varies highly from person to person and hence it is considered to be an uncertain parameter in the model. The developed control scheme should hence be able to estimate this parameter online.*

3.3   Adaptive Fuzzy Sliding Mode Control Scheme

In this section we develop the proposed control scheme. It should serve two purposes :

1. Be able to estimate the dielectric density of blood online.
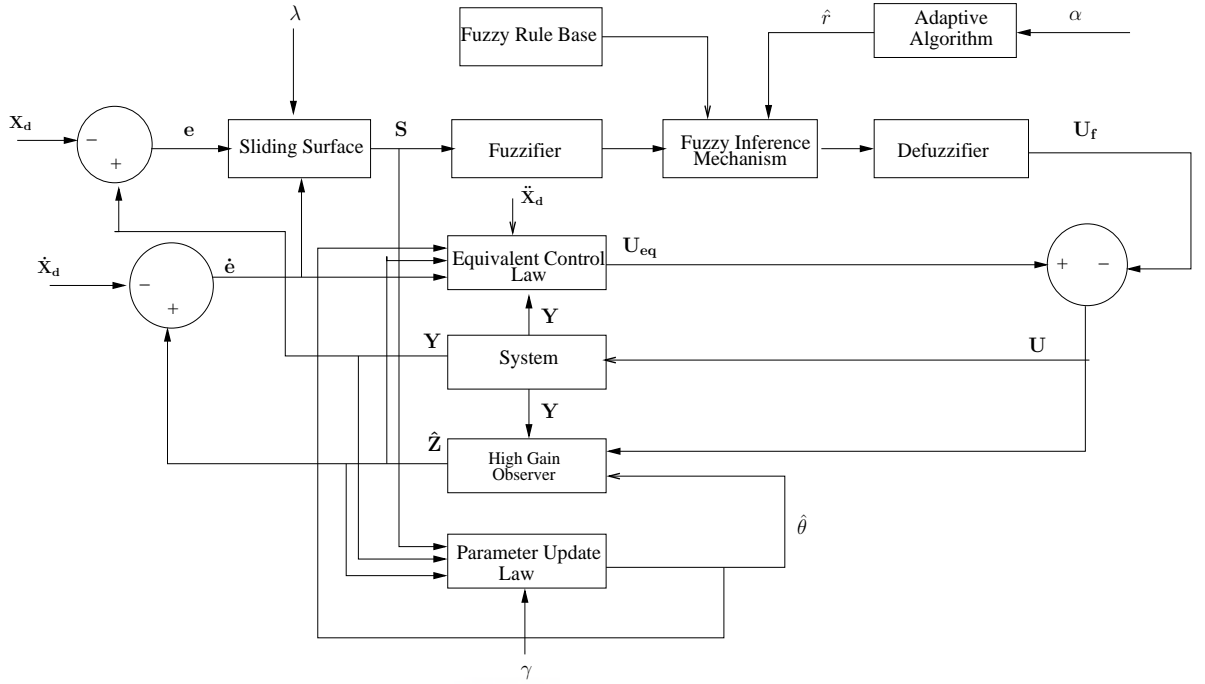
Figure 3.1: Block Schematic of the Adaptive Fuzzy Sliding Mode Control Scheme

2. Ensure that the tracking error between the actual and the reference trajectory converges to zero.

3.3.1 Conventional Adaptive Sliding Mode Control Technique

The sliding plane is defined as

$$\mathbf{S} = \dot{\mathbf{e}} + \boldsymbol{\lambda}\mathbf{e} \tag{3.3.1}$$

Where $\mathbf{S} = [s_1, s_2]^T$ and $\boldsymbol{\lambda} = diag(\lambda_1, \lambda_2)$; λ_1 and λ_2 are positive constants. The objective is to design a controller such that s_i $(i = 1, 2)$ are driven to the sliding plane

$$s_i = \dot{e}_i + \lambda_i e_i = 0, \quad i = 1, 2. \tag{3.3.2}$$

From (3.2.2), we can see that the system can be divided into two subsystems *(S1)* and *(S2)*. Since the two subsystems are similar in structure, the control law synthesis approach for the first subsystem will be exactly similar to that for the second one. Thus, we focus only on the first subsystem. We use the index 1 to denote all the terms associated with the first subsystem.

Let us define a Lyapunov candidate function as follows

$$V_1 = \frac{1}{2}{s_1}^2 + \frac{1}{2}\frac{\tilde{\theta}^2}{\gamma} \tag{3.3.3}$$

26

where γ is the adaptation gain such that $\gamma > 0$ Taking the derivative of (3.3.3), we obtain

$$\dot{V}_1 = s_1 \dot{s}_1 + \frac{\tilde{\theta}\dot{\hat{\theta}}}{\gamma} \tag{3.3.4}$$

From (3.2.2) and (3.3.2) we have

$$
\begin{aligned}
\dot{s}_1 &= \ddot{e}_1 + \lambda_1 \dot{e}_1 \\
&= \ddot{x}_1 - \ddot{x}_d + \lambda_1(\dot{x}_1 - \dot{x}_d) \\
&= \dot{x}_2 - \ddot{x}_d + \lambda_1(\dot{x}_1 - \dot{x}_d) \\
&= f_2 + g_2\theta + U_1 + D_1 - \ddot{x}_d + \lambda_1(\dot{x}_1 - \dot{x}_d) \tag{3.3.5}
\end{aligned}
$$

The equivalent control effort [63], [12] which is designed to guarantee desired performance under nominal model is derived as the solution of $\dot{s}_1 = 0$ without considering modeling errors and unmodeled dynamics ($D_1 = 0$). It is represented by U_{eq_1} and given by

$$U_{eq_1} = -f_2 - g_2\hat{\theta} + \ddot{x}_d - \lambda_1(\dot{x}_1 - \dot{x}_d) \tag{3.3.6}$$

The equivalent control law makes use of the estimate of the dielectric density of blood $\hat{\theta}$. The equivalent control effort cannot ensure favorable control performance in the presence of unpredictable perturbations arising as a result of parameter variations. Thus, an auxiliary control effort U_{h1}, known as the hitting control law, needs to be designed to eliminate the effect of unpredictable perturbations. In conventional SMC, U_{h1} is chosen as

$$U_{h1} = k_1 sgn(s_1) \tag{3.3.7}$$

where k_1 is the hitting control gain ($k_1 > 0$) and $sgn(.)$ is the sign function. k_1 is chosen such that $k_1 > \rho_1$. The complete control effort is given by

$$U_1 = U_{eq_1} - U_{h1} \tag{3.3.8}$$

Using (3.3.5), (3.3.6), (3.3.7) and (3.3.8) in (3.3.4), we obtain

$$
\begin{aligned}
\dot{V}_1 &= s_1[g_2(\theta - \hat{\theta}) - k_1 sgn(s_1) + D_1] + \frac{\tilde{\theta}\dot{\hat{\theta}}}{\gamma} \\
&= -s_1(k_1 sgn(s_1) - D_1) + \tilde{\theta}(s_1 g_2 + \frac{\dot{\hat{\theta}}}{\gamma}) \tag{3.3.9}
\end{aligned}
$$

Let the parameter update law be defined as

$$\dot{\hat{\theta}} = -\gamma s_1 g_2 \tag{3.3.10}$$

or

$$\dot{\hat{\theta}} = \gamma s_1 g_2 \tag{3.3.11}$$
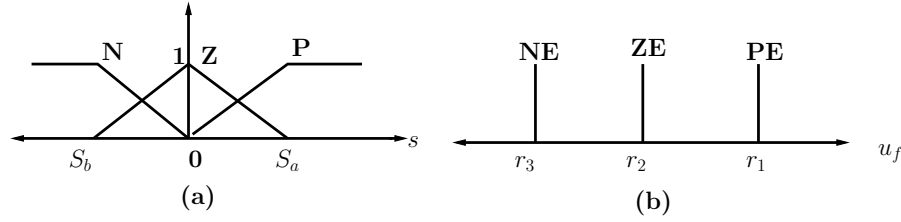
Figure 3.2: (a) Input membership function (b) Output membership function

This gives

$$
\begin{aligned}
\dot{V}_1 &= -s_1(k_1 sgn(s_1) - D_1) \\
&\leq |s_1|\rho_1 - k_1|s_1| \\
&= -|s_1|(k_1 - \rho_1) \leq 0
\end{aligned} \tag{3.3.12}
$$

This ensures that the system is stable in the sense of Lyapunov.

3.3.2 Fuzzy hitting control law

If the upper bound of the modeling errors is chosen too high, the sign function of the hitting law would cause serious chattering phenomenon in the control efforts. Although the boundary layer approximation technique reduces the chatter amplitude, improper choice of the width of the boundary layer might result in unstable tracking responses. In order to overcome this effect, we employ a fuzzy logic inference mechanism [45, 54, 74] to mimic the hitting law.

The sliding surface s_1 is chosen as the input linguistic variable of the fuzzy logic and the fuzzy hitting control law U_{f_1} is taken as the output linguistic variable. The membership functions for the input (s_1) and output (U_{f_1}) fuzzy sets are shown in Figure 3.2. In accordance with the nature of the hitting control law in (3.3.7), the fuzzy linguistic rule base can be summarized as follows

Rule 1: If s_1 is P (positive), then U_{f_1} is PE (positive effort).
Rule 2: If s_1 is Z (zero), then U_{f_1} is ZE (zero effort).
Rule 3: If s_1 is N (negative), then U_{f_1} is NE (negative effort).

In our work, we use triangular type-input membership functions and singleton type output membership function owing to their computational simplicity. For defuzzification, the center-of-gravity method is adopted. The fuzzy hitting control law, estimated by the

fuzzy logic inference mechanism is given by

$$U_{f1} = \frac{\sum\limits_{i=1}^{3} w_i r_i}{\sum\limits_{i=1}^{3} w_i} = w_1 r_1 + w_2 r_2 + w_3 r_3 \tag{3.3.13}$$

where $0 \leq w_1 \leq 1$, $0 \leq w_2 \leq 1$, and $0 \leq w_3 \leq 1$ are the firing strengths associated with rules 1, 2 and 3 respectively ; $r_1 = r$, $r_2 = 0$ and $r_3 = -r$ are the centers of the membership functions PE, ZE and NE respectively; r is the fuzzy parameter to be tuned by an adaptive algorithm and the relation $w_1 + w_2 + w_3 = 1$ holds true based on our choice of special triangular membership functions. Noting that one of the four following conditions would occur based on the value of s_1, the hitting law U_{f1} is further analyzed.

Condition 1: Only rule 1 is triggered.

$(s_1 > S_a; w_1 = 1; w_2 = w_3 = 0)$

$U_{f1} = r$

Condition 2: Rules 1 and 2 are triggered simultaneously.

$(0 < s_1 \leq S_a; 0 < w_1, w_2 \leq 1; w_3 = 0)$

$U_{f1} = r_1 w_1 = r w_1$

Condition 3: Rules 2 and 3 are triggered simultaneously.

$(S_b < s_1 \leq 0; w_1 = 0; 0 \leq w_2, w_3 < 1)$

$U_{f1} = r_3 w_3 = -r w_3$

Condition 4: Only rule 3 is triggered

$(s_1 \leq S_b; w_1 = w_2 = 0; w_3 = 1)$

$U_{f1} = -r$

Based on the four possible conditions, it can be seen that

$$s_1(w_1 - w_3) = |s_1||(w_1 - w_3)| \geq 0 \tag{3.3.14}$$

and

$$U_{f1} = r(w_1 - w_3) \tag{3.3.15}$$

The AFSMC control law can be represented as

$$U_1 = U_{eq1} - U_{f1} = U_{eq1} - r(w_1 - w_3) \tag{3.3.16}$$

where U_{eq1} is given by (3.3.6)

3.3.3 Adaptive Fuzzy Parameter Tuning Algorithm

In this section we develop a simple adaptive algorithm based on Lyapunov stability theory to tune the fuzzy parameter r. A schematic of the entire control architecture is shown in Figure 3.1.

Theorem 3.3.1. *For subsystem ($\mathbf{S_1}$) of the model (3.2.2), representing the dynamics of the micro-robot in the human vasculature , the adaptive fuzzy sliding mode control law, $U_1 = U_{eq_1} - \hat{r}(w_1 - w_3)$, will stabilize the subsystem in the sense of Lyapunov, provided $\hat{r}$ is updated using the update law $\dot{\hat{r}} = \frac{1}{\alpha}(w_1 - w_3)s_1$, where α is a positive constant and $\hat{\theta}$ is updated using the update law $\dot{\hat{\theta}} = \gamma s_1 g_2$ where $U_{eq_1} = -f_2 - g_2\hat{\theta} + \ddot{x}_d - \lambda_1(\dot{x}_1 - \dot{x}_d)$.*

Proof. Let us consider the following control Lyapunov function candidate

$$V_1 = \frac{1}{2}{s_1}^2 + \frac{1}{2}\frac{\tilde{\theta}^2}{\gamma} \tag{3.3.17}$$

Taking the time derivative of the Lyapunov candidate, we get

$$\dot{V}_1 = s_1\dot{s}_1 + \frac{\tilde{\theta}\dot{\tilde{\theta}}}{\gamma} \tag{3.3.18}$$

From (3.3.5) we have

$$\dot{s}_1 = f_2 + g_2\theta + U_1 + D_1 - \ddot{x}_d + \lambda_1(\dot{x}_1 - \dot{x}_d) \tag{3.3.19}$$

Substituting (3.3.16) in (3.3.19) and then in (3.3.18) gives

$$\begin{aligned}\dot{V}_1 &= s_1[g_2(\theta - \hat{\theta}) - r(w_1 - w_3) + D_1] + \frac{\tilde{\theta}\dot{\tilde{\theta}}}{\gamma} \\ &= -s_1[r(w_1 - w_3) - D_1] + \tilde{\theta}(s_1 g_2 + \frac{\dot{\tilde{\theta}}}{\gamma})\end{aligned} \tag{3.3.20}$$

Using (3.3.10) in (3.3.20) we obtain

$$\dot{V}_1 = -s_1[r(w_1 - w_3) - D_1] \tag{3.3.21}$$

If

$$r > \frac{D_1}{(w_1 - w_3)} \tag{3.3.22}$$

then the condition $\dot{V}_1 \leq 0$ will be satisfied. According to (3.3.22), there exists an optimal value for r^* to achieve minimum control efforts and to ensure Lyapunov stability and it is given by

$$r^* = \frac{D_1}{(w_1 - w_3)} + \epsilon \tag{3.3.23}$$

where ϵ is a small positive constant.

Owing to the model uncertainties , the optimal value r^* cannot be ascertained in advance for practical applications. Hence, we employ a simple adaptive algorithm to estimate the optimal value r^* . The estimation error is defined as

$$\tilde{r} = \hat{r} - r^* \tag{3.3.24}$$

where $\hat{r}$ is the estimated value of r^*. Choose a Lyapunov candidate as

$$V_1(s_1, \tilde{r}, \tilde{\theta}) = \frac{1}{2}s_1{}^2 + \frac{1}{2}\frac{\tilde{\theta}^2}{\gamma} + \frac{1}{2}\alpha \tilde{r}^2 \tag{3.3.25}$$

where α is a positive constant. Taking the derivative of $V_1(s_1, \tilde{r}, \tilde{\theta})$ with respect to time, and using (3.3.10),(3.3.19) and (3.3.24), one can obtain

$$\begin{aligned}
\dot{V}_1(s_1, \tilde{r}, \tilde{\theta}) &= s_1\dot{s}_1 + \frac{\tilde{\theta}\dot{\tilde{\theta}}}{\gamma} + \alpha \tilde{r}\dot{\tilde{r}} \\
&= s_1[g_2(\theta - \hat{\theta}) - \hat{r}(w_1 - w_3) + D_1] + \frac{\tilde{\theta}\dot{\tilde{\theta}}}{\gamma} + \alpha \tilde{r}\dot{\tilde{r}} \\
&= -s_1[\hat{r}(w_1 - w_3) - D_1] + \tilde{\theta}(s_1 g_2 + \frac{\dot{\tilde{\theta}}}{\gamma}) + \alpha \tilde{r}\dot{\tilde{r}} \\
&= -s_1[\hat{r}(w_1 - w_3) - D_1] + \alpha \tilde{r}\dot{\tilde{r}}
\end{aligned} \tag{3.3.26}$$

Substituting (3.3.23) in (3.3.26) we obtain

$$\begin{aligned}
\dot{V}_1(s_1, \tilde{r}, \tilde{\theta}) &= -s_1[\tilde{r}(w_1 - w_3) + \epsilon(w_1 - w_3)] + \alpha \tilde{r}\dot{\tilde{r}} \\
&= -s_1\epsilon(w_1 - w_3) + \tilde{r}[\alpha \dot{\tilde{r}} - s_1(w_1 - w_3)]
\end{aligned}$$

$$\tag{3.3.27}$$

If the adaptation law for the fuzzy parameter is chosen as

$$\dot{\hat{r}} = \frac{1}{\alpha}s_1(w_1 - w_3), \tag{3.3.28}$$

(3.3.27) becomes

$$\dot{V}_1(s_1, \tilde{r}, \tilde{\theta}) = -s_1\epsilon(w_1 - w_3) \tag{3.3.29}$$

From the inequality $s_1(w_1 - w_3) \geq 0$ and the fact that ϵ is a positive constant, one can obtain that $\dot{V}_1(s_1, \tilde{r}, \tilde{\theta}) \leq 0$, that is, $\dot{V}_1(s_1, \tilde{r}, \tilde{\theta})$ is negative semi-definite. This implies that $s_1(t), \tilde{r}(t)$ and $\tilde{\theta}(t)$ are bounded. Let function $F(t) = s_1\epsilon(w_1 - w_3) = -\dot{V}_1(s_1(t), \tilde{r}(t), \tilde{\theta}(t))$. Integrating $F(t)$ with respect to time

$$\int_0^t F(\tau)d\tau = V_1(s_1(0), \tilde{r}(0), \tilde{\theta}(0)) - V_1(s_1(t), \tilde{r}(t), \tilde{\theta}(t)) \tag{3.3.30}$$

As $V_1(s_1(0), \tilde{r}(0), \tilde{\theta}(0))$ is bounded and $V_1(s_1(t), \tilde{r}(t), \tilde{\theta}(t))$ is non-increasing and bounded, the following result can be obtained

$$\lim_{t \to \infty} \int_0^t F(\tau) < \infty \qquad (3.3.31)$$

Taking the derivative of $F(t)$, we get

$$\dot{F} = \dot{s}_1(w_1 - w_3)\epsilon + \epsilon s_1(\dot{w}_1 - \dot{w}_3) \qquad (3.3.32)$$

From (3.3.16) and (3.3.19), it is clear that

$$\dot{s}_1 = [g_2\tilde{\theta} - \hat{r}(w_1 - w_3) + D_1] \qquad (3.3.33)$$

As $D_1 < \rho_1$ and $0 \le w_1, w_3 \le 0$, from (3.3.23) it is obvious that r^* is bounded. As r^* and $\tilde{r}$ are both bounded , $\hat{r}$ is also bounded. Since, g_2 is bounded , $\dot{s}_1$ is also bounded . Further, since $\dot{w}_1, \dot{w}_3$ are bounded, $\dot{F}(t)$ is bounded for all time. Hence, $F(t)$ is uniformly continuous. Thus, by Barbalat's Lemma [63], it can be shown that $\lim_{t\to\infty} F(t) = 0$, that is , $s_1 \to 0$ as $t \to \infty$. This proves that the system is asymptotically stable and that the tracking error will converge to zero as $s_1 \to 0$. The AFSMC control law U_{eq_2} for subsystem ($\mathbf{S_2}$) can be derived in a similar manner. $\qquad \square$

__Note__ - The final control law is a function of the position error and also its derivative. The derivative of the position error requires knowledge of the velocity of the micro-robot. However, the MRI imaging modality can provide information regarding the position only. Thus, an observer is required to estimate the velocity of the micro-robot along the horizontal and vertical directions. For this purpose, we choose the structure of the high gain observer proposed in [8]. The choice of this observer is motivated by the fact that locally Lipschitzian state's functions ensure the convergence of the observer. It has been shown by the authors in [8], that the model (3.2.2) satisfies this constraint. In this work, we focus on the development of the controller only.

Table 3.1: Simulation Data

Plasma's viscosity	η_{plasma}	$5 \times 10^{-3}[Pa.s]$
Blood's density	ρ_f	$1060[kg.m^{-3}]$
	V_f	$.025[m.s^{-1}]$
Blood's velocity	a_f	1.15
	w_f	2π
parameters	ϕ_f	$\frac{\pi}{2}$
Robot's density	ρ_m	$8200[kg.m^{-3}]$
Robot's radius	r	$350[\mu m]$
Robot's Young modulus	E_p	$10^9[Pa]$
Wall's Young modulus	E_w	$10^6[Pa]$
Robot's Poisson's ratio	σ_p	0.27
Permanent deformation	δ_0	$0[m]$
Vessel's diameter	D	$3[mm]$
Polymer's density	ρ_{poly}	$1500[kg.m^{-3}]$
Ferromagnetic ratio	τ_m	0.95
Magnetization	M	$1.95 \times 10^6[A.m^{-1}]$
Hematocrit	h_d	0.45
Hamaker constant	A_h	$4 \times 10^{-19}[J]$
Blood's dielectric density	ϵ	$77[C^2.N^{-1}.m^{-2}]$
Initial conditions	$(x_{10}, x_{20}, x_{30}, x_{40})$	$(0.001, 0, 0.002, 0)$
	$(\hat{x}_{10}, \hat{x}_{20}, \hat{x}_{30}, \hat{x}_{40})$	$(0.001, 0.001, 0.002, 0.001)$
Input saturation	U_{sat}	$80[mT.m^{-1}]$
	(k_1, k_2)	$(5, 5)$
Control parameters	(λ_1, λ_2)	$(15, 15)$
	α, γ	$10, 10^{13}$
	S_a, S_b	$(0.001, -.001)$
Observer gains	L	800
	(g_1, g_2, g_3, g_4)	$(-20, -20, -20, -20)$
Initial conditions on Fuzzy parameters	(r_{10}, r_{20})	$(150, 150)$

Table 3.2: Comparison of the two control techniques

Material	Backstepping Control				AFSMC			
	Mean Tracking Error		Mean Control Input		Mean Tracking Error		Mean Control Input	
	$e_x(\mu m)$	$e_z(\mu m)$	$u_x(mT.m^{-1})$	$u_z(mT.m^{-1})$	$e_x(\mu m)$	$e_z(\mu m)$	$u_x(mT.m^{-1})$	$u_z(mT.m^{-1})$
Permendur	14.77	70.99	12.5	36.1	8.76	4.56	12.9	36.3
NdFeB-35	14.48	60.91	19.8	51.6	8.75	4.53	20.4	51.7
Alfenol	14.61	72.59	38.4	85.6	8.68	4.49	39.8	85.3
Supermalloy	15.01	74.69	30.7	96.6	8.79	4.57	32.1	96.6
Fe_30_4	15.32	56.9	70.3	117.1	8.71	4.54	71.6	117
Average	14.84	67.22	34.34	77.4	8.74	4.54	35.36	77.42

3.4 Simulation Results and Analysis

The simulations are conducted keeping in mind the limitations of a clinical MRI system. It is assumed that the MRI devices can provide a maximum magnetic field gradient of $80mT.m^{-1}$. This limitation is additionally affected by the gradient coils' duty cycle and by the multiplexing needed for both controlling and observing. To ensure that the control amplitudes do not exceed the capacity of the MRI system, the applied control law U_a is adjusted as follows

$$U_a = \frac{U}{k}, k = max[1, \frac{U}{U_{sat}}] \tag{3.4.1}$$

where $U_{sat} = 80mT.m^{-1}$ is the maximum magnetic field gradient that can be provided by the MRI coils.

The robot is made to track the center-line of a blood vessel. First, we test the robustness of the proposed AFSMC methodology by comparing its tracking performance with the adaptive backstepping control developed in [9]. Based on the dynamic model developed in [6] and the proposed control action, the simulation parameters are defined in Table 3.1. For the adaptive backstepping control, the control gains are $k_1 = 20, k_2 = 20$. To have a fair comparison between both the control techniques, the Observer gains are kept same for both the methods. Also, simulations are done on both the techniques using the same set of simulation parameters for the model, and the same initial conditions which are mentioned in Table 3.1 . To test the robustness of the schemes, we choose $\mathbf{D} = (0.01sin(4\pi t), 0.01cos(4\pi t))$ to physically represent unmodeled dynamics of the system. The tracking performance of the AFSMC and adaptive backstepping control in the presence of the disturbances are plotted in Figure 3.3 and Figure 3.4 respectively . It is

Table 3.3: Material Properties

Material	Magnetization at Saturation $(A.m^{-1})$	$\rho(kg.m^{-3})$
Permendur	1.95×10^6	8200
NdFeB-35	1.23×10^6	7500
Alfenol	0.63×10^6	6500
Supermalloy	0.79×10^6	8800
Fe_3O_4	0.35×10^6	5200

seen that whereas the AFSMC methodology causes convergence of the actual trajectory
to the reference trajectory, the adaptive backstepping approach fails in this context. This
clearly establishes the superior robustness of the proposed approach.

To have a detailed comparison of the backstepping approach with the proposed AFSMC
scheme, Table 3.2 provides an insight into the mean tracking errors and the control efforts
required for both the techniques, for micro-robots made up of different ferromagnetic
materials. The material properties are listed in Table 3.3. It can be seen that although
the control efforts required are nearly the same, the tracking accuracy of the AFSMC
scheme is far better than that of the backstepping approach. It is to be noted that for
this comparison, no limits have been set on the control input. This is done purposely to
also ascertain the best material, which ensures that the magnetic gradients of the MRI
coils remain within the practical limit of $80mT.m^{-1}$. Permendur and NdFeB-35 satisfy
this criterion and hence are ideal candidates for material fabrication of the micro-robot.

The position and velocity error trajectories in the presence of time-varying disturbances
with the AFSMC method are shown in Figure 3.5 and Figure 3.6 respectively. Clearly, the
proposed control action causes the position and velocity errors to converge to zero within
0.5 seconds. The mean position tracking errors in the transient period are limited to
$8.76\mu m$ and $4.56\mu m$ along the x and z directions respectively, indicating the high tracking
accuracy of the controller. The simulation is performed assuming an initial error of 30%
from the nominal blood's dielectric value. It is seen from Figure 3.7 that the estimated
parameter converges to its true value at steady state. The motivation behind estimating
the uncertain parameter ϵ on-line is justified. This is because among the physiological
parameters of the model, which are the most difficult to measure and are very variable
from one patient to another, sensitivity is the highest for ϵ .

The effectiveness of the developed scheme is investigated by comparing it with the
conventional SMC. Figure 3.9 shows the chattering phenomenon present in conventional

SMC. Figure 3.10 shows that with the AFSMC technique, the control inputs are much more smooth and that the chattering phenomenon has been completely eliminated. Further, the control inputs are within the necessary bounds imposed for this application and hence there is no saturation. Thus, the results indicate that the designed controller is inherently robust to even time varying perturbations. From Figure 3.3, it should be noted that since the curvature of the blood vessel is very small (the blood vessel can be thought of as a nearly horizontal pipe), the horizontal component of the drag force is much larger than the vertical component. A direct consequence of this effect is reflected in Figure 3.10 where the z-component (vertical component) of the control input remains nearly constant. This is because it has to mainly counter-balance the apparent weight of the micro-robot which is far larger than the vertical component of the drag force. Assuming that the drag force along the vertical direction is zero, the magnetic field gradient $u_z = \nabla B_z$ along the z-direction required to balance the apparent weight would be given by

$$u_z = \nabla B_z = \frac{(\rho - \rho_f)g}{M} = 34.23 mT.m^{-1} \qquad (3.4.2)$$

where $\rho = \tau_m \rho_m + (1 - \tau_m)\rho_{poly}$. From simulations, it is found that once steady state is reached, the control input u_z varies from $34.6 mT.m^{-1}$ to $35.9 mT.m^{-1}$. This shows that indeed the effect of apparent weight dominates that of the vertical component of drag force. The slight variations are due to the non-zero vertical component of drag force. Figure 3.8 shows the time evolution of the sliding surfaces.

***Note** - In this study, we have designed the controller to make the micro-robot track the center line of a blood vessel. However, this is not the most optimal trajectory in terms of required control effort. From force balance, it is possible to obtain a set of optimal points which minimize the control effort (in this case the magnetic force F_m) and then link them using B-splines to obtain a C^2 reference trajectory. This is a topic of research in itself and an interested reader is referred to [49]. In our work, we primarily focus on the precision that can be achieved given a trajectory and not on the details which are involved in defining the trajectory itself.*
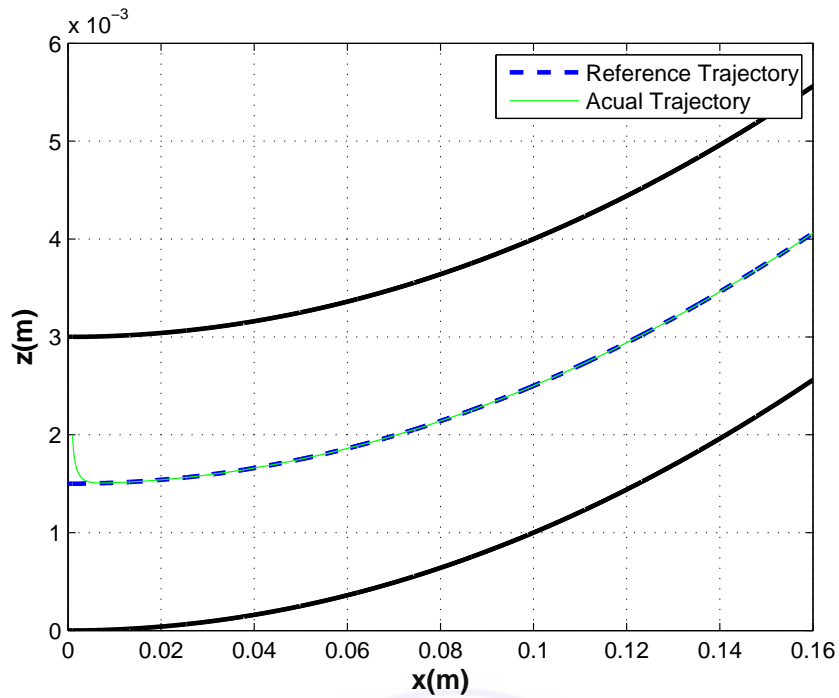
Figure 3.3: Reference and Actual trajectories of the micro-robot in the case of AFSMC with disturbance
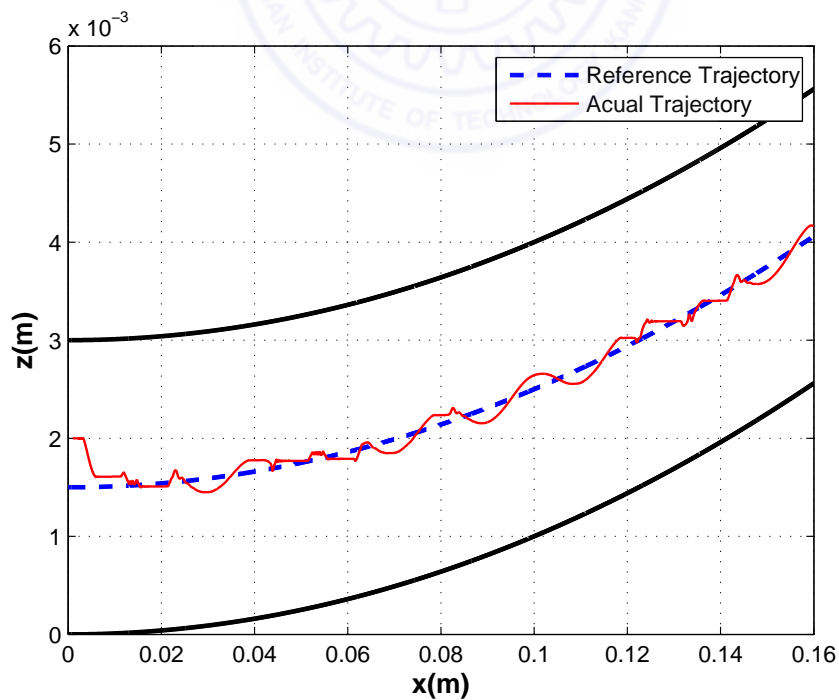
Figure 3.4: Reference and Actual trajectories of the microrobot in the case of Backstepping Control with disturbance
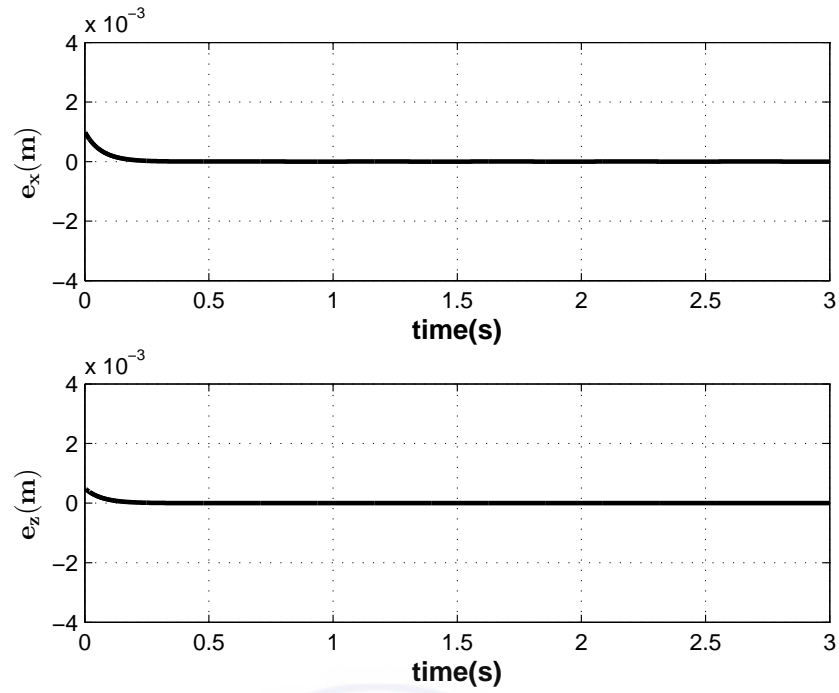
Figure 3.5: Position error trajectories of the microrobot in the case of AFSMC with disturbance
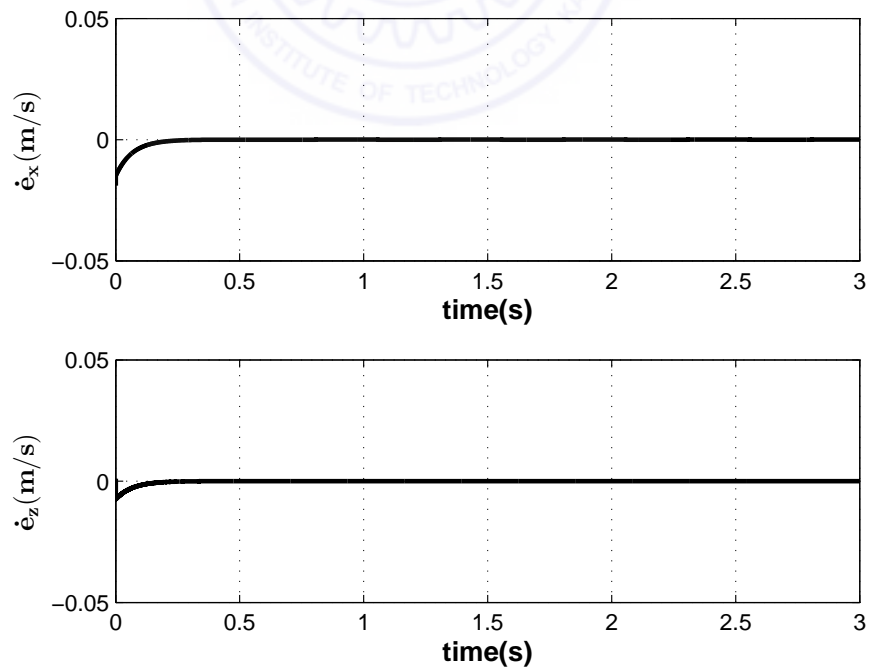
Figure 3.6: Velocity error trajectories of the microrobot in the case of AFSMC with disturbance
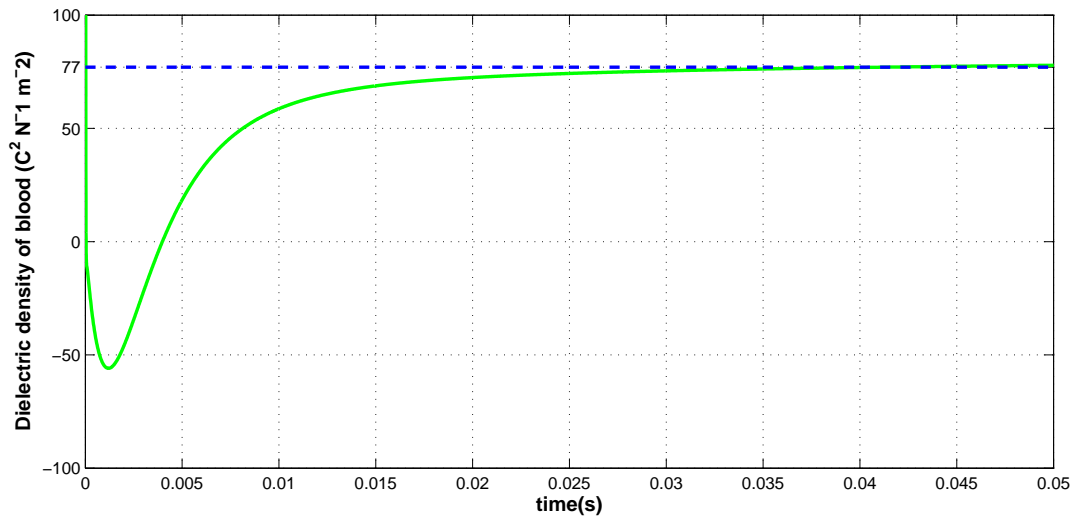
Figure 3.7: Estimation of blood's dielectric density ϵ
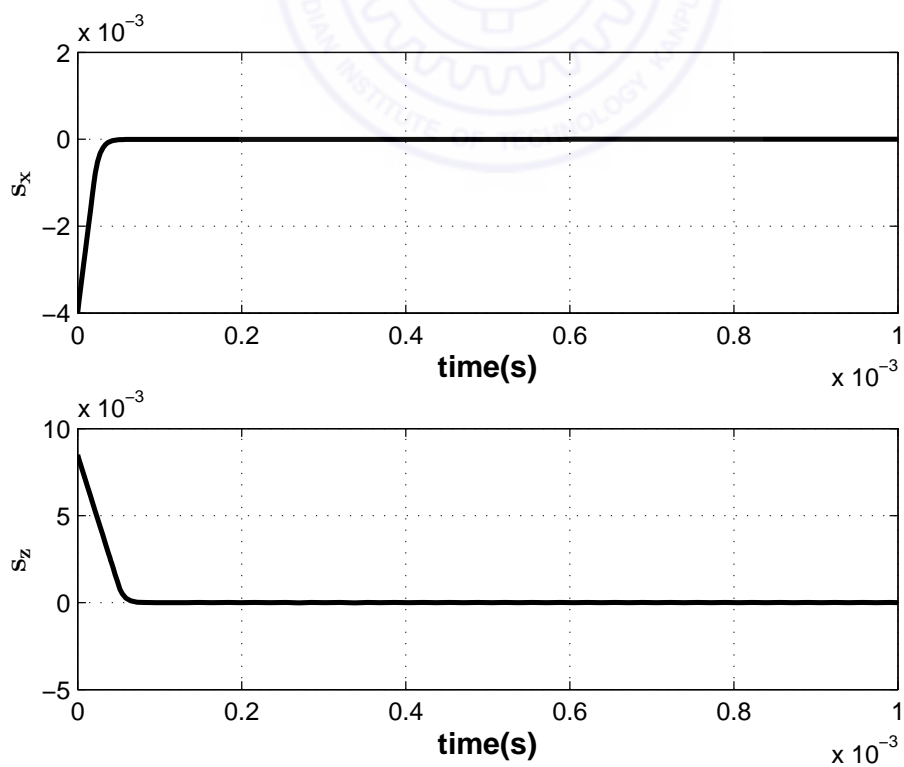
Figure 3.8: Time evolution of the Sliding Surfaces
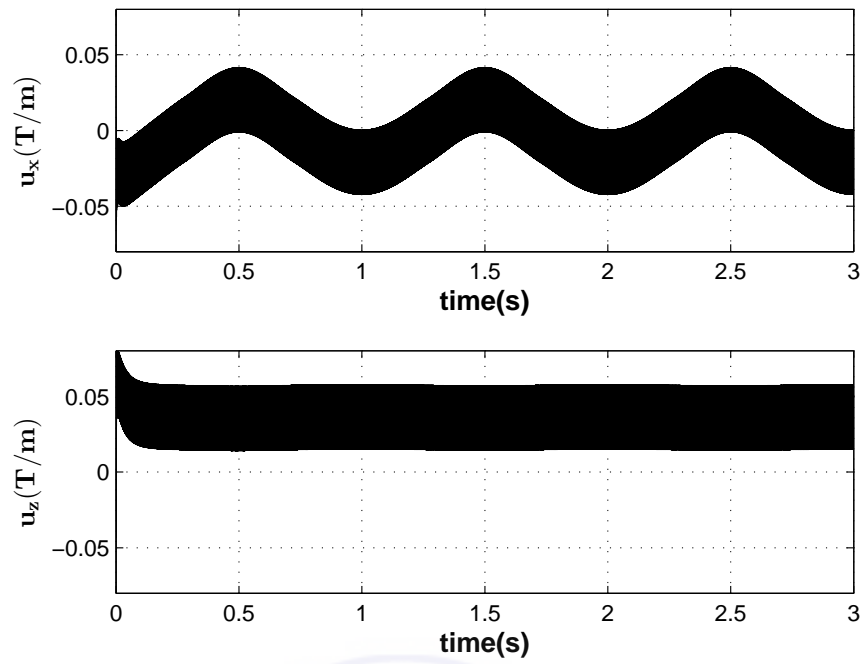
Figure 3.9: Control input in the case of SMC with disturbance
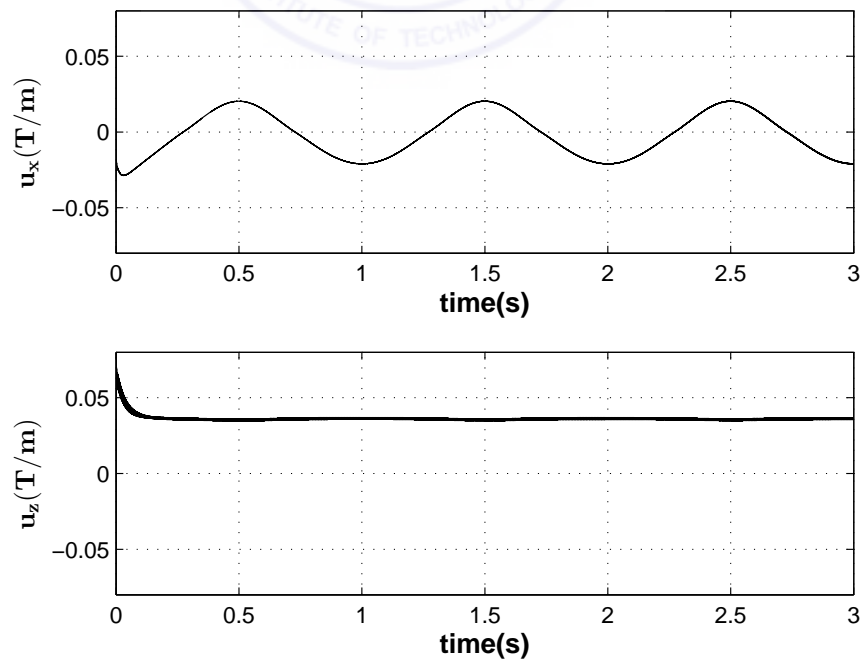
Figure 3.10: Control input in the case of AFSMC with disturbance

3.5 Summary

In this chapter we designed an adaptive fuzzy sliding mode controller which serves two purposes - it achieves perfect trajectory tracking of a therapeutic micro-robot navigating in a blood vessel along a predefined trajectory, and it also performs on-line estimation of a key physiological parameter - the dielectric density of blood. A comparative study with the adaptive backstepping approach indicates the robustness of our methodology in the presence of bounded time varying perturbations. The developed AFSMC system is seen to remove the chattering effect altogether, yielding smooth control laws, which remain within the bounds set for this application. The adaptive algorithm developed to tune the fuzzy parameter proves to be effective in confronting modeling errors and system uncertainties. Thus, the feasibility of an Adaptive Fuzzy Sliding Mode Control technique for trajectory tracking of a micro-robot in the human vasculature, is investigated in sufficient detail and the validity of the approach is established via simulation results.

Chapter 4

Dynamic Modeling of the Barrett Whole Arm Manipulator (WAM) and Experimental Validation

4.1 Introduction

Precise model based control necessitates the requirement of an accurate model of the robotic system. The major contribution of this chapter is the development of a dynamic model for 4 DOF operation of the Barrett Whole Arm Manipulator (WAM). We use the recursive Newton-Euler technique to achieve the same. A detailed description of the parameters required for implementing the Newton-Euler algorithm is presented. We validate the accuracy of the derived model through rigorous experimental studies. Specifically, we test the precision in trajectory tracking tasks using two popular nonlinear control strategies - Backstepping and Sliding Mode, and draw a comparison between the two techniques. While several papers have addressed the trajectory tracking problem in simulation studies on two-link planar rigid manipulators, the differences existing between the nominal model and the real model, owing to friction and other unmodeled dynamic terms, make experimental validation a challenging task. The precise trajectory tracking results which we achieve through our experiments, illustrate the accuracy of the model so derived and the effectiveness of the control schemes in real experiments as opposed to confinement to simulation studies.

4.2   Newton-Euler Technique

The Newton-Euler formulation is based on three important laws of mechanics -

- Every action has an equal and opposite reaction. Thus, if link i exerts a force f and a torque τ on link $i + 1$, then link $i + 1$ in turn exerts a force $-f$ and a torque $-\tau$ on link i.

- The rate of change of linear momentum equals the total force applied to the link.

- The rate of change of angular momentum equals the total torque applied to the link.

Based on these basic principles, the governing equations for this technique can be derived [64], [34]. We present the main steps of implementation of the Newton-Euler algorithm -

---

Algorithm 1 Newton-Euler Algorithm

Forward Recursion : Computing ω_i, α_i and $a_{c,i}$

Initial Conditions: $\omega_0 = 0$, $\alpha_0 = 0$, $a_{c,0} = 0$ and $a_{e,0} = 0$

for each $i := 1$ *to* n **do**

$\quad \omega_i \leftarrow R^i_{i-1}\omega_{i-1} + b_i\dot{q}_i$; where $b_i = R^i_{i-1}z_0$

$\quad \alpha_i \leftarrow R^i_{i-1}\alpha_{i-1} + b_i\ddot{q}_i + \omega_i \times b_i\dot{q}_i$

$\quad a_{e,i} \leftarrow R^i_{i-1}a_{e,i-1} + \dot{\omega}_i \times r_{i,i+1} + \omega_i \times (\omega_i \times r_{i,i+1})$

$\quad a_{c,i} \leftarrow R^i_{i-1}a_{e,i-1} + \dot{\omega}_i \times r_{i,c_i} + \omega_i \times (\omega_i \times r_{i,c_i})$

end for

Backward Recursion : Computing f_i and τ_i

Terminal Conditions: $f_{n+1} = 0, \tau_{n+1} = 0$

for each $j := n$ *to* 1 **do**

$\quad g_i \leftarrow R^i_0 g_0$

$\quad f_i \leftarrow R^i_{i+1}f_{i+1} + m_i a_{c,i} - m_i g_i$

$\quad \tau_i \leftarrow R^i_{i+1}\tau_{i+1} - f_i \times r_{i,c_i} + \left(R^i_{i+1}f_{i+1}\right) \times r_{i+1,c_i} + I_i\alpha_i + \omega_i \times (I_i\omega_i)$

end for

As can be seen from Algorithm 1, there are two key steps in the Newton-Euler technique - The Forward Recursion, which involves the computation of the angular velocity, angular acceleration and linear acceleration of each link, starting from the first link and moving outwards, and the Backward Recursion, which involves computation of the forces and torques at each link, starting from the n-th link and moving inwards. Figure 4.1 shows a random link and the forces and torques acting on it.
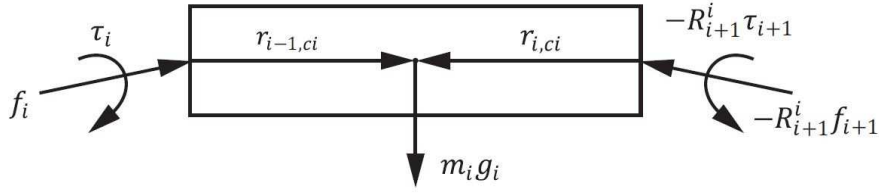
Figure 4.1: Forces and Torques acting on a random link [64]

Notation : The notation used is described as follows :

$a_{c,i}$ — Acceleration of center of mass of link i in frame i.

$a_{e,i}$ — Acceleration of end of link i in frame i.

ω_i — Angular velocity of frame i w.r.t frame i.

α_i — Angular acceleration of frame i w.r.t frame i.

g_i — Acceleration due to gravity in frame i.

f_i — Force exerted by link $i-1$ on link i in frame i.

τ_i — Torque exerted by link $i-1$ on link i in frame i.

R_i^{i+1} — Rotation matrix from frame $i+1$ to frame i.

m_i — Mass of link i.

I_i — Inertia matrix of link i, about a frame parallel to frame i, whose origin is at the center of mass of link i.

r_{i,c_i} — Vector from joint i to the center of mass of link i.

r_{i+1,c_i} — Vector from joint $i+1$ to the center of mass of link i.

$r_{i,i+1}$ — Vector from joint i to joint $i+1$.

4.3   System Description and Modeling

Barrett, the leader in advanced robotic manipulators, provides information about the D-H parameters of the WAM and also about its inertial specifications in its data sheets. However, a dynamic model of the WAM is not disclosed. In our work, we have derived a dynamic model of the Barrett WAM for 4 degree-of-freedom operation. The parameters required for obtaining this model are detailed in this section. Schematics of the Barrett WAM with its 7 revolute joints are shown in Figure 4.2 (copyright has been obtained from Barrett). The necessary D-H parameters of the Barrett WAM are provided in Table 4.1.
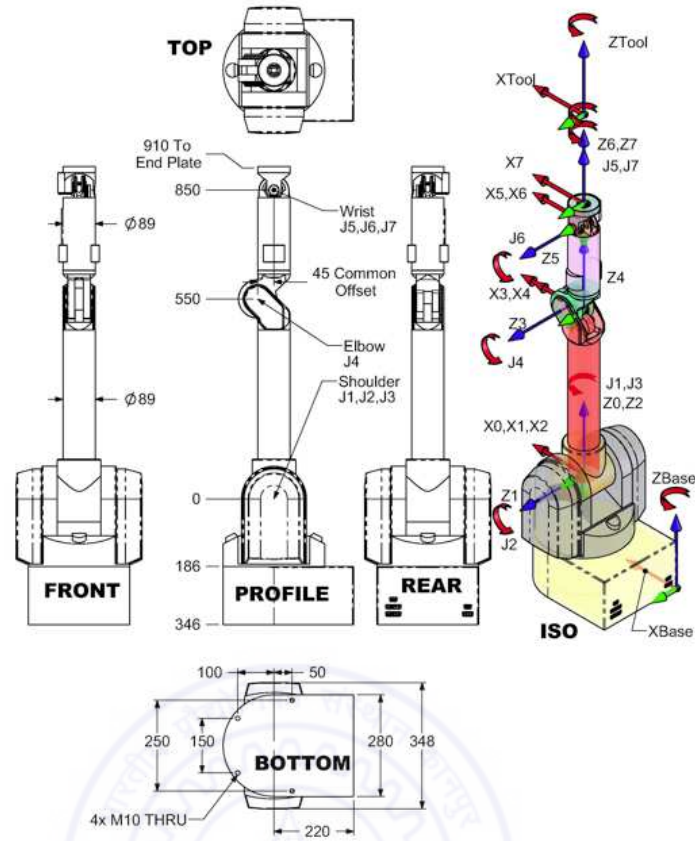
Figure 4.2: WAM 7-DOF dimensions and D-H frames

Table 4.1: D-H Parameters for the 4-DOF Barrett WAM Manipulator

k	a_k (m)	α_k (rad)	d_k (m)	θ_k
1	0	$-\pi/2$	0	θ_1
2	0	$\pi/2$	0	θ_2
3	0.045	$-\pi/2$	0.55	θ_3
4	-0.045	$\pi/2$	0	θ_4

For obtaining the necessary rotation matrices, we use the generalized D-H transform matrix

$$\mathbf{T}_i^{i-1} = \begin{bmatrix} c\theta_i & -s\theta_i c\alpha_i & s\theta_i s\alpha_i & a_i c\theta_i \\ s\theta_i & c\theta_i c\alpha_i & -c\theta_i s\alpha_i & a_i s\theta_i \\ 0 & s\alpha_i & c\alpha_i & d_i \\ 0 & 0 & 0 & 1 \end{bmatrix} \tag{4.3.1}$$

It should be noted that we follow the convention of [64] in our work. c denotes the

cos function and s denotes the sin function. The lengths in the D-H specifications are in meters.

Using equation (4.3.1) and the D-H parameters of the WAM, we derive the following rotation matrices

$$\mathbf{R}_1^0 = \begin{bmatrix} c\theta_1 & 0 & -s\theta_1 \\ s\theta_1 & 0 & c\theta_1 \\ 0 & -1 & 0 \end{bmatrix} \tag{4.3.2}$$

$$\mathbf{R}_2^1 = \begin{bmatrix} c\theta_2 & 0 & s\theta_2 \\ s\theta_2 & 0 & -c\theta_2 \\ 0 & 1 & 0 \end{bmatrix} \tag{4.3.3}$$

$$\mathbf{R}_3^2 = \begin{bmatrix} c\theta_3 & 0 & -s\theta_3 \\ s\theta_3 & 0 & c\theta_3 \\ 0 & -1 & 0 \end{bmatrix} \tag{4.3.4}$$

$$\mathbf{R}_4^3 = \begin{bmatrix} c\theta_4 & 0 & s\theta_4 \\ s\theta_4 & 0 & -c\theta_4 \\ 0 & 1 & 0 \end{bmatrix} \tag{4.3.5}$$

Figure 4.3 shows the different vectors associated with link i. Specifically, we need the link vectors $r_{i,i+1}^i, r_{i,c_i}^i$ and r_{i+1,c_i}^i for $i = 1, 2, 3$ and 4. The superscript i indicates that the vectors need to be expressed in frame i. From the definition of Transformation matrices, we know that the vector $\mathbf{v} = [a_i c\theta_i, a_i s\theta_i, d_i]^T$ represents the vector pointing from Joint i to Joint $i + 1$ expressed in frame $i - 1$. We need to express this vector in frame i. From Figure 4.3, we can see that

$$r_{i,i+1}^i = P_A^i - P_B^i, \tag{4.3.6}$$

where P_A^i and P_B^i represent the position vectors of points A and B in frame i. Now, we know that any random point P_R^{i-1} in frame $i - 1$ is transformed to frame i via the relation

$$\begin{bmatrix} P_R^i \\ 1 \end{bmatrix} = \mathbf{T}_{i-1}^i \begin{bmatrix} P_R^{i-1} \\ 1 \end{bmatrix} \tag{4.3.7}$$

Now, we have

$$\mathbf{T}_{i-1}^i = (\mathbf{T}_i^{i-1})^{-1} = \left[\begin{array}{c:c} \mathbf{R}^T & -\mathbf{R}^T \mathbf{v} \\ \hdashline \mathbf{0} & 1 \end{array} \right], \tag{4.3.8}$$

where $\mathbf{R} = \mathbf{R}_i^{i-1}$. Here, we have used the property that rotation matrices are orthogonal.
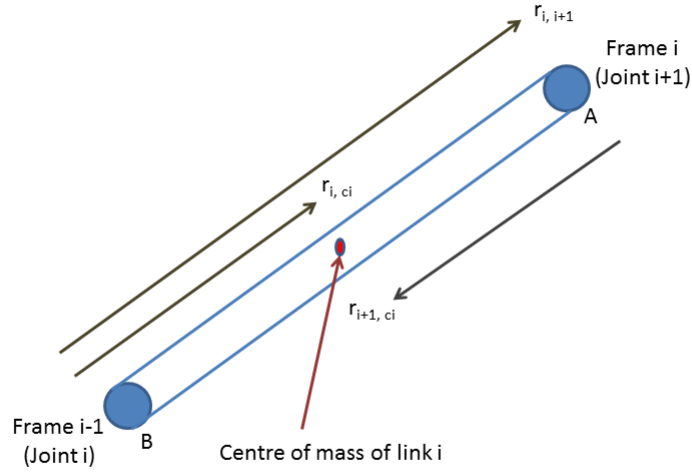
Figure 4.3: Vectors associated with link i

Clearly, $P_B^{i-1} = [0,0,0]^T$ and $P_A^{i-1} = \mathbf{v}$. Using equations (4.3.7) and (4.3.8), we get

$$
\begin{bmatrix} P_B^i \\ 1 \end{bmatrix} = \left[\begin{array}{c|c} \mathbf{R}^T & -\mathbf{R}^T\mathbf{v} \\ \hline \mathbf{0} & 1 \end{array} \right] \begin{bmatrix} 0 \\ 0 \\ 0 \\ 1 \end{bmatrix} = \begin{bmatrix} -\mathbf{R}^T\mathbf{v} \\ 1 \end{bmatrix} \tag{4.3.9}
$$

and

$$
\begin{bmatrix} P_A^i \\ 1 \end{bmatrix} = \left[\begin{array}{c|c} \mathbf{R}^T & -\mathbf{R}^T\mathbf{v} \\ \hline \mathbf{0} & 1 \end{array} \right] \begin{bmatrix} \mathbf{v} \\ 1 \end{bmatrix} = \begin{bmatrix} \mathbf{0} \\ 1 \end{bmatrix} \tag{4.3.10}
$$

Using equations (4.3.6), (4.3.9) and (4.3.10), we get the desired result

$$
r_{i,i+1}^i = \mathbf{R}^T\mathbf{v} = [a_i, d_i s\alpha_i, d_i c\alpha_i]^T \tag{4.3.11}
$$

The inertial specifications of the WAM provides the r_{i+1,c_i}^i vector i.e. the position vector of the centre of mass of link i w.r.t to frame i. From the Figure 4.3, we see that the following relation holds

$$
r_{i,c_i}^i = r_{i,i+1}^i + r_{i+1,c_i}^i \tag{4.3.12}
$$

Equations (4.3.11) and (4.3.12) can be used to find the necessary link vectors. Using these equations, the link vectors so obtained are tabulated in Table 4.2. The link masses are - $m_1 = 8.3936$ kg, $m_2 = 4.8487$ kg, $m_3 = 1.7251$ kg and $m_4 = 1.0912$ kg. It should

Table 4.2: Link Vectors

i	r^i_{i+1,c_i} (in mm)	r^i_{i,c_i} (in mm)	$r^i_{i,i+1}$ (in mm)
1	$[0.3506, 132.6795, 0.6286]^T$	$[0.3506, 132.6795, 0.6286]^T$	$[0, 0, 0]^T$
2	$[-0.223, -21.3924, 13.3754]^T$	$[-0.223, -21.3924, 13.3754]^T$	$[0, 0, 0]^T$
3	$[-38.7565, 217.9078, 0.0252]^T$	$[6.2435, -332.0922, 0.0252]^T$	$[45, -550, 0]^T$
4	$[6.2895, -0.001, 111.0633]^T$	$[-38.7105, -0.001, 111.0633]^T$	$[-45, 0, 0]^T$

be noted that the masses of the electrical and mechanical cables are not included in the
inertial specifications. This data is obtained from the inertial specifications of the Barrett
WAM. We also obtain the following inertia matrices from the same source -

$$I_1 = 10^{-6} \begin{bmatrix} 95157.4294 & 246.1404 & -95.0183 \\ 246.1404 & 92032.3524 & -962.6725 \\ -95.0183 & -962.6725 & 59290.5997 \end{bmatrix} \tag{4.3.13}$$

$$I_2 = 10^{-6} \begin{bmatrix} 29326.8098 & -43.3994 & -129.2942 \\ -43.3994 & 20781.5826 & 1348.6924 \\ -129.2942 & 1348.6924 & 22807.3271 \end{bmatrix} \tag{4.3.14}$$

$$I_3 = 10^{-6} \begin{bmatrix} 56662.2970 & -2321.6892 & 8.2125 \\ -2321.6892 & 3158.0509 & -16.6307 \\ 8.2125 & -16.6307 & 56806.6024 \end{bmatrix} \tag{4.3.15}$$

$$I_4 = 10^{-6} \begin{bmatrix} 18890.7885 & -0.8092 & -1721.2915 \\ -0.8092 & 19340.5969 & 17.8241 \\ -1721.2915 & 17.8241 & 2026.8453 \end{bmatrix} \tag{4.3.16}$$

It should be noted that the unit of each entry of the above matrices is $kg\text{-}mm^2$. This
completes the necessary system description. Armed with this data, one can implement
Algorithm 1. Two other points need to be mentioned in this regard. For forward recursion,
the vector $z_0 = [0, 0, 1]^T$ and for backward recursion, the vector $g_0 = [0, 0, -g]^T$, where g
is the acceleration due to gravity. These results follow directly from the way in which the
frames are assigned.

The implementation of the Newton-Euler algorithm has been done using the software
Maple. The choice was justified by the ability of Maple to carry out heavy symbolic
calculations. The Maple code used for deriving the model is provided here [2] [link]. The
M, C and G matrices necessary for state-space representation are also derived using this

code. For testing our control laws in a simulation environment, we have used the Matlab platform. Thus, the model derived in Maple has been imported to Matlab. The Maple to Matlab conversion has also been demonstrated in the Maple code. It should be noted that this code can be used to derive rigid body models for a generalized n-link manipulator with revolute joints.

Note -

- The D-H specifications can be obtained here [link].

- The Barrett Arm Inertial Specifications are available here [link].

4.4 Experimental Validation

4.4.1 State Space Representation

The standard model representing the dynamics of the robotic system as obtained via the Newton Euler technique is

$$\mathbf{M}(\mathbf{q})\ddot{\mathbf{q}} + \mathbf{C}(\mathbf{q},\dot{\mathbf{q}}) + \mathbf{G}(\mathbf{q}) = \tau \tag{4.4.1}$$

where $\mathbf{q} \in \Re^4$ represents the joint position vector, $\dot{\mathbf{q}} \in \Re^4$ is the joint velocity vector, $\ddot{\mathbf{q}} \in \Re^4$ is the joint acceleration vector, $\mathbf{M}(\mathbf{q}) \in \Re^{4\times4}$ is the symmetric, positive definite inertia matrix, $\mathbf{C}(\mathbf{q},\dot{\mathbf{q}}) \in \Re^4$ is the Coriolis and Centrifugal vector and $\mathbf{G}(\mathbf{q}) \in \Re^4$ is the Gravity vector. τ represents the vector of applied joint torques to the system.

For applying the control techniques, we need to express the model given by (4.4.1) in the standard nonlinear control affine form. To this end, we define the following

$$\mathbf{x} \triangleq [q_1, q_2, q_3, q_4]^T$$
$$\mathbf{z} \triangleq [\dot{q}_1, \dot{q}_2, \dot{q}_3, \dot{q}_4]^T$$
$$\mathbf{f}(\mathbf{x},\mathbf{z}) \triangleq -\mathbf{M}^{-1}(\mathbf{C}+\mathbf{G})$$
$$\mathbf{g}(\mathbf{x}) \triangleq \mathbf{M}^{-1}$$
$$\mathbf{u} \triangleq \tau$$

Based on these notations, the state space model for (4.4.1) becomes

$$\dot{\mathbf{x}} = \mathbf{z}$$
$$\dot{\mathbf{z}} = \mathbf{f}(\mathbf{x},\mathbf{z}) + \mathbf{g}(\mathbf{x})\mathbf{u} \tag{4.4.2}$$

4.4.2   Control Strategies

Backstepping Control Design

Step 1: Design of the virtual control law $\mathbf{z_d}$

The tracking error is defined as $\mathbf{e_1} \triangleq \mathbf{x} - \mathbf{x_d}$. Here $\mathbf{x_d}$ is the reference trajectory. A Lyapunov candidate is chosen as

$$V_1 = \frac{1}{2}\mathbf{e_1}^T\mathbf{e_1} \qquad (4.4.3)$$

The time derivative of this Lyapunov candidate yields

$$
\begin{aligned}
\dot{V}_1 &= \mathbf{e_1}^T\dot{\mathbf{e}}_1 \\
&= \mathbf{e_1}^T(\mathbf{z} - \dot{\mathbf{x}}_\mathbf{d}) \qquad (4.4.4)
\end{aligned}
$$

Let the virtual control law be defined as

$$\mathbf{z_d} \triangleq \dot{\mathbf{x}}_\mathbf{d} - \mathbf{K_1}\mathbf{e_1} \qquad (4.4.5)$$

where $\mathbf{K_1} = diag(k_1, k_2, k_3, k_4)$; k_1, k_2, k_3 and k_4 are positive constants. Let $\mathbf{e_2} \triangleq \mathbf{z} - \mathbf{z_d}$. Using (4.4.4), (4.4.5) and the definition of $\mathbf{e_2}$, we get

$$\dot{V}_1 = -\mathbf{e_1}^T\mathbf{K_1}\mathbf{e_1} + \mathbf{e_1}^T\mathbf{e_2} \qquad (4.4.6)$$

Step 2: Design of the actual control law u

Let the augmented Lyapunov function $V_2(\mathbf{e_1}, \mathbf{e_2})$ be chosen as

$$V_2 = V_1 + \frac{1}{2}\mathbf{e_2}^T\mathbf{e_2} \qquad (4.4.7)$$

Using (4.4.2), the time derivative of this function gives

$$
\begin{aligned}
\dot{V}_2 &= \dot{V}_1 + \mathbf{e_2}^T\dot{\mathbf{e}}_2 \\
&= -\mathbf{e_1}^T\mathbf{K_1}\mathbf{e_1} + \mathbf{e_2}^T\mathbf{e_1} + \mathbf{e_2}^T(\dot{\mathbf{z}} - \dot{\mathbf{z}}_\mathbf{d}) \\
&= -\mathbf{e_1}^T\mathbf{K_1}\mathbf{e_1} + \mathbf{e_2}^T(\mathbf{e_1} + \mathbf{f}(\mathbf{x}, \mathbf{z}) + \mathbf{g}(\mathbf{x})\mathbf{u} - \dot{\mathbf{z}}_\mathbf{d}) \qquad (4.4.8)
\end{aligned}
$$

Let the actual control law be chosen as

$$\mathbf{u} = \mathbf{g}(\mathbf{x})^{-1}(-\mathbf{f}(\mathbf{x}, \mathbf{z}) + \dot{\mathbf{z}}_\mathbf{d} - \mathbf{e_1} - \mathbf{K_2}\mathbf{e_2}) \qquad (4.4.9)$$

where $\mathbf{K_2} = diag(d_1, d_2, d_3, d_4)$; d_1, d_2, d_3 and d_4 are positive constants. From (4.4.8) and (4.4.9), we have

$$\dot{V}_2 = -\mathbf{e_1}^T\mathbf{K_1}\mathbf{e_1} - \mathbf{e_2}^T\mathbf{K_2}\mathbf{e_2} < 0 \qquad (4.4.10)$$

as $\mathbf{K_1}$ and $\mathbf{K_2}$ are positive definite matrices. Thus, the system is shown to be asymptotically stable in the sense of Lyapunov. This would imply that as $t \to \infty, \mathbf{e_1}, \mathbf{e_2} \to 0$. Thus, perfect tracking would be established. The control law as given by (4.4.9) can be expressed in terms of the state variables and the system parameters as

$$\mathbf{u} = (\mathbf{C} + \mathbf{G}) + \mathbf{M}(\ddot{\mathbf{x}}_\mathbf{d} - (\mathbf{K_1} + \mathbf{K_2})(\mathbf{z} - \dot{\mathbf{x}}_\mathbf{d})$$
$$-(\mathbf{I} + \mathbf{K_1}\mathbf{K_2})(\mathbf{x} - \mathbf{x_d}))$$

(4.4.11)

Sliding Mode Control Design

As mentioned earlier, the main advantage of the SMC methodology over other nonlinear control techniques is its invariance to process dynamics characteristics and external perturbations. This can be established analytically. To this end, we rewrite the state space model given by (4.4.2) by including a matched disturbance vector $\mathbf{d}$. It represents deviations from the nominal model. We base our analysis on two assumptions:

- We use the well-known property of robot dynamics that $||\mathbf{M^{-1}(q)}|| \leq \alpha$, where α is a known bounded positive constant.

- The disturbance vector $\mathbf{d} = [d_1, d_2, d_3, d_4]^T$ is bounded, i.e $|d_i| \leq \beta_i, i = 1, 2, 3, 4$, where β_i is the known bound on the disturbance.

The state space model is rewritten as

$$\dot{\mathbf{x}} = \mathbf{z}$$
$$\dot{\mathbf{z}} = \mathbf{f(x,z)} + \mathbf{g(x)u} + \mathbf{g(x)d}$$

(4.4.12)

Let the tracking error be defined by $\mathbf{e} \triangleq \mathbf{x} - \mathbf{x_d}$. A sliding surface $\mathbf{S}$ is chosen such that

$$\mathbf{S} = \dot{\mathbf{e}} + \boldsymbol{\lambda}\mathbf{e}$$

(4.4.13)

where $\boldsymbol{\lambda} = diag(\lambda_1, \lambda_2, \lambda_3, \lambda_4)$; $\lambda_1, \lambda_2, \lambda_3$ and λ_4 are positive constants.

The objective is to design $\mathbf{u}$ in such a way that $\mathbf{S}$ is driven to zero. Let a Lyapunov function V be defined as

$$V = \frac{1}{2}\mathbf{S^T S}$$

(4.4.14)

The time derivative of V along the closed-loop trajectory gives

$$\dot{V} = \mathbf{S^T \dot{S}}$$
$$= \mathbf{S^T}(\ddot{\mathbf{e}} + \boldsymbol{\lambda}\dot{\mathbf{e}})$$
$$= \mathbf{S^T}(\mathbf{f(x,z)} + \mathbf{g(x)u} + \mathbf{g(x)d} - \ddot{\mathbf{x}}_\mathbf{d} + \boldsymbol{\lambda}(\mathbf{z} - \dot{\mathbf{x}}_\mathbf{d}))$$

(4.4.15)

Let the actual control law be chosen as

$$\mathbf{u} = \mathbf{g(x)}^{-1}(-\mathbf{f(x,z)} + \ddot{\mathbf{x}}_\mathbf{d} - \boldsymbol{\lambda}(\mathbf{z} - \dot{\mathbf{x}}_\mathbf{d}) - \mathbf{Ksgn(S)}) \tag{4.4.16}$$

where $\mathbf{K} = diag(k_1, k_2, k_3, k_4)$; k_1, k_2, k_3 and k_4 are positive constants. The lower bounds on these constants will be ascertained later. Replacing the expression for $\mathbf{u}$ in (4.4.15), we get

$$\begin{aligned}
\dot{V} &= \mathbf{S^T}(\mathbf{g(x)d} - \mathbf{Ksgn(S)}) \\
&= -\sum_{i=1}^{4} k_i |s_i| + \mathbf{S^T M^{-1} d} \\
&\leq -\sum_{i=1}^{4} |s_i|(k_i - \alpha\beta_i) \tag{4.4.17}
\end{aligned}$$

Thus, if the gains of the controller are chosen to satisfy the constraint $k_i > \alpha\beta_i$, then from (4.4.17) it follows that $\dot{V} < 0$. This guarantees the sliding condition and the system becomes asymptotically stable in the sense of Lyapunov. This in turn ensures that the tracking error would converge to zero. The final control law $\mathbf{u}$ can be expressed in terms of the system states and parameters as

$$\mathbf{u} = \mathbf{C} + \mathbf{G} + \mathbf{M}(\ddot{\mathbf{x}}_\mathbf{d} - \boldsymbol{\lambda}(\mathbf{z} - \dot{\mathbf{x}}_\mathbf{d}) - \mathbf{Ksgn(S)}) \tag{4.4.18}$$

Comparing (4.4.18) with (4.4.11), we observe that the control structures for both the control algorithms are very similar except for the discontinuous $\mathbf{Ksgn(S)}$ term in the case of SMC. This is known in literature as the 'hitting law' and it makes the SMC robust to matched perturbations for proper choices of $\mathbf{K}$. However, it also causes the control input to chatter. In order to reduce chattering, we use the Boundary Layer method. The signum function is accordingly replaced by a saturation function $\frac{s_i}{(|s_i|+\epsilon)}$, where ϵ represents the width of the boundary layer.

4.4.3 Experimental Results

Individual Joint Motion Testing

For the first experiment, we perform trajectory tracking on each joint separately i.e for a single run, only one joint is given a trajectory to track while the others are constrained to remain at their initial conditions. This process is repeated for each of the 4 joints for both the control algorithms. Due to the high coupling between the joints, a finite torque is required to keep the 3 constrained joints at their initial positions, while a single joint moves. Each joint in turn is given a sinusoidal trajectory which it needs to track. This

is of the form $\theta_i = A_i \sin(\omega_i t)$. A_i is chosen to be 1 for Joints 1, 2 and 4 and 0.5 for Joint 3. This is because through our experiments we have observed that Joint 3 on an average requires much more torque as compared to the other 3 joints. We have performed experiments for varying angular frequencies ω_i for every joint. It is to be noted that the initial conditions for testing each joint are different (to avoid self collisions) and they are mentioned below

- **For Joint 1**: $[\theta_{10}, \theta_{20}, \theta_{30}, \theta_{40}] = [0, -\frac{\pi}{2}, 0, \pi]$

- **For Joint 2**: $[\theta_{10}, \theta_{20}, \theta_{30}, \theta_{40}] = [0, 0, 0, \pi]$

- **For Joint 3**: $[\theta_{10}, \theta_{20}, \theta_{30}, \theta_{40}] = [0, -\frac{\pi}{2}, 0, \pi]$

- **For Joint 4**: $[\theta_{10}, \theta_{20}, \theta_{30}, \theta_{40}] = [0, -\frac{\pi}{2}, 0, \frac{\pi}{2}]$

Table 4.3 presents a detailed report of this experiment, outlining the Root Mean Square Error (RMSE) and Mean Control Input required for each joint. Although in our formulations we have used the **G** vector, since the system is internally gravity compensated, we present the values of torque over this gravity compensation term i.e. the value of the Sliding Mode/Backstepping Control excluding the gravity term. From the results in Table 4.3, the following observations have been made

- The tracking performance for Joints 1 and 2 are comparable for both the control techniques. However, for Joint 3 in particular, the Sliding Mode Control technique with an RMSE of 3.38 mrad performs much better as compared to Backstepping which has a high RMSE of 43.45 mrad. This can be attributed to the fact that Joint 3 has the highest uncertainty in dynamics associated with it, (the reason why it requires higher control effort as mentioned earlier) and that the Sliding Mode technique is more robust a control scheme as compared to Backstepping.

- The error in tracking is more predominant at the peaks of the sinusoidal trajectory which correspond to reversals in direction of motion.

- It is noted that the control effort for both the control algorithms increases with an increase in operating frequency, which is to be expected as the joints need to be moved faster, necessitating higher values of torques.

- The control efforts for both the techniques are nearly the same.

Table 4.3: Comparison of the two control techniques

Frequency	Backstepping Control								Sliding Mode Control							
	RMSE (in mrad)				Mean Control Input (in N-m)				RMSE (in mrad)				Mean Control Input (in N-m)			
(rad/s)	Jnt.1	Jnt.2	Jnt.3	Jnt.4	Jnt.1	Jnt.2	Jnt.3	Jnt.4	Jnt.1	Jnt.2	Jnt.3	Jnt.4	Jnt.1	Jnt.2	Jnt.3	Jnt.4
0.6	6.0	8.7	40.8	15.0	2.80	3.61	2.05	1.21	8.5	3.4	2.5	10.1	2.76	3.47	2.22	1.30
0.8	7.1	9.5	41.8	15.0	2.86	3.72	2.09	1.22	9.8	7.3	2.9	10.2	2.93	3.69	2.27	1.31
1	8.7	10.7	44.6	15.3	3.04	3.95	2.21	1.27	11.6	14.1	5.0	10.8	3.07	3.87	2.39	1.30
1.2	9.6	12.2	46.6	15.6	3.12	4.08	2.29	1.27	11.8	19.8	3.1	10.7	3.19	4.01	2.48	1.29
Average	7.85	10.27	43.45	15.22	2.96	3.84	2.16	1.24	10.43	11.15	3.38	10.45	2.99	3.76	2.34	1.30

Table 4.4 presents the figures for the case $\omega = 0.8 rad/s$. As was observed from Table 4.3, the tracking performance for Backstepping control for Joint 3 is inferior to that of SMC. Also, it can be seen that the control effort is smoother for Backstepping as compared to that for SMC inspite of using the Boundary Layer technique.

Combined Joint Motion Testing

In this experiment, we study the effect of combined motion of the joints. Each joint is given a sinusoidal trajectory which it has to track. The reference trajectories for each of the joints are as follows:

- $\theta_{1ref} = \sin(0.8t)$

- $\theta_{2ref} = \frac{\pi}{4}\sin(0.8t)$

- $\theta_{3ref} = \frac{1}{2}\sin(0.8t)$

- $\theta_{4ref} = \sin(0.8t)$

The initial condition for this experiment is taken to be $[\theta_{10}, \theta_{20}, \theta_{30}, \theta_{40}] = [0, -\frac{\pi}{4}, 0, \frac{\pi}{2}]$. The trajectory plots for this experiment for SMC and Backstepping are shown in Figures 4.4 and 4.5 respectively. The Mean Control effort and RMSE are shown in Figures 4.6 and 4.7 respectively. It can be seen that the tracking performance is better for every joint in the case of SMC. However, this comes at the cost of higher control effort as is evident from Figure 4.6.
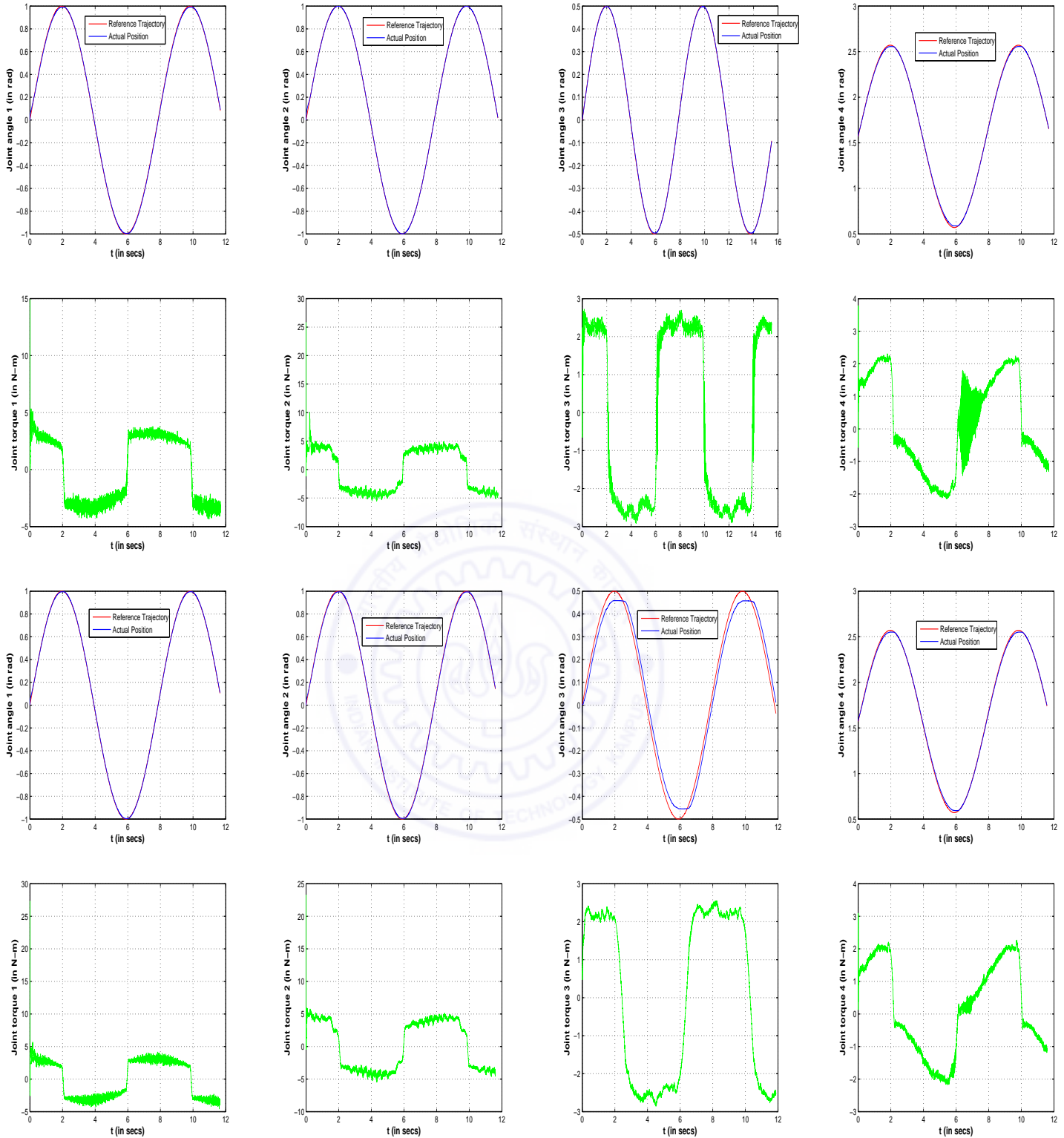
Table 4.4: Details of the First Experiment for $\omega = 0.8rad/s$. Row 1 shows the trajectory responses for each of the four joints for SMC. Row 2 shows the Control efforts for SMC. Row 3 shows the trajectory responses for each of the four joints for Backstepping. Row 4 shows the Control efforts for Backstepping
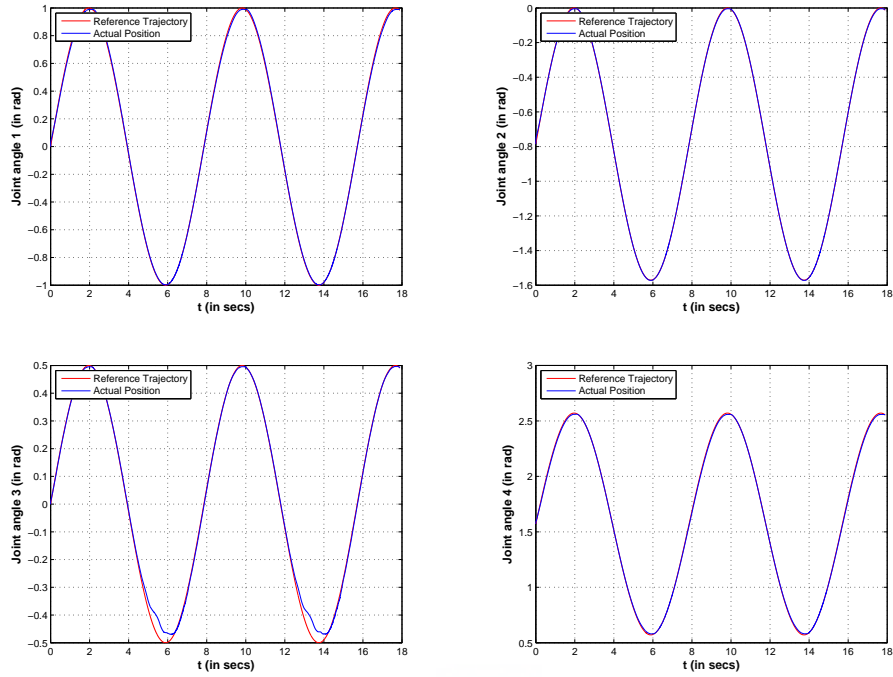
Figure 4.4: Details of Experiment 2: Combined motion of 4 Joints using SMC
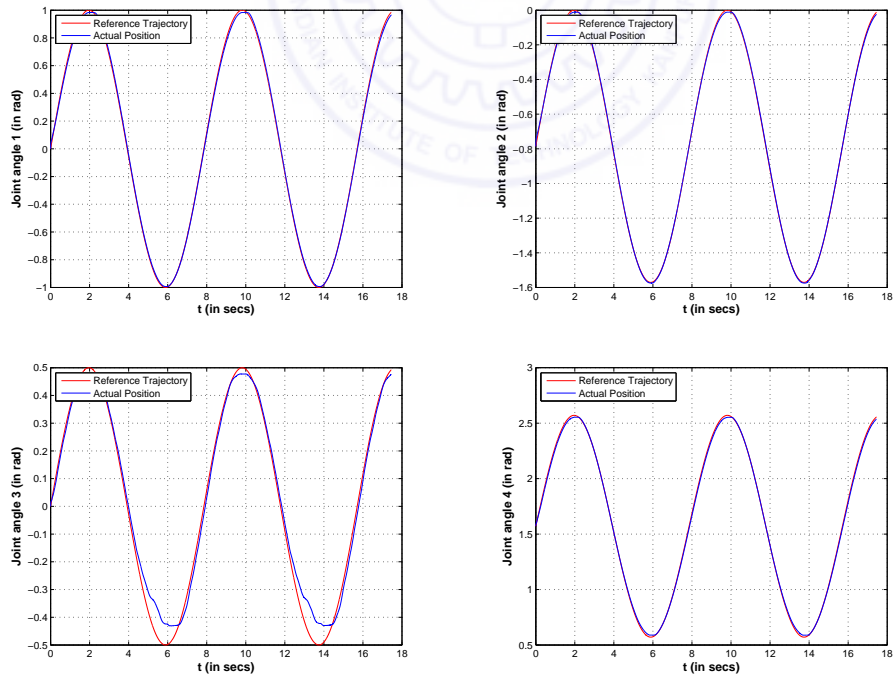
Figure 4.5: Details of Experiment 2: Combined motion of 4 Joints using Backstepping
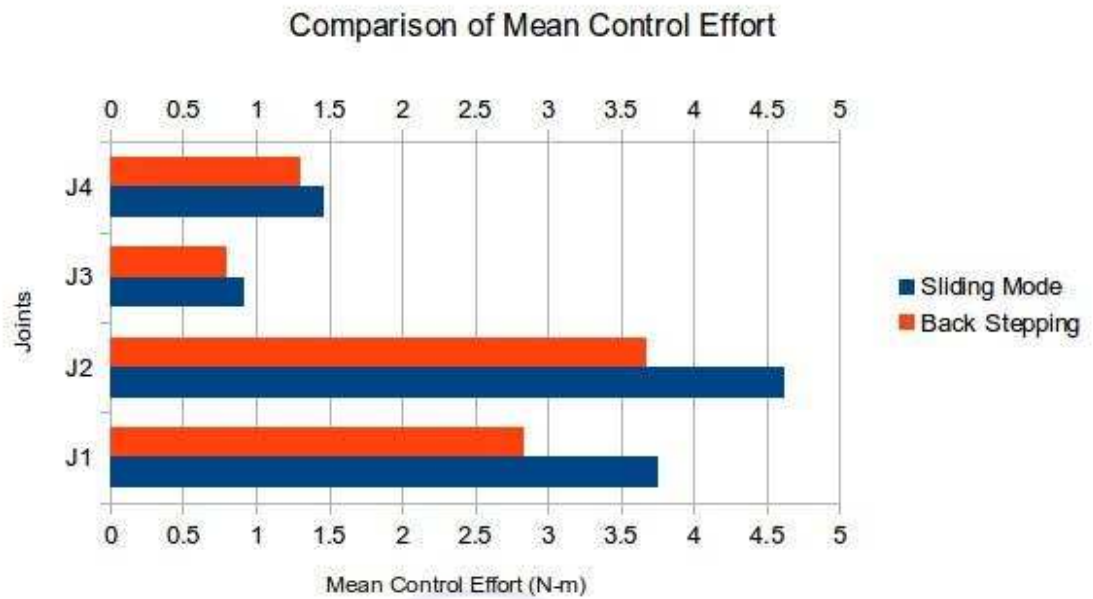
Figure 4.6: Mean control effort comparison for experiment 2
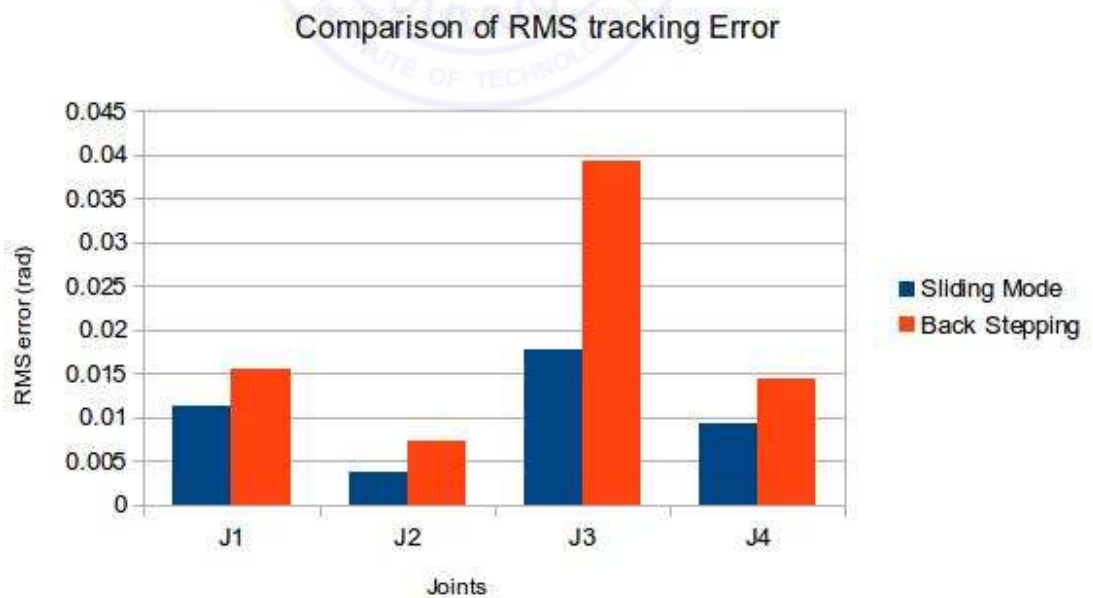
Figure 4.7: RMSE comparison for experiment 2

4.5 Summary

In this chapter, we have developed a dynamic model for 4 DOF operation of the Barrett WAM. The model development procedure along with the system specifications are discussed in detail. This is followed up by experimental validation of the derived model using two popular nonlinear control techniques - Sliding Mode Control and Backstepping. We presented rigorous experimentation results for both, individual joint motion and combined joint motion. The two control strategies are compared in terms of Root Mean Square Error and Mean Control Effort.

Chapter 5

Development of a Nonsingular Fast Terminal Sliding Mode Controller for Computed Torque Control

5.1   Introduction

In this chapter, we develop a Nonsingular Fast Terminal Sliding Mode Control (NFTSMC) technique for control of the 4 DOF Barrett WAM, using the model developed in Chapter 4. We begin by providing the motivation behind using a Terminal Sliding Mode Controller (TSMC) for robotic manipulators, and a background survey of existing TSMC techniques. We then develop a NFTSMC and analyse its finite time convergence. We establish analytically that under some simplifying assumptions, the NFTSMC technique ensures faster convergence as compared to the standard Nonsingular Terminal Sliding Mode Controller existing in literature. Simulation results on a simple 2nd order model are presented to illustrate the main ideas. We extend this scheme to trajectory tracking applications for robotic manipulators. Finally, detailed experimental results are presented to validate the control technique. Figure 5.1 shows the 4 DOF Barrett WAM available in our lab - Intelligent Systems Lab (ISL).

Figure 5.1: The 4 DOF Barrett WAM robot

5.2 Background

Although conventional SMC has been widely explored in a variety of uncertain systems owing to its strong robustness feature, the linear switching manifolds used in SMC lead to asymptotic stability only. This means that the system trajectories will converge to the equilibrium as time goes to infinity. The concept of Terminal Sliding Mode Control (TSMC) was introduced in [90], [87] to overcome this drawback and guarantee finite-time convergence to the equilibrium. With TSMC, the convergence rate grows exponentially as the state approaches the equilibrium. This is the key feature which distinguishes TSMC from SMC and ensures finite-time convergence while retaining the basic robustness features of SMC. This forms the motivation behind using TSMC for tracking applications in robotics, where fast convergence to the equilibrium is highly desirable. We first discuss the development of TSMC over the years, to its most present form.

For this purpose, let us consider a 2nd-order nonlinear dynamical system as follows

$$\dot{x}_1 = x_2$$

$$\dot{x}_2 = f(\mathbf{x}) + g(\mathbf{x})u + d \tag{5.2.1}$$

Here $\mathbf{x} = [x_1, x_2]^T$ represents the system state vector, $f(\mathbf{x})$ and $g(\mathbf{x}) \neq 0$ are smooth nonlinear functions of $\mathbf{x}$, d represents uncertainties and disturbances which satisfy $||d|| < \zeta$ and u is the control input.

5.2.1   Conventional TSMC and Fast TSMC

For this system, the conventional TSM, as developed in [87], is given by the following first-order sliding variable

$$s = x_2 + \beta x_1^{\frac{q}{p}} = 0, \tag{5.2.2}$$

where $\beta > 0$ is a design parameter and p, q are positive odd integers such that $p > q$. Once the states reach the sliding surface, i.e when $s = 0$, the time taken by x_1 to converge to zero is given by

$$t_s = \frac{p}{\beta(p - q)}|x_1(t_r)|^{\frac{p-q}{p}} \tag{5.2.3}$$

Here, $x_1(t_r)$ is the value of the state x_1 at the end of the reaching phase, i.e. when the sliding phase starts (s becomes 0). Although the states converge to zero in finite time, the main problem with this method was that the TSM control law given by

$$u = -g^{-1}(\mathbf{x})\left(f(\mathbf{x}) + \beta\frac{q}{p}x_1^{\frac{q}{p}-1}x_2 + (\zeta + \eta)sgn(s)\right) \tag{5.2.4}$$

suffered from the problem of a singularity. Specifically, the term $x_1^{\frac{q}{p}-1}x_2$ in (5.2.4), could lead to a singularity if $x_2 \neq 0$ and $x_1 = 0$. This follows directly from the fact that $p > q$. The term η in (5.2.4) is a positive gain constant.

It should be noted that compared to the conventional sliding mode scheme, TSM may not offer the same rate of convergence when the system states are far off from the equilibrium point. To overcome this problem, Yu and Man [86], [88] proposed a fast terminal sliding mode (FTSM) scheme where the sliding variable was defined by

$$s = x_2 + \alpha x_1 + \beta x_1^{\frac{q}{p}} = 0 \tag{5.2.5}$$

Here, α, β are positive design constants. However, the control law associated with the FTSM suffered from the same singularity problem.

5.2.2 Nonsingular TSMC

To overcome the problem of singularity in the control input, a few methods have been proposed over the years. Some indirect approaches to avoid the singularity were discussed in [91] and [77]. Feng *et al.* developed the concept of Nonsingular TSM (NTSM) in [24]. The NTSM model is defined by the following sliding variable

$$s = x_1 + \frac{1}{\beta} x_2^{\frac{p}{q}} = 0 \tag{5.2.6}$$

β, p and q have been defined earlier. It was shown that with $1 < \frac{p}{q} < 2$, the states x_1 and x_2 would converge to zero in finite time and the control law would be free of singularities. This NTSM technique has since then been widely used by several researchers in a variety of applications.

  Remark - Expressions (5.2.2), (5.2.5) and (5.2.6) all suffer from a common defect. They contain terms of the type $x^{\frac{q}{p}}$. For $x < 0$, the fractional power $\frac{q}{p}$ may lead to the term $x^{\frac{q}{p}} \notin \Re$. For this reason, S.Yu *et al.* [85] modified the NTSM to have the following form

$$s = x_1 + \frac{1}{\beta} |x_2|^{\frac{p}{q}} sign(x_2) = 0 \tag{5.2.7}$$

Although the TSM function (5.2.7) contains absolute value and signum operators, it is continuous and differentiable. This has been established in [85]. Its first derivative can be expressed as

$$\dot{s} = \dot{x}_1 + \frac{1}{\beta} \frac{p}{q} |x_2|^{\frac{p}{q}-1} \dot{x}_2 \tag{5.2.8}$$

  Notation - Throughout the remainder of this chapter we shall use $sig^{\frac{p}{q}}(x) = |x|^{\frac{p}{q}} sign(x)$, where $x \in \Re$. For a vector $\mathbf{x} = [x_1, \cdots, x_n]^T$, the notation $sig^{\frac{p}{q}}(\mathbf{x})$ represents the vector $sig^{\frac{p}{q}}(\mathbf{x}) = [sig^{\frac{p}{q}}(x_1), \cdots, sig^{\frac{p}{q}}(x_n)]^T$.

5.3 Nonsingular Fast TSMC

Very recently, the concept of Nonsingular Fast TSMC was established by Yang and Yang in [80] . They proposed the following general structure of the NFTSM model

$$s = x + k_1 sig^{a_1}(x) + k_2 sig^{a_2}(\dot{x}) = 0, \tag{5.3.1}$$

where $k_1, k_2 > 0$, $1 < a_2 < 2$, and $a_1 > a_2$. The NFTSM concept draws from the idea of the FTSM and ensures a high convergence rate when the state x is both near and far from the equilibrium point. It also ensures a control law which is free of singularities. The

settling time, t_s, is in the form of a Gauss' Hypergeometric function which is convergent if the parameters k_1, k_2, a_1 and a_2 are chosen in a way as has been described earlier.

Inspired by (5.2.7) and (5.3.1), for the system described by (5.2.1), we use the following structure for the sliding variable

$$s = x_1 + \alpha sig^{\frac{p}{q}}(x_1) + \frac{1}{\beta} sig^{\frac{p}{q}}(x_2) = 0, \tag{5.3.2}$$

where α and β are design parameters.

Note - Unlike (5.3.1), in the sliding variable proposed by us, $a_1 = a_2 = \frac{p}{q}$. The choice of this sliding variable will be justified through simulations and experimental results on the Barrett WAM. First, we investigate the finite time convergence of the proposed NFTSM. A simplifying assumption that leads to a constraint on the design parameter α will help us analyse the time of convergence and obtain an approximate expression for the settling time t_s.

5.3.1 Analysis of Time of Convergence

In this section, we analyse the time of convergence of the state x_1. Once the states reach the sliding surface $s = 0$, we obtain the following nonlinear differential equation

$$\dot{x}_1 = -\beta^{\frac{q}{p}} sig^{\frac{q}{p}}(x_1 + \alpha x_1^{\frac{p}{q}}) \tag{5.3.3}$$

Proposition - Let the state x_1 be bounded with a known bound ρ such that $|x_1| < \rho$. Let the following constraints be imposed

$$\alpha = \frac{1}{\rho^{\frac{p}{q}-1}} \tag{5.3.4}$$

and $1 < \frac{p}{q} < 2$.

Under these constraints, starting from any initial non-zero state $x_1(0)$, the time of convergence required using the NFTSM model described in (5.3.2), is always lesser than the time of convergence using the standard NTSM model given by (5.2.6).

Proof. From (5.3.3), we find that the settling time required for the NFTSM model is given by

$$t_s = \int_0^{|x_1(0)|} \frac{dx_1}{\beta^{\frac{q}{p}} \left(x_1 + \alpha x_1^{\frac{p}{q}}\right)^{\frac{q}{p}}} \tag{5.3.5}$$

Using a binomial series expansion, we obtain

$$
\frac{1}{\left(x_1 + \alpha x_1^{\frac{p}{q}}\right)^{\frac{q}{p}}} = x_1^{-\frac{q}{p}}\left(1 + \alpha x_1^{\frac{p}{q}-1}\right)^{-\frac{q}{p}}
$$

$$
= x_1^{-\frac{q}{p}}\left(1 + \sum_{n=1}^{\infty}\binom{m}{n}(\alpha x_1^{\frac{p}{q}-1})^n\right), \tag{5.3.6}
$$

where $m = -\frac{q}{p}$ and $\binom{m}{n} = \frac{m(m-1)\cdots(m-(n-1))}{n!}$. Substituting (5.3.6) in (5.3.5), we obtain

$$
t_s = \frac{1}{\beta^{\frac{q}{p}}}\int_0^{|x_1(0)|}\left(x_1^{-\frac{q}{p}} + \sum_{n=1}^{\infty}\binom{m}{n}\alpha^n x_1^{\frac{np}{q}-n-\frac{q}{p}}\right)\; dx_1 \tag{5.3.7}
$$

Performing the integration, we obtain

$$
t_s = t_1 + t_2 \tag{5.3.8}
$$

where

$$
t_1 = \frac{1}{\beta^{\frac{q}{p}}}\frac{|x_1(0)|^{1-\frac{q}{p}}}{(1-\frac{q}{p})} \tag{5.3.9}
$$

and

$$
t_2 = \frac{1}{\beta^{\frac{q}{p}}}\sum_{n=1}^{\infty}\binom{m}{n}\frac{\alpha^n |x_1(0)|^{\frac{np}{q}-\frac{q}{p}-n+1}}{(\frac{np}{q}-\frac{q}{p}-n+1)} \tag{5.3.10}
$$

To show that t_2 converges, we use the Ratio test for convergence of infinite series. Let a_n represent the n-th term of the infinite series given by (5.3.10). Then, we have

$$
\left|\frac{a_{n+1}}{a_n}\right| = \left|\frac{(\frac{q}{p}+n-1)}{(n+1)}\right|\left|\alpha|x_1(0)|^{\frac{p}{q}-1}\right|\left|\frac{(\frac{np}{q}-\frac{q}{p}-n+1)}{(\frac{np}{q}+\frac{p}{q}-\frac{q}{p}-n)}\right| \tag{5.3.11}
$$

Using the constraint (5.3.4) and taking limits on both sides of (5.3.11), we obtain

$$
\lim_{n\to\infty}\left|\frac{a_{n+1}}{a_n}\right| = \left|\alpha|x_1(0)|^{\frac{p}{q}-1}\right| = \left(\frac{|x_1(0)|}{\rho}\right)^{\frac{p}{q}-1} < 1 \tag{5.3.12}
$$

Thus, from the Ratio test, we can conclude that t_2 converges. As $\frac{1}{2} < \frac{q}{p} < 1$, we have

$$
0 < n - \frac{1}{2} < \frac{q}{p} + n - 1 < n < n+1 \tag{5.3.13}
$$

Thus, $\left|\frac{(\frac{q}{p}+n-1)}{(n+1)}\right| < 1$. Also, $\left|\frac{(\frac{np}{q}-\frac{q}{p}-n+1)}{(\frac{np}{q}+\frac{p}{q}-\frac{q}{p}-n)}\right| < 1$ follows directly from the fact that $\frac{p}{q} > 1$. We have already established that $\left|\alpha|x_1(0)|^{\frac{p}{q}-1}\right| < 1$. Based on these results, we can conclude that for the infinite series given by (5.3.10),

$$
\left|\frac{a_{n+1}}{a_n}\right| < 1 \tag{5.3.14}
$$

It can be seen that in the expression for t_2, $a_1 < 0$ and consecutive terms are of opposite signs. The infinite series can be broken up into pairs of consecutive terms where each pair consists of one positive term and one negative term. The first such pair would consist of a_1 and a_2 with $a_1 < 0$ and $a_2 > 0$. Since $|a_2| < |a_1|$ (based on the result (5.3.14)), we have the sum of the first pair $a_1 + a_2 < 0$. The same logic can be extended to show that the sum of the infinite series, that is, $t_2 < 0$. Thus, using (5.3.8), we obtain

$$t_s < t_1 \tag{5.3.15}$$

The term t_1 is exactly the settling time taken for the NTSM model given by (5.2.7). Thus, we obtain the desired result. This completes the proof. $\qquad\square$

Remark - *The assumption which we make about the state x_1 being bounded, with a priori knowledge of its upper bound, is a reasonable assumption for robotic systems where the position states remain bounded in a tracking or regulation application. x_1, as we will see later on, will represent the tracking error in position. If a control scheme is developed such that it ensures that the tracking error converges to zero asymptotically, then the assumption which we make makes complete sense.*

To gain more insight, we perform a comparative study of the times of convergence of the NFTSM model and the NTSM model. We start with different initial conditions and compare the settling times of the two techniques. Also, the accuracy of the expression derived for the settling time, for the NFTSM method, is checked. For this purpose, we choose upto 3 terms in the expression for t_2 given by (5.3.10). For this simulation study, $p = 5$, $q = 3$, $\beta = 5$ and $\alpha = \frac{1}{|x_1(0)|^{\frac{p}{q}-1}}$. When the state x_1 settles within a tolerance band of 10^{-6}, we stop the simulation.

From Tables 5.1 and 5.2, we clearly see that the NFTSM has a lower settling time. This is in accordance with the theory presented earlier. Also, it is seen that the formula for t_2, when truncated to 3 terms, gives a slightly higher estimation of the settling time t_s. With higher number of terms, a more accurate result is obviously expected.

5.4 Control Synthesis and Stability Analysis

In this section, we develop the Nonsingular Fast Terminal Sliding Mode Controller for the system described by (5.2.1), and analyse the stability of the system when subjected to this control using Lyapunov theory.

Table 5.1: Comparison of convergence times of NTSM and NFTSM

$x_1(0)$	NFTSM settling time (in secs)		NTSM settling time (in secs)
	Formula	Actual	
5	1.605	1.529	1.813
7.5	1.887	1.799	2.129
10	2.118	2.1019	2.385
-2	1.112	1.060	1.258
-4	1.468	1.399	1.649
-8	1.937	1.845	2.182

Theorem 5.4.1. *For system (5.2.1), with the NFTSM given by (5.3.2), if the control is designed as*

$$u = -g^{-1}(\mathbf{x}) \left(f(\mathbf{x}) + \beta \frac{q}{p} sig^{2 - \frac{p}{q}}(x_2)(\alpha \frac{p}{q}|x_1|^{\frac{p}{q}-1} + 1) + (k + \zeta)sgn(s) \right), \quad (5.4.1)$$

where $1 < \frac{p}{q} < 2$, $k > 0$, then the NFTSM manifold (5.3.2) will be reached in finite time. Also, the states x_1 and x_2 will converge to zero in finite time.

Proof. Let us choose the following Lyapunov candidate

$$V = \frac{1}{2}s^2 \qquad (5.4.2)$$

Using (5.3.2), and taking the derivative of s along the system dynamics (5.2.1), we get

$$
\begin{aligned}
\dot{s} &= \dot{x}_1 + \frac{1}{\beta}\frac{p}{q}|x_2|^{\frac{p}{q}-1}\dot{x}_2 + \alpha\frac{p}{q}|x_1|^{\frac{p}{q}-1}\dot{x}_1 \\
&= x_2 + \frac{1}{\beta}\frac{p}{q}|x_2|^{\frac{p}{q}-1}(f(\mathbf{x}) + g(\mathbf{x})u + d) + \alpha\frac{p}{q}|x_1|^{\frac{p}{q}-1}x_2 \\
&= \frac{1}{\beta}\frac{p}{q}|x_2|^{\frac{p}{q}-1}(d - (k + \zeta)sgn(s)) \qquad (5.4.3)
\end{aligned}
$$

Thus,

$$
\begin{aligned}
\dot{V} &= s\dot{s} \\
&= \frac{1}{\beta}\frac{p}{q}|x_2|^{\frac{p}{q}-1}(ds - (k + \zeta)|s|) \\
&\leq -\frac{k}{\beta}\frac{p}{q}|x_2|^{\frac{p}{q}-1}|s| \qquad (5.4.4)
\end{aligned}
$$

Let us define $\rho(x_2) = \frac{k}{\beta}\frac{p}{q}|x_2|^{\frac{p}{q}-1}$. Since k, β, p and q are all positive by definition, we have $\rho(x_2) > 0$ for $x_2 \neq 0$. Thus, $s\dot{s} \leq -\rho(x_2)|s|$ with $\rho(x_2) > 0$ for $x_2 \neq 0$. Thus, for the situation when $x_2 \neq 0$, the Lyapunov stability condition is satisfied. This ensures that the

$x_1(0) = 5$	$x_1(0) = 7.5$	$x_1(0) = 10$

$x_1(0) = -2$	$x_1(0) = -4$	$x_1(0) = -8$
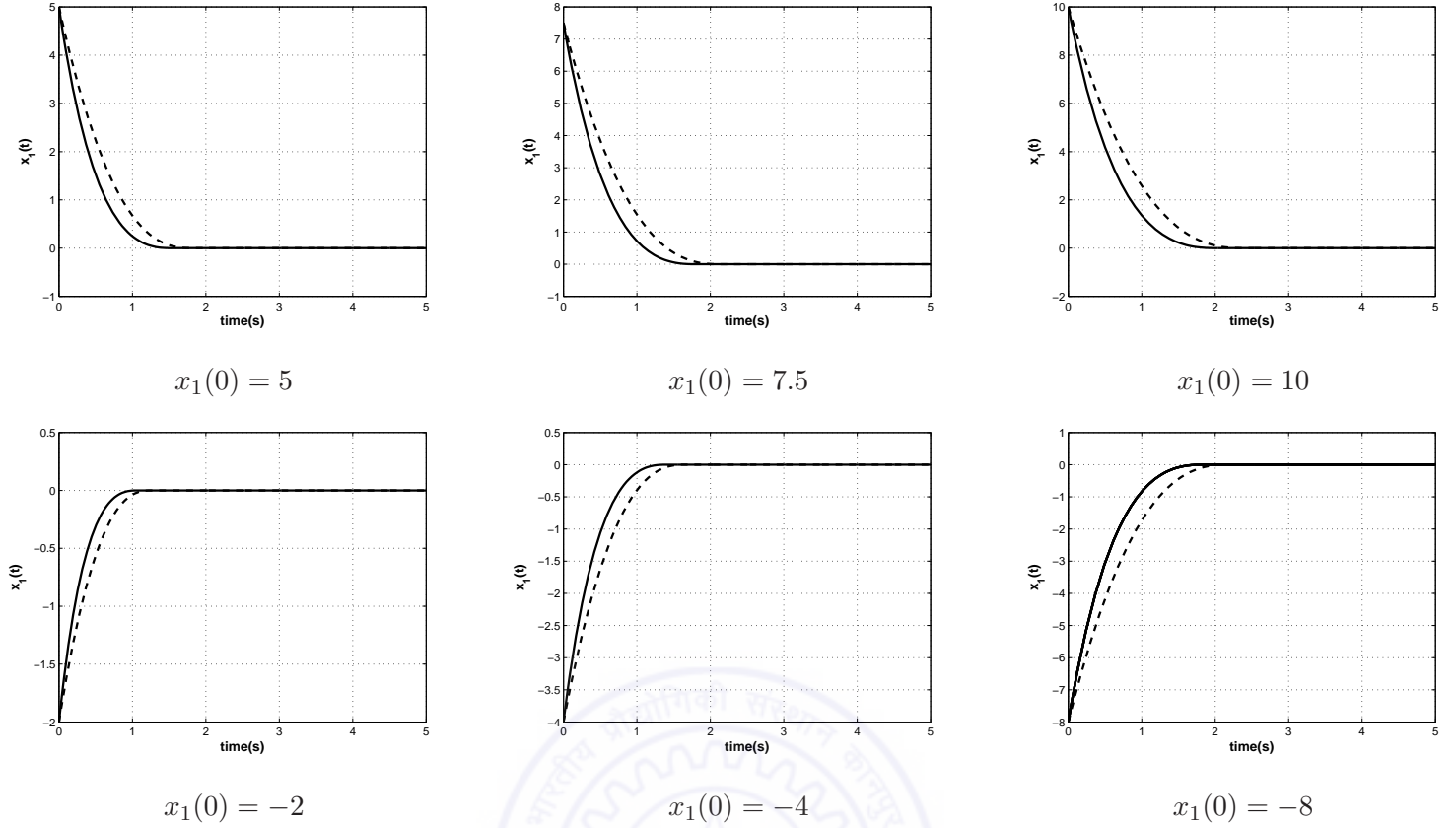
Table 5.2: Comparison of time of convergence of NTSM with NFTSM. The dashed line represents the response of the NTSM model and the bold line represents the response of the NFTSM model.

system states will reach the sliding mode $s = 0$ in finite time. Next, let us analyse the case when $x_2 = 0$. By substituting the control (5.4.1) into the second equation of (5.2.1), we get

$$\dot{x}_2 = d - \beta \frac{q}{p} sig^{2-\frac{p}{q}}(x_2)(\alpha \frac{p}{q}|x_1|^{\frac{p}{q}-1} + 1) - (k + \zeta)sgn(s) \qquad (5.4.5)$$

Thus, for $x_2 = 0$, we get

$$\dot{x}_2 = d - (k + \zeta)sgn(s) \qquad (5.4.6)$$

Thus, we see that $\dot{x}_2 < -k$ and $\dot{x}_2 > k$ for $s > 0$ and $s < 0$, respectively. From the logic presented in [24], it is apparent that ($x_1 \neq 0$ and $x_2 = 0$) is not a terminal attractor and that the sliding mode $s = 0$ can be reached from anywhere in the phase plane in finite time. This completes the proof. $\qquad \Box$

Remark - *It should be noted that in the control law given by (5.4.1), none of the terms have negative fractional powers. Thus, the possibility of a singularity is eliminated with this design. This follows directly from the fact that $1 < \frac{p}{q} < 2$.*

5.4.1   A Simulation study for a 2nd-order system

To test the performance of the NFTSMC, we consider the following 2nd-order nonlinear dynamical system [24] -

$$\begin{aligned} \dot{x}_1 &= x_2 \\ \dot{x}_2 &= 0.1\sin(20t) + u \end{aligned} \tag{5.4.7}$$

The control parameters are chosen as follows : $\beta = 5$, $\alpha = 0.63$, $p = 5$ and $q = 3$. We use the boundary layer concept for minimizing the chattering effect. Thus $sgn(s)$ is approximated by $\frac{s}{(|s|+\epsilon)}$. The width of the boundary layer, ϵ, is chosen to be 0.01. The initial condition for the simulation is $[x_1(0), x_2(0)] = [-0.05, 1]$.

Based on the parameters defined earlier, the sliding surface is given by

$$s = s = x_1 + 0.63 sig^{\frac{5}{3}}(x_1) + 0.2 sig^{\frac{5}{3}}(x_2) = 0 \tag{5.4.8}$$

The control law is obtained by using equation (5.4.1).

From Table 5.3, we can see that the states indeed converge to zero in finite time. The control effort does not become unbounded, i.e. there is no singularity in the control effort. The chattering in the control can be further reduced by increasing the boundary layer width.

It is interesting to note that even though the states converge to zero in finite time, the control effort u does not vanish at steady state. This is because of the $0.1\sin(20t)$ term in the second part of equation (5.4.7). To balance the effect of this term, at steady state, $u = -0.1\sin(20t)$.
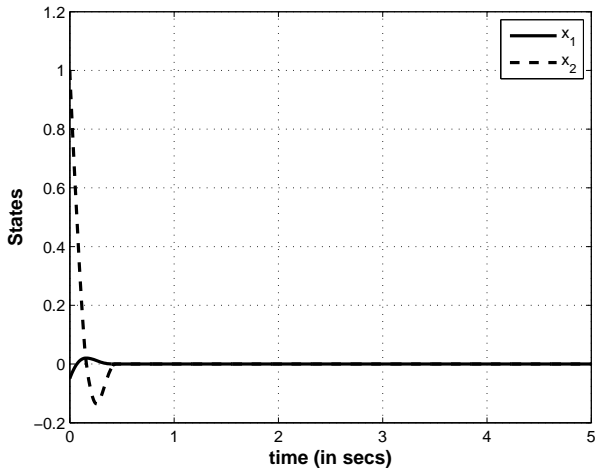
Plot of system states
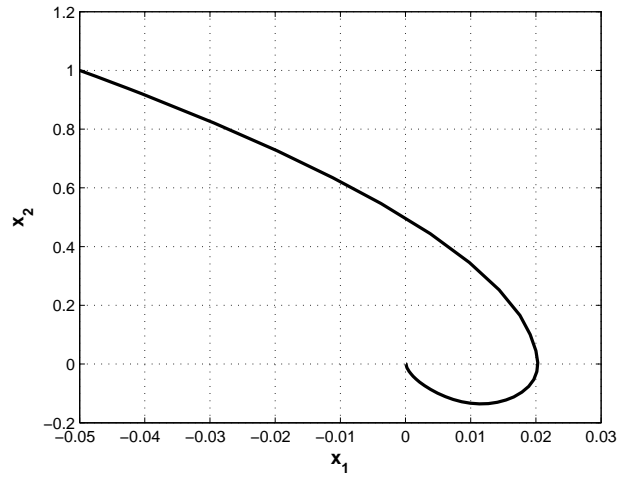
Phase plane plot
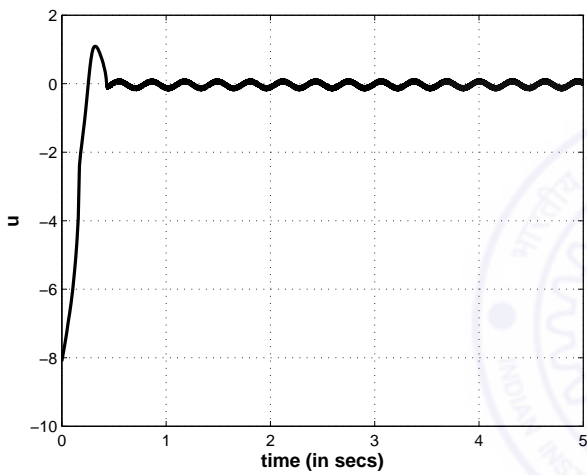
Plot of the control input
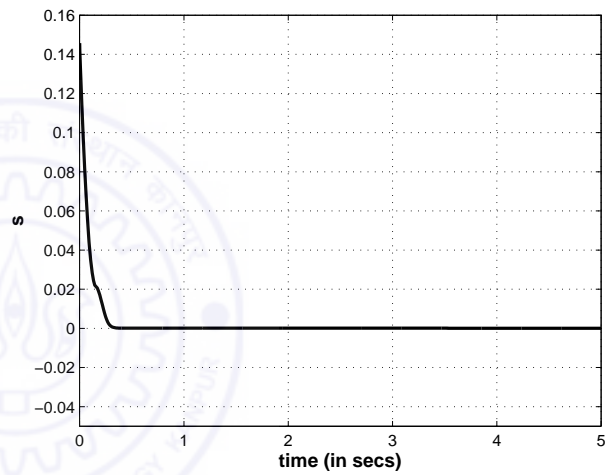
Plot of the sliding variable

Table 5.3: Details of the Simulation Study on the 2nd-order model

5.5 Nonsingular Fast Terminal Sliding Mode Controller for the 4 DOF WAM

For the control design, we use the state space representation which has already been derived from the dynamics of the WAM in Chapter 4. We reproduce it here for convenience

$$
\begin{aligned}
\dot{\mathbf{x}} &= \mathbf{z} \\
\dot{\mathbf{z}} &= \mathbf{f}(\mathbf{x}, \mathbf{z}) + \mathbf{g}(\mathbf{x})\mathbf{u} + \mathbf{d},
\end{aligned}
\tag{5.5.1}
$$

where

$$\mathbf{x} \triangleq [q_1, q_2, q_3, q_4]^T$$

$$\mathbf{z} \triangleq [\dot{q}_1, \dot{q}_2, \dot{q}_3, \dot{q}_4]^T$$

$$\mathbf{f}(\mathbf{x}, \mathbf{z}) \triangleq -\mathbf{M}^{-1}(\mathbf{C} + \mathbf{G})$$

$$\mathbf{g}(\mathbf{x}) \triangleq \mathbf{M}^{-1}$$

$$\mathbf{u} \triangleq \boldsymbol{\tau}$$

We work with the assumptions that

- $||\mathbf{M}^{-1}(\mathbf{q})|| = ||\mathbf{g}(\mathbf{x})|| \leq \rho$, where ρ is a known bounded positive constant.

- The disturbance vector $\mathbf{d} = [d_1, d_2, d_3, d_4]^T$ is bounded, i.e $||\mathbf{d}|| \leq \gamma$, where γ is the known bound on the disturbance.

Let the tracking error be defined by $\mathbf{e} \triangleq \mathbf{x} - \mathbf{x_d}$. A sliding surface $\mathbf{S}$ is chosen according to the NFTSM concept and it is given by

$$\mathbf{S} = \mathbf{e} + \mathbf{A} sig^{\frac{p}{q}}(\mathbf{e}) + \mathbf{B} sig^{\frac{p}{q}}(\dot{\mathbf{e}}), \tag{5.5.2}$$

where $\mathbf{A} = diag(\alpha_1, \alpha_2, \alpha_3, \alpha_4)$ and $\mathbf{B} = diag(\frac{1}{\beta_1}, \frac{1}{\beta_2}, \frac{1}{\beta_3}, \frac{1}{\beta_4})$ are the design matrices. The entries of $\mathbf{A}$ and $\mathbf{B}$ are all positive. p and q are positive odd integers satisfying $1 < \frac{p}{q} < 2$. In light of the analysis performed previously on the convergence time of the NFTSM model, the gain α_i is chosen to satisfy

$$\alpha_i = \frac{1}{(\max |e_i|)^{\frac{p}{q}-1}}$$

The objective is to design $\mathbf{u}$ in such a way that $\mathbf{S}$ is driven to zero.

Theorem 5.5.1. *For the state space model of the Barrett WAM represented by (5.5.1), if the NFTSM manifold is chosen as (5.5.2), and the NFTSM control is designed as*

$$\mathbf{u} = \mathbf{M}\ddot{\mathbf{x}}_\mathbf{d} + \mathbf{C} + \mathbf{G} - \mathbf{M}\mathbf{B}^{-1}\left(\frac{q}{p}\mathbf{I}_4 + \mathbf{A}\boldsymbol{\Lambda_2}\right) sig^{2-\frac{p}{q}}(\dot{\mathbf{e}}) - \mathbf{M}(\mathbf{K} + \rho\gamma\mathbf{I_4})\frac{\mathbf{S}}{||\mathbf{S}||}, \tag{5.5.3}$$

where $\mathbf{x_d}$ is the reference trajectory, $\mathbf{I}_4$ is the identity matrix of dimension 4 , $\boldsymbol{\Lambda}_2$ is a diagonal matrix with $\boldsymbol{\Lambda}_2(i, i) = |e_i|^{\frac{p}{q}-1}$ and $\mathbf{K}$ is the diagonal gain matrix with $k_i > 0$, then fast finite time convergence to $\mathbf{S} = 0$ is ensured, and the states $\mathbf{x}$ and $\mathbf{z}$ also converge to zero in finite time.

Proof. Let us consider the following Lyapunov function

$$V = \frac{1}{2}\mathbf{S}^T\mathbf{S} \tag{5.5.4}$$

The derivative of the NFTSM manifold $\mathbf{S}$ (5.5.2), along the system dynamics (5.5.1), gives

$$
\begin{aligned}
\dot{\mathbf{S}} &= \dot{\mathbf{e}} + \frac{p}{q}\mathbf{A}\mathbf{\Lambda_2}\dot{\mathbf{e}} + \frac{p}{q}\mathbf{B}\mathbf{\Lambda_1}\ddot{\mathbf{e}} \\
&= \left(\mathbf{I}_4 + \frac{p}{q}\mathbf{A}\mathbf{\Lambda_2}\right)\dot{\mathbf{e}} + \frac{p}{q}\mathbf{B}\mathbf{\Lambda_1}\left(\mathbf{f} + \mathbf{g}\mathbf{u} + \mathbf{g}\mathbf{d} - \ddot{\mathbf{q}}_{\mathbf{r}}\right) \\
&= \frac{p}{q}\mathbf{B}\mathbf{\Lambda_1}\left(\mathbf{g}\mathbf{d} - (\mathbf{K} + \rho\gamma\mathbf{I_4})\frac{\mathbf{S}}{||\mathbf{S}||}\right)
\end{aligned}
\tag{5.5.5}
$$

In the above equations $\mathbf{\Lambda}_1$ is a diagonal matrix with $\mathbf{\Lambda}_1(i,i) = |\dot{e}_i|^{\frac{p}{q}-1}$. Using (5.5.5), the derivative of V becomes

$$
\begin{aligned}
\dot{V} &= \mathbf{S^T}\dot{\mathbf{S}} \\
&= \mathbf{S}^T\frac{p}{q}\mathbf{B}\mathbf{\Lambda_1}\left(\mathbf{g}\mathbf{d} - (\mathbf{K} + \rho\gamma\mathbf{I_4})\frac{\mathbf{S}}{||\mathbf{S}||}\right) \\
&\leq -\min_{i=1,2,3,4}(\frac{k_i}{\beta_i}|\dot{e}_i|^{\frac{p}{q}-1})\frac{p}{q}||S||
\end{aligned}
\tag{5.5.6}
$$

Let us define

$$
\psi(\dot{\mathbf{e}}) = \min_{i=1,2,3,4}(\frac{k_i}{\beta_i}|\dot{e}_i|^{\frac{p}{q}-1})\sqrt{2}\frac{p}{q}
\tag{5.5.7}
$$

Thus, from (5.5.6), we get

$$
\dot{V} \leq -\psi V^{\frac{1}{2}}
\tag{5.5.8}
$$

We use the Comparison Lemma [30], and follow the same line of argument as in Theorem 5.4.1, to conclude that the sliding manifold $\mathbf{S} = 0$ will be reached in finite time. This in turn ensures that the states $\mathbf{x}$ and $\mathbf{z}$ will converge to zero in finite time. $\qquad\square$

5.6 Simulation and Experimental results

In this section, we present a comparative study of simulation and experimentation performed on the Barrett WAM, using the NFTSMC scheme developed in the previous section. We start with individual joint tracking experiments. This concept has already been explained in Chapter 4. Each joint is given a sinusoidal trajectory to track at various angular frequencies, while the movements of the other joints are constrained. The initial conditions for testing the joints are as follows

- **For Joint 1**: $[\theta_{10}, \theta_{20}, \theta_{30}, \theta_{40}] = [0, -\frac{\pi}{2}, 0, \pi]$

- **For Joint 2**: $[\theta_{10}, \theta_{20}, \theta_{30}, \theta_{40}] = [0, 0, 0, \pi]$

- **For Joint 3**: $[\theta_{10}, \theta_{20}, \theta_{30}, \theta_{40}] = [0, -\frac{\pi}{2}, 0, \frac{\pi}{2}]$

Table 5.4: Comparison of Simulation and Experimental Data

Frequency	Simulation Data								Experimental Data							
	RMSE (in mrad)				Mean Control Input (in N-m)				RMSE (in mrad)				Mean Control Input (in N-m)			
(rad/s)	Jnt.1	Jnt.2	Jnt.3	Jnt.4	Jnt.1	Jnt.2	Jnt.3	Jnt.4	Jnt.1	Jnt.2	Jnt.3	Jnt.4	Jnt.1	Jnt.2	Jnt.3	Jnt.4
0.6	1.62	0.37	3.15	2.40	0.19	0.19	0.02	0.01	9.6	13.5	8.7	6.5	2.72	3.48	2.46	1.19
0.8	2.81	0.45	5.98	4.60	0.31	0.21	0.03	0.02	10.9	15.0	10.0	7.9	2.87	3.69	2.65	1.27
1	4.63	0.65	5.03	7.68	0.45	0.31	0.04	0.03	12.6	16.3	11.5	9.9	2.99	3.85	2.79	1.37
1.2	5.65	0.79	3.95	1.55	0.61	0.47	0.06	0.05	14.8	18.3	13.4	11.3	3.19	4.01	2.91	1.41

- **For Joint 4**: $[\theta_{10}, \theta_{20}, \theta_{30}, \theta_{40}] = [0, -\frac{\pi}{2}, 0, \frac{\pi}{2}]$

The amplitude of oscillation is set to 1 for all trials. The gain matrix $\mathbf{K}$ is set to $diag(10, 10, 10, 10)$ and the design matrices $\mathbf{A}$ and $\mathbf{B}$ are set to $diag(5, 5, 5, 5)$ and $diag(0.2, 0.2, 0.2, 0.2)$ respectively, for both simulations and experiments. The boundary layer width is chosen to be $\epsilon = 0.01$ for simulations. This parameter requires tuning for the experiments. A lower value of ϵ yields better accuracy at the cost of higher chattering. For experiments on the first 3 joints, ϵ has been set to 0.03. For Joint 4, its value is 0.05. Simulations have been carried out assuming $\mathbf{d} = 0$ i.e. there are no disturbances to the system.

Note - *Since the Barrett WAM has an internal gravity compensation module, the values of Torques (control efforts) presented, do not include the gravity compensation term. To make the simulation study more realistic, we exclude the gravity compensation term for simulations as well.*

5.6.1 Discussion of Results

- Table 5.5 shows the trajectory plots for the various joints and the corresponding control efforts at $\omega = 1$rad/s. From the plots of the trajectories, it is observed that the NFTSMC technique ensures excellent tracking in both simulations and experiments.

- From Table 5.5, we find that in the simulations, a nominal control effort only is required for the tracking. This is mainly because there are no model uncertainties/disturbances to be accounted for. Also, the gravity compensation term has been excluded. The remaining effort required for sinusoidal motion is observed to be nominal in the simulations.
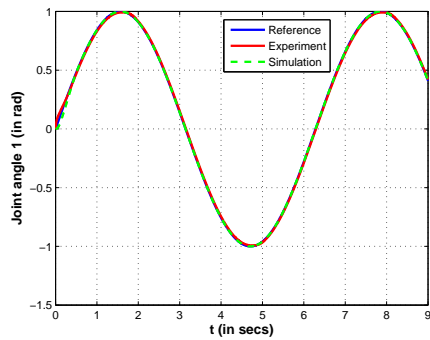
Joint 1 Trajectory
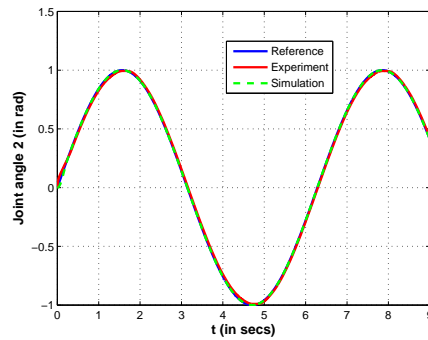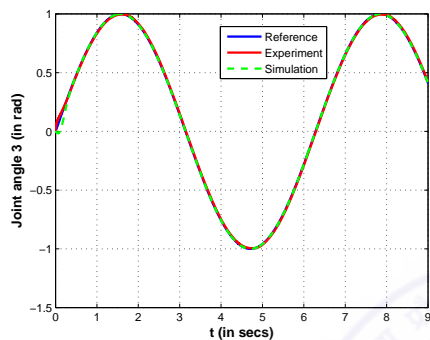
Joint 2 Trajectory

Joint 3 Trajectory
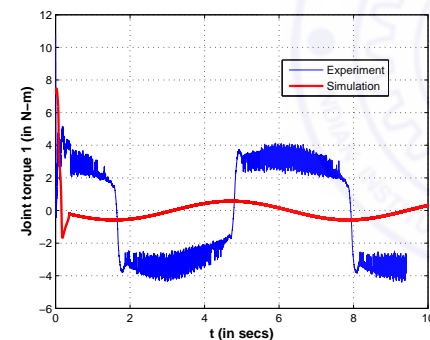
Joint 4 Trajectory
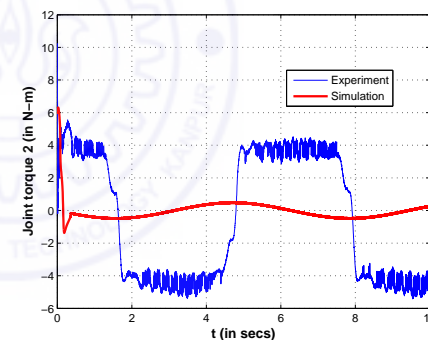
Joint 1 Control
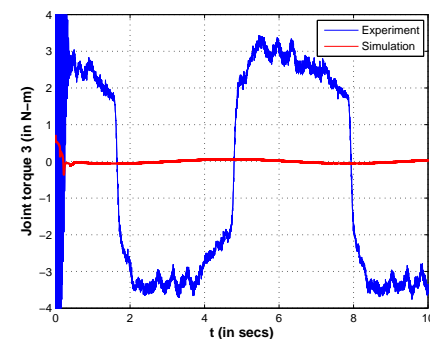
Joint 2 Control
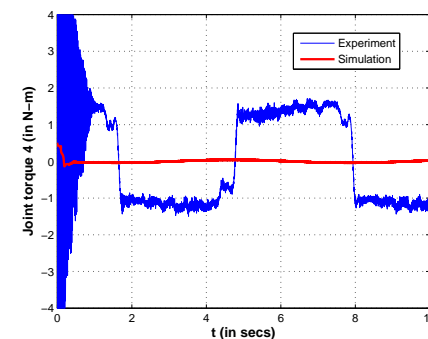
Joint 3 Control

Joint 4 Control

Table 5.5: Details of Simulation and Experimentation on Individual Joint Trajectory Tracking at $\omega = 1$ rad/s.

- The difference between a simulation environment and a real experimental platform is clearly reflected by the difference in control efforts between the corresponding values of simulation and experimental torques. The extra torque required during experiments helps overcome friction and other unmodeled dynamic terms. Thus, one can think of the difference between the corresponding values of simulation and experimental torques to represent the disturbances of the system. It is apparent that the disturbance is not constant, but rather a function of the angular position of the joints.

- Table 5.4 tabulates the Root Mean Square Errors (RMSE) and Mean Control Efforts for all the joints, for different angular frequencies, and gives a quantitative idea of the differences existing between simulations and experiments. As expected, the RMSE is lesser for simulations and so is the required control effort.

- From Table 5.4, one can observe that both the RMSE and the Mean Control Effort increase at higher frequencies of operation.

Next, we perform a combined joint motion testing. The initial positions and reference trajectories are exactly the same as the ones used for the combined motion testing in Chapter 4. The only difference is the angular frequency of testing. In Chapter 4, the results were reported for $\omega = 0.8 rad/s$. Here, the experiments have been performed for $\omega = 1 rad/s$. Table 5.6 shows the results for this experiment. Clearly, the tracking is performed very accurately. A YouTube video which illustrates our experiments is available here [link] [3]. A repository of codes relevant to the modeling and control of the WAM is being stored here [link] [1]. It contains the Maple code for deriving the model, Matlab codes for testing the control actions in simulations, and C++ codes for actual experimentation.
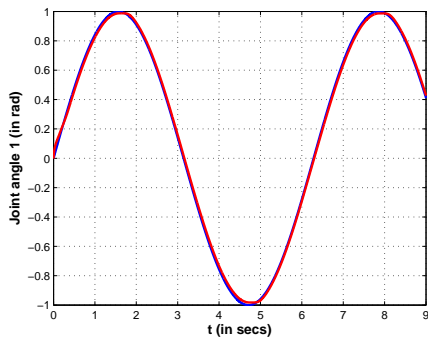
Joint 1 Trajectory
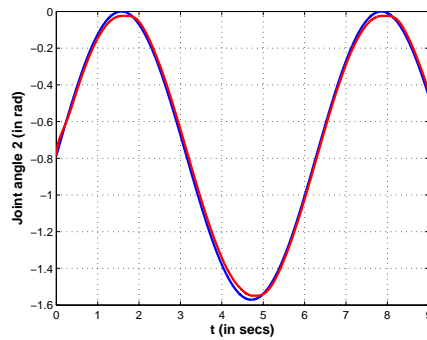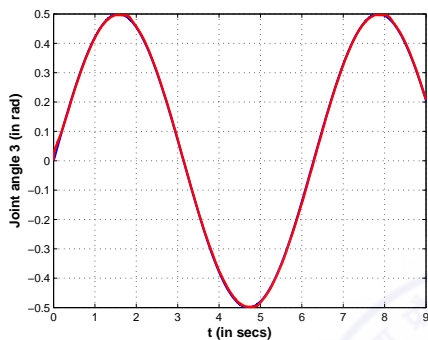
Joint 2 Trajectory
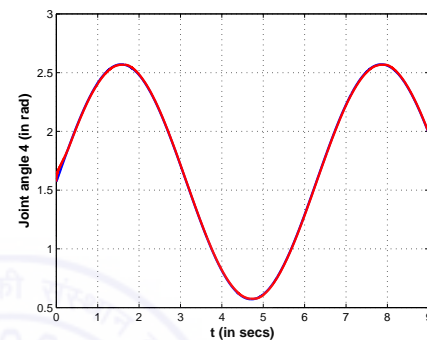
Joint 3 Trajectory

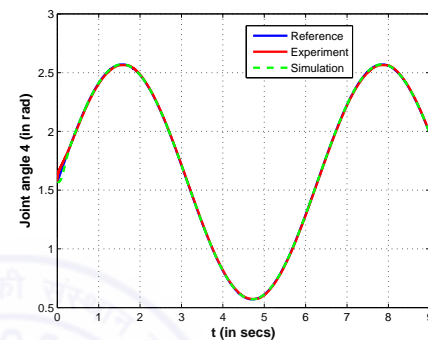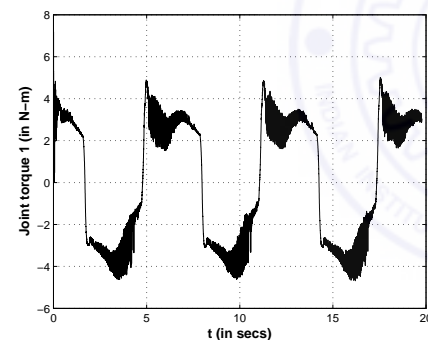Joint 4 Trajectory
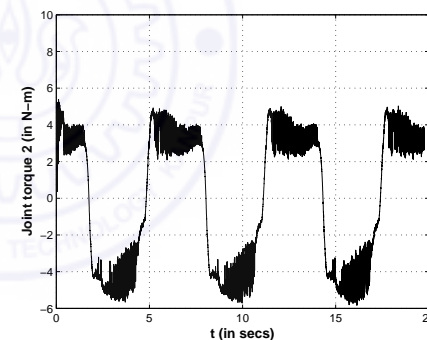
Joint 1 Control
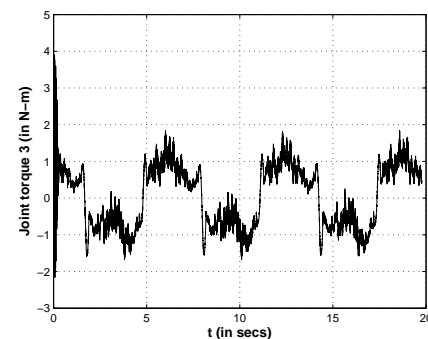
Joint 2 Control
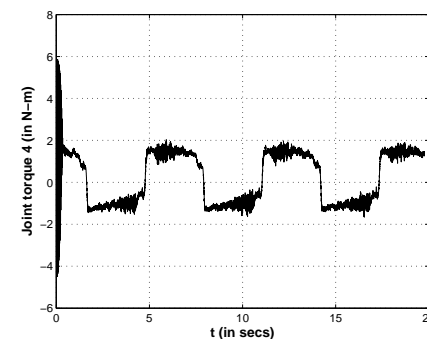
Joint 3 Control

Joint 4 Control

Table 5.6: Details of Experimentation on Combined Joint Trajectory Tracking at $\omega = 1$ rad/s.

5.7 Summary

In this chapter, we have presented a Nonsingular Fast Terminal Sliding Mode Control (NFTSMC) scheme for control of the 4 DOF Barrett WAM. An analytical expression is derived for the error settling time. We have proved that the time of convergence of the proposed scheme is lesser than that of a standard Nonsingular Terminal Sliding Mode Control (NTSMC) scheme which exists in literature. Simulations on simple systems are presented to illustrate the main ideas. This is followed by detailed simulation and experimental results performed on the WAM. The tracking results are found to be very promising. Thus, we have established the feasibility of the NFTSMC scheme for control of the WAM robot.

Chapter 6

Continuous-Time Single Network Adaptive Critic Based Optimal Sliding Mode Control for Nonlinear systems

6.1 Introduction

Integrating the Sliding Mode Control (SMC) theory with Approximate Dynamic Programming (ADP), this chapter presents a novel technique for designing robust optimal sliding mode control schemes for a class of nonlinear control affine systems with disturbances. The main motivation of the work is to merge the inherent robustness of conventional sliding mode control with optimal control theory. Towards this end, a dynamic sliding surface is first used and a control law is defined which guarantees stability in the sense of Lyapunov in the presence of the disturbances. Next, a continuous time single network adaptive critic is used to find an approximate solution to the Hamilton-Jacobi-Bellman (HJB) equation. Since the adaptive critic approximates the optimal cost-to-go function using a parametric positive semi-definite function, the stability of the system is studied during the evolution of weights by employing Lyapunov theory. The merits of the proposed algorithm are demonstrated through simulation examples.

6.2 Background

Sliding Mode Control (SMC) is one of the most effective nonlinear robust control techniques as it makes the system dynamics insensitive to matched disturbances once the system states reach the sliding surface [12, 63, 70, 83] . Usually, stability is the main consideration governing the design of conventional SMC. They are accordingly developed to account for the worst case scenarios when system uncertainties and external disturbances are dominant. However, a majority of real physical processes are well known to us, and hence can be modeled by a dominant nominal part with relatively small uncertainties. For such cases, stability and convergence are not the only issues to be addressed. Optimality issues need to be taken into consideration, which minimize the input energy so as to preclude the possibilities of impracticable control designs.

While optimal control theory provides the methodology to design controllers which are optimal with respect to a defined performance index, the main limitation of such techniques is their sensibility to system uncertainties. This necessitates the requirement of complete system knowledge, which might prove to be difficult in several cases. As SMC is insensitive to uncertainties and external disturbances, combining SMC with optimal control theory can lead to a potential solution to this problem. Such a combination can lead to optimal or sub-optimal control schemes which are more robust. In [84], Young et al. have used the Linear Quadratic (LQ) approach for designing the optimal sliding mode. In [82], Young and Ozguner use co-states of the plant for constructing sliding manifolds, yielding a robust control design for solving linear optimal control problems with fixed terminal time and fixed terminal constraints. In [40], Koshkouei and Zinober have studied frequency shaping linked with linear quadratic optimal control and sliding mode control. However, their method is applicable to only linear time-invariant systems, and the quadratic cost function has only the states as its arguments and does not consider the control input. In [79], Xu and Ozguner incorporated the control effort into the quadratic cost function and presented an optimal sliding mode control approach for linear systems.

While most of the existing literature in optimal sliding mode control is dedicated to linear systems, some recent works have addressed the problem for nonlinear systems as well [22, 60]. In [78], Xu and Ozguner have used three different methods, the Hamilton-Jacobi-Bellman (HJB) equation approach, the Control Lyapunov function approach and the State Dependent Riccati equation approach (SDRE), namely, for finding the optimal sliding mode solution for a class of nonlinear control affine systems. This chapter focuses on the use of Approximate Dynamic Programming for designing optimal sliding mode

controllers.

For a dynamical system with a corresponding performance index, there are two main techniques for solving the associated optimal control problem. They are Pontryagin's minimum principle and Bellman's dynamic programming [15,53]. The continuous time version of Bellman's recurrence equation in dynamic programming is called the Hamilton-Jacobi-Bellman equation, which is a necessary as well as sufficient condition for optimality [15,53]. However, the HJB equation becomes very difficult to solve analytically for even moderately complex systems. To overcome this difficulty, Approximate Dynamic Programming was introduced by Werbos [75]. The ADP formulation leads to the Adaptive Critic architectures which consist of two parametric structures - an actor network which computes a parametrized control law and a critic network which provides guidance on how to update the control law. In [59], Padhi et al. proposed an architecture known as the Single Network Adaptive Critic (SNAC) which simplifies the standard adaptive critic framework by getting rid of the actor network for a class of systems where the control input can be expressed explicitly in terms of state and costate variables. Quite recently, Kumar, Padhi and Behera [42] introduced a continuous-time version of the SNAC architecture which approximates the optimal cost function using a parametric positive semi-definite function and derives a continuous-time weight update law so as to satisfy the HJB equation.

In this chapter, we integrate the continuous time SNAC design with SMC so as to obtain a novel methodology for designing robust optimal sliding mode controllers for a class of nonlinear control affine systems. First, we define the problem at hand and develop a sliding mode controller which guarantees robustness of the system to external disturbances. Next, we use the continuous time SNAC for finding an approximate solution to the HJB equation for a reformulated version of the nominal system without the disturbances. A detailed stability analysis of the entire framework is next presented, which establishes asymptotic stability of the system in the sense of Lyapunov. This is followed up by a summary of the steps to be followed to design controllers based on the proposed algorithm. As motivating examples to demonstrate the merits of the proposed scheme, two simulation studies are presented considering first order and second order nonlinear systems. These are regulation problems. Comparisons are drawn with the conventional SMC and HJB based solutions. Next, we extend the developed theory to a trajectory tracking setting. The proposed technique is applied to a simplified model of the MRI guided micro-robot system which was discussed in Chapters 2 and 3. Simulation results are presented.

6.3 Control Strategy

6.3.1 Problem Statement

Let us consider a class of nonlinear systems described by

$$\begin{aligned}
\dot{x}_i &= x_{i+1}, \quad i = 1, ..., n-1 \\
\dot{x}_n &= f(\mathbf{x}) + u + \zeta
\end{aligned} \tag{6.3.1}$$

where $\mathbf{x} = [x_1, ..., x_n]^T$ is the state vector, f is a smooth function such that $f(0) = 0$ and ζ is a bounded, non-vanishing , exogenous disturbance. The task is to design a control input which minimizes the performance index

$$J = \int_0^\infty [L(\mathbf{x}) + u^2]\, \mathrm{d}t. \tag{6.3.2}$$

where $L(\mathbf{x}) \geq 0$ is a positive semi-definite function of the state $\mathbf{x}$.

6.3.2 Sliding Mode Control Design

The motivation behind using sliding mode control for the system given by (6.3.1) is to obtain robustness against the exogenous disturbance ζ around the equilibrium. This design has been taken up in [2] and we reproduce it here for completeness. An integral sliding mode control design is chosen over the conventional sliding mode control technique, as it adds an extra degree of freedom in designing the controller. A switching function is defined as

$$s = c_1 x_1 + c_2 x_2 + \cdots + c_{n-1} x_{n-1} + x_n + \phi \tag{6.3.3}$$

where $c_i's$ are constant parameters, ϕ is a smooth function to be defined later, and the continuous approximated sliding mode control is given by

$$u = -c_1 x_2 - c_2 x_3 - \cdots - c_{n-1} x_n - f - \dot{\phi} - M\sigma_\epsilon(s) \tag{6.3.4}$$

where $M >$max$|\zeta|$, and $\sigma_\epsilon(\cdot)$ is a saturation function defined as

$$\sigma_\epsilon(s) = \begin{cases} 1 & \text{if } s > \epsilon; \\ \frac{s}{\epsilon} & \text{if } |s| \leq \epsilon; \\ -1 & \text{if } s < -\epsilon. \end{cases} \tag{6.3.5}$$

where ϵ is a small positive constant.

Theorem 6.3.1. *The sliding mode control (6.3.4) will drive and restrict the system
(6.3.1) within a boundary layer $\Omega = \{s||s| < \epsilon\}$ from $t = 0$ even in the presence of the
disturbance ζ, if we enforce $s(0) = 0$ by choosing $\phi(0) = -\sum_{i=1}^{n-1} c_i x_i(0) - x_n(0)$.*

Proof. Let us consider a Lyapunov function candidate

$$V = \frac{1}{2}s^2 \tag{6.3.6}$$

Its derivative with respect to time is given by

$$\begin{aligned}
\dot{V} &= s\dot{s} \\
&= s(\zeta - \frac{M}{\epsilon}s) \\
&= s\zeta - \frac{M}{\epsilon}s^2
\end{aligned} \tag{6.3.7}$$

On the boundary of Ω, $s = |\epsilon|$. Hence, from (6.3.7) we have

$$\begin{aligned}
\dot{V} &= s\zeta - \frac{M}{\epsilon}\epsilon^2 \\
&= \epsilon(|\zeta| - M) \\
&< 0
\end{aligned}$$

Therefore, the sliding mode control design renders the boundary layer Ω an invariant set
of the closed-loop system (6.3.1). Thus, by enforcing $s(0) = 0 \in \Omega$, the evolution of
the closed-loop system will be confined to the boundary layer Ω from $t = 0$, even in the
presence of the exogenous disturbance ζ. □

Since s always stays within the boundary layer, that is, as $|s| \leq \epsilon$, the control input to
the system becomes

$$u = -c_1 x_2 - c_2 x_3 - \cdots - c_{n-1} x_n - f - \dot{\phi} - \frac{M}{\epsilon}s \tag{6.3.8}$$

The control law (6.3.8) guarantees stability of the system in the sense of Lyapunov in
the presence of the disturbances. The next task is to design an update law for ϕ which
minimizes the cost function (6.3.2). For this, we consider the nominal system without
the disturbances. By denoting $x_{n+1} = \phi$, $v = \dot{\phi}$ and $\eta = \frac{M}{\epsilon}$, we reformulate the dynamics
of (6.3.1) as

$$\begin{aligned}
\dot{x}_1 &= x_2 \\
&\vdots \\
\dot{x}_{n-1} &= x_n \\
\dot{x}_n &= -\eta c_1 x_1 - \sum_{i=1}^{n-1}(c_i + \eta c_{i+1})x_{i+1} - \eta x_{n+1} - v \\
\dot{x}_{n+1} &= v
\end{aligned} \tag{6.3.9}$$

where $c_n = 1$.

6.3.3 Continuous Time Single Network Adaptive Critic based Optimal Sliding Mode Control Design

The dynamics of the system (6.3.9) can be expressed in the control-affine form

$$\dot{\bar{\mathbf{x}}} = \mathbf{F}(\bar{\mathbf{x}}) + \mathbf{G}(\bar{\mathbf{x}})v \tag{6.3.10}$$

where $\bar{\mathbf{x}}$ represents the augmented state vector such that $\bar{\mathbf{x}} = [x_1, ..., x_n, x_{n+1}]^T$ and

$$\mathbf{F}(\bar{\mathbf{x}}) = \begin{bmatrix} x_2 \\ \vdots \\ -\eta c_1 x_1 - \sum_{i=1}^{n-1} (c_i + \eta c_{i+1}) x_{i+1} - \eta x_{n+1} \\ 0 \end{bmatrix}, \mathbf{G}(\bar{\mathbf{x}}) = \begin{bmatrix} 0 \\ \vdots \\ 0 \\ -1 \\ 1 \end{bmatrix} \tag{6.3.11}$$

v represents the input to the system (6.3.10) and the performance index (6.3.2) can be written as

$$J(\bar{\mathbf{x}}(0), 0) = \int_0^\infty [L + \bar{f}^2 + 2\bar{f}v + v^2] \, \mathrm{d}t. \tag{6.3.12}$$

where

$$\bar{f} = f + \eta c_1 x_1 + \sum_{i=1}^{n-1} (c_i + \eta c_{i+1}) x_{i+1} + \eta x_{n+1} \tag{6.3.13}$$

Thus, the equivalent problem reduces to an optimal control problem for a control-affine system with a non-quadratic cost functional. The solution to this problem would give the optimal v^*, which can then be used to solve the original optimal sliding mode control problem.

Let $J^*(\bar{\mathbf{x}}^*(t), t)$ be a scalar function representing the optimal value of the performance index J for an initial state $\bar{\mathbf{x}}^*(t)$ at time t.

Let us define a Hamiltonian as

$$H(\bar{\mathbf{x}}, \boldsymbol{\lambda}^*, v) = L + \bar{f}^2 + 2\bar{f}v + v^2 + \boldsymbol{\lambda}^{*T}[\mathbf{F}(\bar{\mathbf{x}}) + \mathbf{G}(\bar{\mathbf{x}})v] \tag{6.3.14}$$

where $\boldsymbol{\lambda}^* = \frac{\partial J^*}{\partial \bar{\mathbf{x}}}$. The optimal control v^* is derived from the necessary condition given by

$$\frac{\partial H}{\partial v} = \frac{\partial}{\partial v}[L + \bar{f}^2 + 2\bar{f}v + v^2] + \boldsymbol{\lambda}^{*T}\frac{\partial}{\partial v}[\mathbf{F}(\bar{\mathbf{x}}) + \mathbf{G}(\bar{\mathbf{x}})v] = 0 \tag{6.3.15}$$

This results in the following expression for the optimal control input to the system (6.3.10)

$$v^* = -\bar{f} - \frac{1}{2}\boldsymbol{\lambda}^{*T}\mathbf{G}(\bar{\mathbf{x}}) = -\bar{f} - \frac{1}{2}\mathbf{G}^T(\bar{\mathbf{x}})\boldsymbol{\lambda}^* \tag{6.3.16}$$

Substituting the value of v^* in (6.3.14), we get

$$H(\bar{\mathbf{x}}^*, \boldsymbol{\lambda}^*, v^*) = L + \bar{f}^2 + 2\bar{f}[-\bar{f} - \frac{1}{2}\mathbf{G}^T(\bar{\mathbf{x}}^*)\boldsymbol{\lambda}^*] + [\bar{f}^2 + \frac{1}{4}\boldsymbol{\lambda}^{*T}\mathbf{G}(\bar{\mathbf{x}}^*)\mathbf{G}^T(\bar{\mathbf{x}}^*)\boldsymbol{\lambda}^* + \bar{f}\mathbf{G}^T(\bar{\mathbf{x}}^*)\boldsymbol{\lambda}^*]$$
$$+ \boldsymbol{\lambda}^{*T}(\mathbf{F}(\bar{\mathbf{x}}^*) + \mathbf{G}(\bar{\mathbf{x}}^*)[-\bar{f} - \frac{1}{2}\mathbf{G}^T(\bar{\mathbf{x}}^*)\boldsymbol{\lambda}^*])$$

$$(6.3.17)$$

On simplification, the expression for the optimal Hamiltonian becomes

$$H^* = L - \frac{1}{4}\boldsymbol{\lambda}^{*T}\mathbf{G}(\bar{\mathbf{x}}^*)\mathbf{G}^T(\bar{\mathbf{x}}^*)\boldsymbol{\lambda}^* + \boldsymbol{\lambda}^{*T}\mathbf{F}(\bar{\mathbf{x}}^*) - \bar{f}\boldsymbol{\lambda}^{*T}\mathbf{G}(\bar{\mathbf{x}}^*) \qquad (6.3.18)$$

Now, the optimal value function $J^*(\bar{\mathbf{x}}^*(t), t)$ must satisfy the *Hamilton-Jacobi-Bellman* (HJB) equation given by

$$\frac{\partial J^*}{\partial t} + \min_{\mathbf{u}} H(\bar{\mathbf{x}}, \frac{\partial J^*}{\partial \bar{\mathbf{x}}}, v, t) = 0 \qquad (6.3.19)$$

Thus, from (6.3.18) and (6.3.19), the optimal value function must satisfy the following nonlinear dynamic equation

$$\frac{\partial J^*}{\partial t} + L - \frac{1}{4}\left(\frac{\partial J^*}{\partial \bar{\mathbf{x}}}\right)^T \mathbf{G}(\bar{\mathbf{x}}^*)\mathbf{G}^T(\bar{\mathbf{x}}^*)\frac{\partial J^*}{\partial \bar{\mathbf{x}}} + \left(\frac{\partial J^*}{\partial \bar{\mathbf{x}}}\right)^T \mathbf{F}(\bar{\mathbf{x}}^*) - \bar{f}\left(\frac{\partial J^*}{\partial \bar{\mathbf{x}}}\right)^T \mathbf{G}(\bar{\mathbf{x}}^*) = 0$$

$$(6.3.20)$$

The above equation is extremely difficult to solve analytically. Thus, an alternate approach is to approximate the optimal value function as follows:

$$V(\bar{\mathbf{x}}, t) = h(\mathbf{w}, \bar{\mathbf{x}}) \qquad (6.3.21)$$

The approximating function $h(\mathbf{w}, \bar{\mathbf{x}})$ is chosen such that it satisfies certain initial conditions which are discussed in the next section. If $h(\mathbf{w}, \bar{\mathbf{x}})$ represents the optimal value function, then it has to satisfy the HJB equation (6.3.19). This yields

$$\frac{\partial V}{\partial t} + \min_{\mathbf{u}} H(\bar{\mathbf{x}}, \frac{\partial V}{\partial \bar{\mathbf{x}}}, v, t) = 0 \qquad (6.3.22)$$

From (6.3.20), (6.3.21) and (6.3.22), we get

$$\frac{\partial V}{\partial t} + L - \frac{1}{4}\left(\frac{\partial V}{\partial \bar{\mathbf{x}}}\right)^T \mathbf{G}\mathbf{G}^T\frac{\partial V}{\partial \bar{\mathbf{x}}} + \left(\frac{\partial V}{\partial \bar{\mathbf{x}}}\right)^T \mathbf{F} - \bar{f}\left(\frac{\partial V}{\partial \bar{\mathbf{x}}}\right)^T \mathbf{G} = 0 \qquad (6.3.23)$$

As $\frac{\partial V}{\partial t} = \left(\frac{\partial h}{\partial \mathbf{w}}\right)^T \dot{\mathbf{w}}$, we get the following weight update law:

$$\left(\frac{\partial h}{\partial \mathbf{w}}\right)^T \dot{\mathbf{w}} = -L + \frac{1}{4}\left(\frac{\partial h}{\partial \bar{\mathbf{x}}}\right)^T \mathbf{G}\mathbf{G}^T\frac{\partial h}{\partial \bar{\mathbf{x}}} - \left(\frac{\partial h}{\partial \bar{\mathbf{x}}}\right)^T \mathbf{F} + \bar{f}\left(\frac{\partial h}{\partial \bar{\mathbf{x}}}\right)^T \mathbf{G} \qquad (6.3.24)$$

However, the scalar equation (6.3.24) represents an *under-determined system of linear equations* where the number of equations is lesser than the number of variables to be

solved for. Out of the infinitely many solutions of this equation, we seek the *minimum norm* solution, i.e the solution which minimizes $||\dot{\mathbf{w}}||_2$. We use the Pseudo-inverse method to compute the solution for $\dot{\mathbf{w}}$.

Equation (6.3.24) can be re-written as

$$\mathbf{S}\dot{\mathbf{w}} = r \tag{6.3.25}$$

where $\mathbf{S} = \left(\frac{\partial h}{\partial \mathbf{w}}\right)^T$ is a row vector and $r = -L + \frac{1}{4}\left(\frac{\partial h}{\partial \bar{\mathbf{x}}}\right)^T \mathbf{G}\mathbf{G}^T \frac{\partial h}{\partial \bar{\mathbf{x}}} - \left(\frac{\partial h}{\partial \bar{\mathbf{x}}}\right)^T \mathbf{F} + \bar{f}\left(\frac{\partial h}{\partial \bar{\mathbf{x}}}\right)^T \mathbf{G}$ is a scalar.

The pseudo-inverse solution to (6.3.25) is given by

$$\dot{\mathbf{w}} = \mathbf{S}^T(\mathbf{S}\mathbf{S}^T)^{-1} r \tag{6.3.26}$$

Remark - *Since* $(\mathbf{S}\mathbf{S}^T)$ *is a scalar, its inverse can easily be computed.*

6.4 Stability Analysis

In this section, we seek to analyse under what conditions the parametrized function $h(\mathbf{w}, \bar{\mathbf{x}})$ and the weight update law associated with it guarantee asymptotic stability in the sense of Lyapunov. It is a well known concept in optimal control theory that every meaningful value function is a Lyapunov function. Since we have chosen $h(\mathbf{w}, \bar{\mathbf{x}})$ to approximate the optimal value function, it serves as a suitable Lyapunov candidate for studying the stability of the proposed scheme. Since $V(\bar{\mathbf{x}}, t) = h(\mathbf{w}, \bar{\mathbf{x}})$, differentiating $V(\bar{\mathbf{x}}, t)$ with respect to time, we obtain

$$\begin{aligned}
\dot{V} &= \frac{\partial V}{\partial t} + \left(\frac{\partial V}{\partial \bar{\mathbf{x}}}\right)^T \dot{\bar{\mathbf{x}}} \\
&= \frac{\partial V}{\partial t} + \left(\frac{\partial V}{\partial \bar{\mathbf{x}}}\right)^T [\mathbf{F} + \mathbf{G}v]
\end{aligned} \tag{6.4.1}$$

Using (6.3.16), (6.3.23) and (6.4.1), we get

$$\dot{V} = -L + \frac{1}{4}\left(\frac{\partial V}{\partial \bar{\mathbf{x}}}\right)^T \mathbf{G}\mathbf{G}^T \frac{\partial V}{\partial \bar{\mathbf{x}}} - \left(\frac{\partial V}{\partial \bar{\mathbf{x}}}\right)^T \mathbf{F} + \bar{f}\left(\frac{\partial V}{\partial \bar{\mathbf{x}}}\right)^T \mathbf{G} + \left(\frac{\partial V}{\partial \bar{\mathbf{x}}}\right)^T (\mathbf{F} + \mathbf{G}[-\bar{f} - \frac{1}{2}\mathbf{G}^T \frac{\partial V}{\partial \bar{\mathbf{x}}}]) \tag{6.4.2}$$

On simplification, we get

$$\dot{V} = -L - \frac{1}{4}\left(\frac{\partial V}{\partial \bar{\mathbf{x}}}\right)^T \mathbf{G}\mathbf{G}^T \frac{\partial V}{\partial \bar{\mathbf{x}}} \tag{6.4.3}$$

Now, L is a positive semi-definite function of the states by definition. Clearly $\dot{V} < 0$ whenever $\bar{\mathbf{x}} \neq 0$. $V(\bar{\mathbf{x}}, t)$ is a function of both the states $\bar{\mathbf{x}}$ and the weights $\mathbf{w}$. Let us

impose a condition on the parametrized function $h(\mathbf{w}, \bar{\mathbf{x}})$ that

$$\frac{\partial V}{\partial \bar{\mathbf{x}}}(\bar{\mathbf{x}}, t) = \frac{\partial h}{\partial \bar{\mathbf{x}}} = 0 \quad \text{when} \quad \bar{\mathbf{x}} = 0 \tag{6.4.4}$$

Thus, $\dot{V} = 0$ when either $\{\bar{\mathbf{x}} = 0, \mathbf{w} = 0\}$ and $\{\bar{\mathbf{x}} = 0, \mathbf{w} \neq 0\}$. Thus, we can conclude that $\dot{V}$ is only negative semi-definite. This ensures the boundedness of $\bar{\mathbf{x}}, \mathbf{w}$ and also of $\dot{\bar{\mathbf{x}}}$. Let us impose a second condition on $V(\bar{\mathbf{x}}, t)$ that it is *lower bounded*. Integrating $\dot{V}$ with respect to time, we get

$$\int_0^t \dot{V} \, d\tau = V(\bar{\mathbf{x}}(t), t) - V(\bar{\mathbf{x}}(0), 0) \tag{6.4.5}$$

As $V(\bar{\mathbf{x}}(0), 0)$ is bounded and $V(\bar{\mathbf{x}}(t), t)$ is bounded and non-increasing, the following result can be obtained

$$\lim_{t \to +\infty} \int_0^t \dot{V} \, d\tau < \infty \tag{6.4.6}$$

Taking the derivative of $\dot{V}$ once again with respect to time, we get

$$\ddot{V} = -\left(\frac{\partial L}{\partial \bar{\mathbf{x}}}\right)^T \dot{\bar{\mathbf{x}}} - \frac{1}{2}\left(\frac{\partial V}{\partial \bar{\mathbf{x}}}\right)^T \mathbf{G}\mathbf{G}^T \frac{\partial^2 V}{\partial t \partial \bar{\mathbf{x}}} - \frac{1}{4}\left(\frac{\partial V}{\partial \bar{\mathbf{x}}}\right)^T \frac{\partial(\mathbf{G}\mathbf{G}^T)}{\partial t}\frac{\partial V}{\partial \bar{\mathbf{x}}} \tag{6.4.7}$$

Now, the partial derivative $\frac{\partial L}{\partial \bar{\mathbf{x}}}$ is a function of $\bar{\mathbf{x}}$ and the partial derivative $\frac{\partial V}{\partial \bar{\mathbf{x}}}$ is a function of $\bar{\mathbf{x}}$ and $\mathbf{w}$. The boundedness of $\bar{\mathbf{x}}$ and $\mathbf{w}$ has already been established . Thus, the partial derivatives $\frac{\partial L}{\partial \bar{\mathbf{x}}}$ and $\frac{\partial V}{\partial \bar{\mathbf{x}}}$ are bounded. From (6.3.11), we find that $\mathbf{G}$ is a vector of constants. Hence the partial derivative $\frac{\partial(\mathbf{G}\mathbf{G}^T)}{\partial t} = 0$. Thus, $\ddot{V}$ is bounded for all time and we can hence conclude that $\dot{V}$ is uniformly continuous in time. Based on this conclusion, the conditions imposed on $V(\bar{\mathbf{x}}, t)$ and (6.4.6), we can state based on Barbalat's Lemma that $\dot{V} \to 0$ as $t \to \infty$. From (6.4.3), $\dot{V} = 0$ implies that

$$-L - \frac{1}{4}\left(\frac{\partial V}{\partial \bar{\mathbf{x}}}\right)^T \mathbf{G}\mathbf{G}^T \frac{\partial V}{\partial \bar{\mathbf{x}}} = 0$$

Since both L and $\left(\frac{\partial V}{\partial \bar{\mathbf{x}}}\right)^T \mathbf{G}\mathbf{G}^T \frac{\partial V}{\partial \bar{\mathbf{x}}}$ are positive scalars, the above equation leads to the following result

$$L = 0 \quad \text{and} \quad \left(\frac{\partial V}{\partial \bar{\mathbf{x}}}\right)^T \mathbf{G}\mathbf{G}^T \frac{\partial V}{\partial \bar{\mathbf{x}}} = 0$$

Thus, we can conclude that $\bar{\mathbf{x}} \to 0$ and $\frac{\partial V}{\partial \bar{\mathbf{x}}} \to 0$ as $t \to \infty$. This establishes the fact that the approximate optimal value function (6.3.21) along with the weight update rule (6.3.24) guarantee asymptotic stability in the sense of Lyapunov.

6.5   Design Procedure

In this section, we summarize the main steps that need to be followed to design an Optimal Sliding Mode Controller for systems of the type (6.3.1) using the proposed algorithm.

1. Design the sliding surface s using the equation (6.3.3).

2. Based on knowledge of the system under consideration, choose the gain parameter M to satisfy the constraint $M >\max|\zeta|$. Choose the boundary layer width ϵ. It should be noted that a smaller value of ϵ leads to more robustness against disturbances at the cost of higher chattering.

3. Determine $\mathbf{F}(\bar{\mathbf{x}}), \mathbf{G}(\bar{\mathbf{x}})$ and $\bar{f}$ using the equations (6.3.11) and (6.3.13) respectively.

4. Choose a parametric positive semi-definite structure for the cost-to-go function $V(\bar{\mathbf{x}}, t) = h(\mathbf{w}, \bar{\mathbf{x}})$ such that it satisfies (6.4.4). A possible candidate for an n-th order system of the type (6.3.1) is $V = \frac{1}{2}\left(\sum_{i=1}^{n+1} w_i x_i\right)^2 + \frac{1}{2}\sum_{i=1}^{n+1} w_i{}^2$. Here $x_{n+1} = \phi$.

5. Using the parameterized cost-go-to function as defined in Step 4, compute the partial derivatives $\frac{\partial h}{\partial \mathbf{w}}$ and $\frac{\partial h}{\partial \bar{\mathbf{x}}}$.

6. Using the Pseudo-inverse method, find the minimum norm solution to the equation (6.3.24). This gives the weight update law for the parameterized function V.

7. Derive the optimal update law v^* for the parameter ϕ using the equation (6.3.16). This update law minimizes the performance index (6.3.2).

8. Construct the control law u using equation (6.3.8) and the optimal update law as obtained in step 7.

9. While implementing the control law, the initial value of ϕ should be chosen so as to satisfy the constraint $s(0) = 0$ i.e. $\phi(0) = -\sum_{i=1}^{n-1} c_i x_i(0) - x_n(0)$.

6.6   Simulation and Results

In this section, we consider two different non-linear dynamical systems and establish the efficacy of the proposed Optimal Sliding Mode control scheme.

Example 1: Let us consider the following first-order system

$$\dot{x} = -x^3 + u + \zeta \tag{6.6.1}$$

where ζ is the bounded exogenous disturbance. Let the performance index be

$$J = \int_0^\infty \left(\frac{1}{2} x^2 + u^2 \right) \, dt. \tag{6.6.2}$$

The task is to design a control action u which drives the state x to the origin in the presence of the disturbance and also minimizes the cost function given by (6.6.2). Thus, the problem is an optimal regulation problem and we consider three separate designs for the same.

Design 1 : *Optimal Sliding Mode Control*

Let the sliding surface s be chosen as

$$s = x + \phi \tag{6.6.3}$$

Comparing with the general formulation in (6.3.1) and (6.3.2) , we have $f(x) = -x^3$ and $L = \frac{1}{2} x^2$. Using (6.3.8),

$$u = x^3 - \dot{\phi} - \frac{M}{\epsilon} s \tag{6.6.4}$$

As has been established earlier, the choice of this control law along with the constraint that $\phi(0) = -x(0)$, ensures that system remains confined to the boundary layer from $t = 0$, even in the presence of the disturbance ζ. This establishes the robustness of the scheme. Next, we consider the nominal system (without the disturbance) and by denoting $x_1 = x, x_2 = \phi, v = \dot{\phi}$ and $\eta = \frac{M}{\epsilon}$, we reformulate the dynamics of (6.6.1) as

$$\begin{aligned} \dot{x}_1 &= -\eta(x_1 + x_2) - v \\ \dot{x}_2 &= v \end{aligned} \tag{6.6.5}$$

Thus, comparing with (6.3.10) and (6.3.11) , we have

$$\mathbf{F}(\bar{\mathbf{x}}) = \begin{bmatrix} -\eta(x_1 + x_2) \\ 0 \end{bmatrix} , \mathbf{G}(\bar{\mathbf{x}}) = \begin{bmatrix} -1 \\ 1 \end{bmatrix} \tag{6.6.6}$$

where $\bar{\mathbf{x}} = [x_1, x_2]^T$. Using (6.3.12), we have $\bar{f} = f + \eta(x_1 + x_2) = -x_1{}^3 + \eta(x_1 + x_2)$.
Let us choose the following structure for the optimal cost-to-go function

$$V = \frac{1}{2}(w_1 x_1 + w_2 x_2)^2 + \frac{1}{2}(w_1{}^2 + w_2{}^2) \tag{6.6.7}$$

The weight vector $\mathbf{w} = [w_1, w_2]^T$ is updated by using the pseudo-inverse solution to the under-determined equation (6.3.24), which is reproduced here for convenience

$$\left(\frac{\partial V}{\partial \mathbf{w}}\right)^T \dot{\mathbf{w}} = -L + \frac{1}{4}\left(\frac{\partial V}{\partial \bar{\mathbf{x}}}\right)^T \mathbf{G}\mathbf{G}^T \frac{\partial V}{\partial \bar{\mathbf{x}}} - \left(\frac{\partial V}{\partial \bar{\mathbf{x}}}\right)^T \mathbf{F} + \bar{f}\left(\frac{\partial V}{\partial \bar{\mathbf{x}}}\right)^T \mathbf{G} \tag{6.6.8}$$

where the partial derivatives are given by

$$\frac{\partial V}{\partial \mathbf{x}} = [(w_1 x_1 + w_2 x_2)w_1, (w_1 x_1 + w_2 x_2)w_2]^T, \qquad (6.6.9)$$

$$\frac{\partial V}{\partial \mathbf{w}} = [(w_1 x_1 + w_2 x_2)x_1 + w_1, (w_1 x_1 + w_2 x_2)x_2 + w_2]^T \qquad (6.6.10)$$

The optimal control v^* is given by (6.3.16), and for this problem it is computed to be

$$v^* = -\bar{f} - \frac{1}{2}\mathbf{G}^T(\bar{\mathbf{x}})\frac{\partial V}{\partial \bar{\mathbf{x}}} = -x_1{}^3 + \eta(x_1 + x_2) - \frac{1}{2}[w_1(w_2 - w_1)x_1 + w_2(w_2 - w_1)x_2] \quad (6.6.11)$$

Using (6.6.4) and (6.6.11), the optimal sliding mode control u for the system given by (6.6.1) is

$$u = \frac{1}{2}[w_1(w_2 - w_1)x_1 + w_2(w_2 - w_1)x_2] \qquad (6.6.12)$$

This control law along with the weight update law (6.6.8) completes the Optimal Sliding Mode Control design.

Design 2 : *Conventional Sliding Mode Control*

Since the system under consideration is a first-order system, let us define the sliding surface as $s = x$. Let a Lyapunov candidate be chosen as

$$V = \frac{1}{2}s^2 \qquad (6.6.13)$$

Taking the derivative of V with respect to time, we get

$$\dot{V} = s\dot{s} = s(-x^3 + u + \zeta) \qquad (6.6.14)$$

Let us define u as

$$u = x^3 - k sgn(s) \qquad (6.6.15)$$

where k is a positive constant such that $k > \max|\zeta|$ and $sgn(\cdot)$ represents the signum function. This gives

$$\dot{V} = s\dot{s} = s(-k sgn(s) + \zeta) = -k|s| + s\zeta \leq -|s|(k - \max|\zeta|) < 0 \qquad (6.6.16)$$

Thus, the control law u given by (6.6.15) guarantees asymptotic stability. To reduce the chattering phenomenon existing in conventional SMC, we use the popular boundary layer technique where the signum function is approximated by the saturation function $\frac{s}{(|s|+\epsilon)}$ and ϵ is a small positive quantity representing the width of the boundary layer. This yields the following smooth sliding mode control law

$$u = x^3 - k\frac{s}{(|s| + \epsilon)} \qquad (6.6.17)$$

Design 3 : *HJB based optimal control (analytical solution)*

Since the dynamics of the system given by (6.6.1) is time invariant, the HJB equation for this system (nominal) turns out to be

$$\min_{\mathbf{u}} \left(\frac{1}{2}x^2 + u^2 + \frac{\partial J^*}{\partial x}\dot{x} \right) = 0 \tag{6.6.18}$$

Or,

$$\min_{\mathbf{u}} \left(\frac{1}{2}x^2 + u^2 + \frac{\partial J^*}{\partial x}(-x^3 + u) \right) = 0 \tag{6.6.19}$$

This gives the following optimal control law u^*

$$u^* = -\frac{1}{2}\frac{\partial J^*}{\partial x} \tag{6.6.20}$$

Replacing u^* in (6.6.19) gives

$$-\frac{1}{4}(\nabla J)^2 - \nabla J x^3 + \frac{1}{2}x^2 = 0 \tag{6.6.21}$$

where $\nabla J = \frac{\partial J^*}{\partial x}$. This is a quadratic equation in ∇J. Noting that only a positive definite function is acceptable as the solution, we get

$$\nabla J = -2\left(x^3 - \sqrt{x^6 + \frac{1}{2}x^2} \right) \tag{6.6.22}$$

Thus, using (6.6.20) and (6.6.22), the optimal control law is

$$u^* = x^3 - \sqrt{x^6 + \frac{1}{2}x^2} \tag{6.6.23}$$

This represents the analytical optimal solution to the HJB equation for the system (6.6.1) and forms the benchmark for testing optimal performance.

To have a fair comparison between the three controls, the initial value of the state x is chosen the same for all three designs such that $x(0) = 0.1$. For the optimal sliding mode controller, $\phi(0) = -0.1, [w_1(0), w_2(0)] = [10, 12], M = 5, \epsilon = 0.1$. Hence $\eta = 50$. Also, in order to make the comparison between the optimal SMC and the conventional SMC more meaningful, for the conventional SMC, $k = 5$ and ϵ (boundary layer width)$= 0.1$.

In order to analyze quantitatively the performances of the three controls, we require cost functionals. Since it is not possible to integrate till infinite time, the cost functional is modified to integrate during a finite time period of 10 secs -

$$J_1 = \int_0^{10} \left(\frac{1}{2}x^2 + u^2 \right) \, \mathrm{d}t. \tag{6.6.24}$$

Moreover, in order to analyze the robustness of the three controls around the origin, we define another cost functional given by

$$J_2 = \frac{1}{2} \int_0^{10} x^2 \, \mathrm{d}t. \tag{6.6.25}$$

The values of the two cost functionals J_1 and J_2, for different disturbances, are tabulated in Table 6.1 and Table 6.2 respectively. From Tables 6.1 and 6.2, the following observations can be made:

- The cost functional J_1 is the least for the HJB based controller and maximum for the conventional SMC. The performance of the Optimal SMC is quite close to that of the HJB based optimal control, however the performance of the conventional SMC is much worse. Thus, we can conclude that the Optimal SMC is *"nearly optimal"*.

- For J_2, the average value for the Optimal SMC is almost **0.42** times that for the HJB based controller, implying it is far more robust. Although the conventional SMC is the most robust out of the three designs, it is the least optimal. The prime advantage of the proposed scheme is that it retains the robustness of the conventional SMC without compromising on optimality.

Next, a simulation is done for a different initial condition $x(0) = 0.01$, keeping all other parameters unchanged. Figure 6.1 shows the evolution of the state x for the three different control actions in the presence of the time-varying bounded disturbance $\zeta = 0.01 \sin(4\pi t)$. From the zoomed version of the state response, it can be observed that the conventional SMC drives the state towards the origin the fastest, followed by the Optimal SMC and the HJB based control action. It can be seen that after around 10 secs the state response for the HJB based control begins to diverge. Thus, the optimal control derived based on the HJB principle does not guarantee stability for time varying disturbances. Clearly, the proposed Optimal SMC is far more robust.

Figure 6.2 shows the three different control actions. Eventually the conventional SMC control action becomes exactly equal and opposite to $\zeta = 0.01 \sin(4\pi t)$, making it the most robust. Although the disturbance does not vanish , the HJB based control settles down to zero and hence it is the least robust. The Optimal SMC action does not vanish, and from its state response we can ascertain that it is fairly robust.

Example 2: Let us consider the following single link manipulator system

$$\begin{aligned} \dot{x_1} &= x_2 \\ \dot{x_2} &= -10 \sin x_1 + u + \zeta \end{aligned} \tag{6.6.26}$$

Table 6.1: J_1 for the three controls

Cases	SMC	Optimal SMC	HJB
$\zeta = 0$	41.7678	1.7364	0.7236
$\zeta = 0.01 \sin(4\pi t)$	41.8784	1.8497	0.9196
$\zeta = 0.01 \cos(4\pi t)$	41.9140	1.9202	0.9455
$\zeta = 0.1 \sin(4\pi t)$	49.0422	2.6011	1.5147
$\zeta = 0.1 \cos(4\pi t)$	47.4824	2.5052	1.4328
Average	44.4170	**2.1225**	1.10724

Table 6.2: J_2 for the three controls

Cases	SMC	Optimal SMC	HJB
$\zeta = 0$	0.0260	0.1929	0.3652
$\zeta = 0.01 \sin(4\pi t)$	0.0263	0.2074	0.4636
$\zeta = 0.01 \cos(4\pi t)$	0.0265	0.2138	0.4766
$\zeta = 0.1 \sin(4\pi t)$	0.0278	0.2910	0.7628
$\zeta = 0.1 \cos(4\pi t)$	0.0271	0.2666	0.7208
Average	0.0267	**0.2343**	0.5578

where ζ represents the disturbance term and the task is to design u so as to minimize the following cost function

$$J = \int_0^\infty \left(\frac{1}{2}(x_1{}^2 + x_2{}^2) + u^2 \right) \mathrm{d}t. \tag{6.6.27}$$

Design 1 : *Optimal Sliding Mode Control*

Let the sliding surface s be chosen as

$$s = c_1 x_1 + x_2 + \phi \tag{6.6.28}$$

Comparing with the general formulation in (6.3.1) and (6.3.2), we have $f(\mathbf{x}) = -10 \sin x_1$ and $L = \frac{1}{2}(x_1{}^2 + x_2{}^2)$. Let us choose the following structure for the optimal cost-to-go function

$$V = \frac{1}{2}(w_1 x_1 + w_2 x_2 + w_3 x_3)^2 + \frac{1}{2}(w_1{}^2 + w_2{}^2 + w_3{}^2) \tag{6.6.29}$$

We skip routine details and present the final control law -

$$u = \frac{1}{2}[w_1(w_3 - w_2)x_1 + w_2(w_3 - w_2)x_2 + w_3(w_3 - w_2)x_3] \tag{6.6.30}$$

Design 2 : *Conventional Sliding Mode Control*
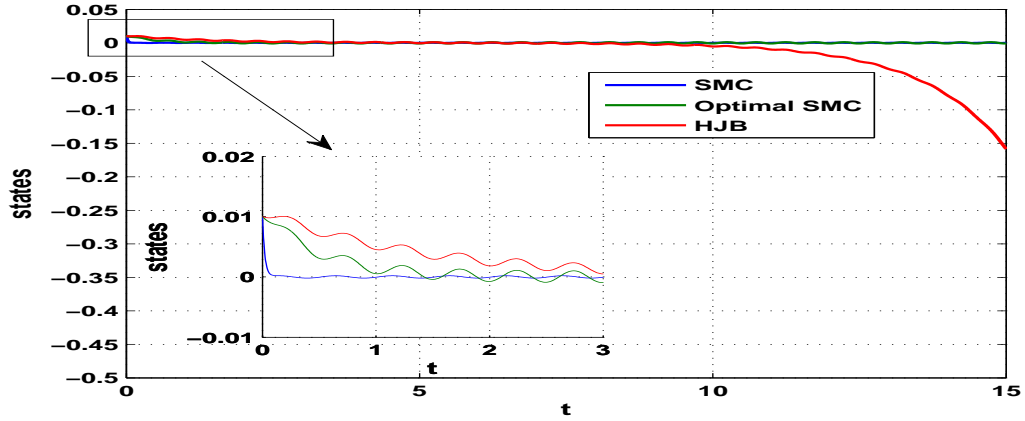
Figure 6.1: Evolution of states
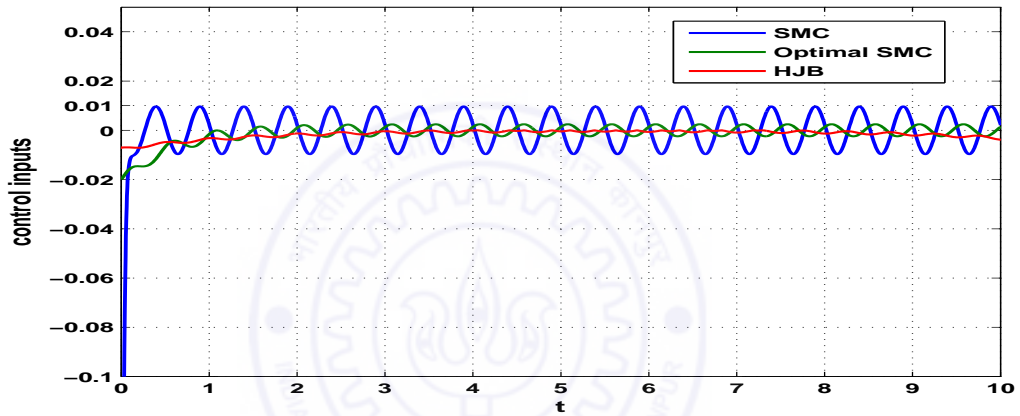
Figure 6.2: Control inputs

Let us define the sliding surface as

$$s = \dot{e} + \lambda e \qquad (6.6.31)$$

where $e = x_1$ (as it is a regulation problem). Let a Lyapunov candidate be chosen as $V = \frac{1}{2}s^2$. The design steps are the same as that for a conventional SMC scheme using the Boundary Layer Technique. We skip the details and present the final control law

$$u = 10\sin x_1 - \lambda x_2 - k\frac{s}{(|s| + \epsilon)} \qquad (6.6.32)$$

where k is a positive constant such that $k > \max|\zeta|$, $sgn(\cdot)$ represents the signum function and λ is a positive constant.

To have a fair comparison between the two controls, the same initial values $x_1(0) = 0.01$ and $x_2(0) = 0$ are chosen for both the designs. For the Optimal SMC, Theorem 1 necessitates that $s(0) = 0$, that is, $\phi(0) = -c_1 x_1(0) - x_2(0)$. Taking $c_1 = 10, \phi(0) = -0.1$. The initial weight vector is chosen as $[w_1(0), w_2(0), w_3(0)] = [20, 3, 5.75]$. The other parameters

are $M = 1, \epsilon = 0.01$. Hence $\eta = 100$. Also, in order to make the comparison between the optimal SMC and the conventional SMC more meaningful, for the conventional SMC, $k = 1, \epsilon$ (boundary layer width)$= 0.01$ and $\lambda = 10$. As in the previous example, we define two cost functionals J_1 and J_2 to analyze quantitatively the relative performances of the two designs. They are defined as

$$J_1 = \int_0^{10} \left(\frac{1}{2}(x_1{}^2 + x_2{}^2) + u^2 \right) \, \mathrm{d}t. \tag{6.6.33}$$

and

$$J_2 = \frac{1}{2} \int_0^{10} (x_1{}^2 + x_2{}^2) \, \mathrm{d}t. \tag{6.6.34}$$

The disturbance ζ is chosen as $\zeta = a \sin t + b \cos t$ where a, b are constants. From Table 6.3, it is evident that the proposed Optimal SMC has a much lower J_1 cost functional than that of the conventional SMC, implying that it is a more optimal SMC design. Although the conventional SMC is more robust than the proposed scheme (as is evident from the J_2 cost functional values) , it can be seen from Figures 6.3 and 6.4 that the Optimal SMC ensures fast convergence of the states to zero even in the presence of the time varying disturbance ζ. Figure 6.3 depicts the evolution of the position state x_1 and the velocity state x_2 for the two different control actions corresponding to the case when $a = 0.01, b = 0.02$. Figure 6.4 shows the control inputs for the two designs.
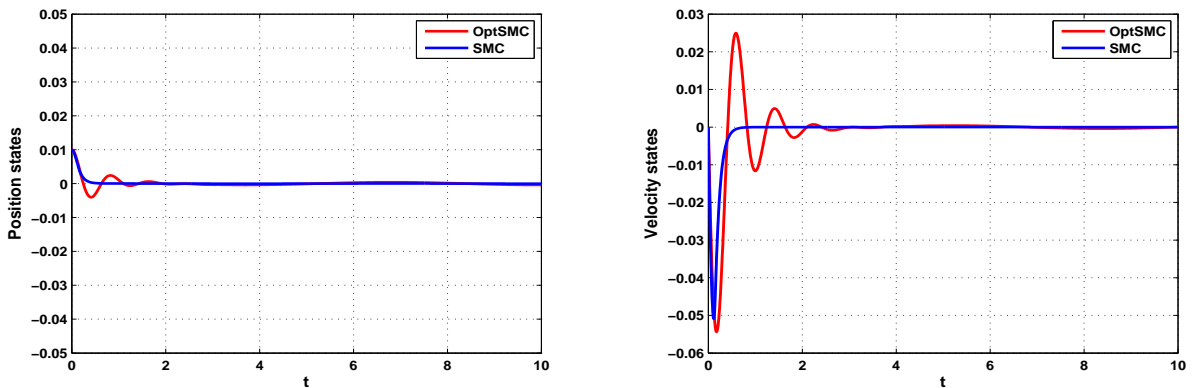
Figure 6.3: Position and Velocity Trajectories

Table 6.3: J_1 and J_2 for the two controls

Cases	SMC		Optimal SMC	
	J_1	J_2	J_1	J_2
a=0.01,b=0.02	13.0684	0.0274	7.6162	0.0571
a=0.02,b=0.01	13.0055	0.0280	7.6265	0.0598
a=0,b=0.01	12.8628	0.0281	7.5374	0.0603
a=0.01,b=0	12.6294	0.0246	7.3033	0.0595
a=0.02,b=0.02	13.2034	0.0273	7.7225	0.0569
Average	12.9539	0.0271	**7.5612**	**0.0587**
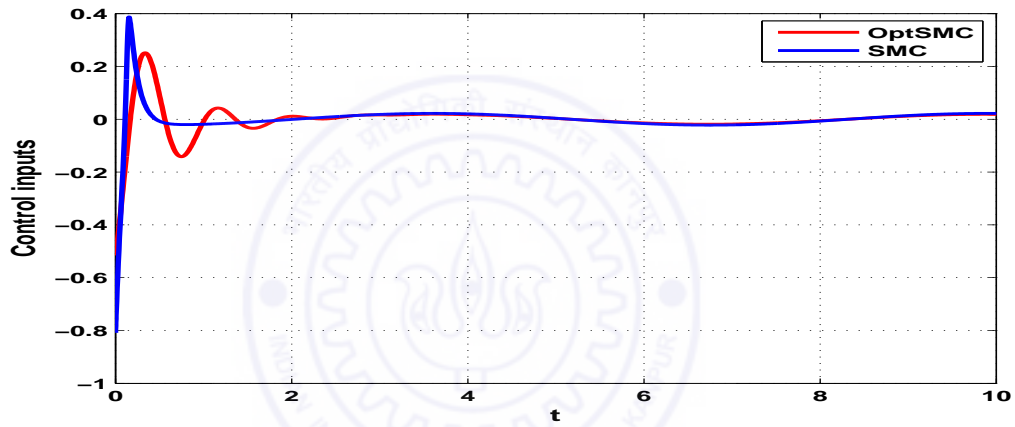
Figure 6.4: Control inputs

6.7 Extension to Trajectory Tracking Applications : A Case Study

6.7.1 Problem Formulation

Let us consider the following nonlinear system

$$\dot{\mathbf{x}} = \mathbf{p}(\mathbf{x}) + \mathbf{g}u, \tag{6.7.1}$$

where $\mathbf{x} \in \Re^n$, $\mathbf{p}(\mathbf{x}) \in \Re^n$, $\mathbf{g} \in \Re^n$ and u is a scalar. In accordance with the theory which has been developed in this chapter so far, it is assumed that $\mathbf{p}(\mathbf{x})$ has a structure given by $\mathbf{p}(\mathbf{x}) = [x_2, x_3, \cdots, x_n, f(\mathbf{x})]^T$; $f(\mathbf{x})$ is a smooth function, and $\mathbf{g} = [0, 0, \cdots, 1]^T$. The objective of the infinite time optimal tracking problem is the design of the optimal control law u^*, which ensures that the nonlinear system (6.7.1) tracks a desired trajectory $\mathbf{x_d}$ in

an optimal manner [21]. Let us define the desired trajectory to be

$$\dot{\mathbf{x}}_{\mathbf{d}} = \mathbf{p}(\mathbf{x}_{\mathbf{d}}) + \mathbf{g}u_d, \tag{6.7.2}$$

where u_d is the desired control input. In equation (6.7.2), $\dot{\mathbf{x}}_{\mathbf{d}}$ and $\mathbf{p}(\mathbf{x}_{\mathbf{d}})$ are known. Hence, u_d can obtained by rearranging (6.7.2). It is given by

$$u_d = \dot{x}_{nd} - f(\mathbf{x}_{\mathbf{d}}) \tag{6.7.3}$$

Next, the state tracking error is defined as

$$\mathbf{e} = \mathbf{x} - \mathbf{x}_{\mathbf{d}} \tag{6.7.4}$$

Using (6.7.1), (6.7.2) and (6.7.4), the tracking error dynamics is given by

$$\dot{\mathbf{e}} = \mathbf{p}_{\mathbf{e}}(\mathbf{e}) + \mathbf{g}u_{\mathbf{e}}, \tag{6.7.5}$$

where $\mathbf{p}_{\mathbf{e}}(\mathbf{e}) = \mathbf{p}(\mathbf{x}) - \mathbf{p}(\mathbf{x}_{\mathbf{d}})$, and $u_{\mathbf{e}} = u - u_d$. In order to control (6.7.5) in an optimal manner, it is required to design $u_{\mathbf{e}}$ in a way which minimizes the following infinite horizon cost function

$$J_{\mathbf{e}} = \int_0^\infty [L(\mathbf{e}) + u_{\mathbf{e}}^2] \, \mathrm{d}t. \tag{6.7.6}$$

where $L(\mathbf{e}) \geq 0$ is a positive semi-definite function of the error state $\mathbf{e}$.

6.7.2   Solution Methodology

We have successfully formulated the problem in accordance with the theory which has been developed previously in this chapter. Now, we need to consider the applicability of this theory to the model of the MRI based micro-robot guidance system. To this end, we consider a simplified model of this system , proposed by Ferreira *et al.* in [7]. Some of the main simplifying assumptions which the authors make in [7] are

- The micro-robot under consideration is assumed to be large enough to neglect the effect of wall interaction forces such as Van der Waals force and Electrostatic force. As the electrostatic force is neglected in this model, the need to estimate the dielectric density of blood on-line is no longer necessary.

- The flow is assumed to be Newtonian i.e. variations of blood viscosity with vessel diameter is not taken into account.

Based on these assumptions, the only forces acting on the micro-robot are the drag force, the apparent weight and the force due to the magnetic field of the MRI. The blood vessel,

which is considered to be a tube which bifurcates in two with an angle θ, is shown in Figure 6.5. Let x_1 and x_2 represent the position and velocity of the micro-robot along the horizontal axis (x-axis), and let x_3 and x_4 denote its position and velocity along the vertical axis (z-axis). The state space representation of the system is as follows

$$
\begin{aligned}
&(S1)\begin{cases} \dot{x}_1 = x_2 \\ \dot{x}_2 = f_2(x_2) + \bar{u}_1 \end{cases} \\
&(S2)\begin{cases} \dot{x}_3 = x_4 \\ \dot{x}_4 = f_4(x_4) + \bar{u}_2 \end{cases}
\end{aligned} \tag{6.7.7}
$$

Here,

$$
\bar{u}_1 = a_2 v_x^2 - a_1 v_x + a_4 u_1 \tag{6.7.8}
$$

and

$$
\bar{u}_2 = b_2 v_z^2 - b_1 v_z - g\left(\frac{\rho}{\rho_r} - 1\right) + b_4 u_2 \tag{6.7.9}
$$

u_1 and u_2 are the actual control inputs. They are the magnetic field gradients generated by the MRI, and are given by $u_1 = ||\nabla B_x||$, $u_2 = ||\nabla B_z||$. v_x and v_z are the horizontal and vertical components respectively, of the blood's velocity. For a detailed description of the other terms involved in the state space description (6.7.7), one is referred to [7].

The steps to solve the optimal tracking problem are mentioned below

- Firstly, from (6.7.7), one can observe that the system can be split into two sub-systems $S(1)$ and $S(2)$. Independent control laws can be designed for each of these subsystems. Moreover, the structure of the two subsystems matches exactly with the class of nonlinear systems considered in our study. Thus, the first step is to reformulate the state space equations in the format of (6.7.5). This gives $\bar{u}_{\mathbf{e1}}$ and $\bar{u}_{\mathbf{e2}}$, where $\bar{u}_{\mathbf{e1}} = \bar{u}_1 - \bar{u}_{d1}$ and $\bar{u}_{\mathbf{e2}} = \bar{u}_2 - \bar{u}_{d2}$.

- Obtain $\bar{u}_{d1}$ and $\bar{u}_{d2}$ from

$$
\bar{u}_{d1} = \dot{x}_{2d} - f_2(x_{2d}) \quad ; \quad \bar{u}_{d2} = \dot{x}_{4d} - f_4(x_{4d}) \tag{6.7.10}
$$

- Based on definitions of $J_{\mathbf{e1}}$ and $J_{\mathbf{e2}}$, and the design procedure outlined in this chapter, one can obtain $\bar{u}_{\mathbf{e1}}$ and $\bar{u}_{\mathbf{e2}}$.

- Once $\bar{u}_{\mathbf{e1}}$ and $\bar{u}_{\mathbf{e2}}$ are known, $\bar{u}_1$ and $\bar{u}_2$ can be obtained easily.

- Using equations (6.7.8) and (6.7.9), the actual control inputs u_1 and u_2 can be obtained. This completes the design procedure.
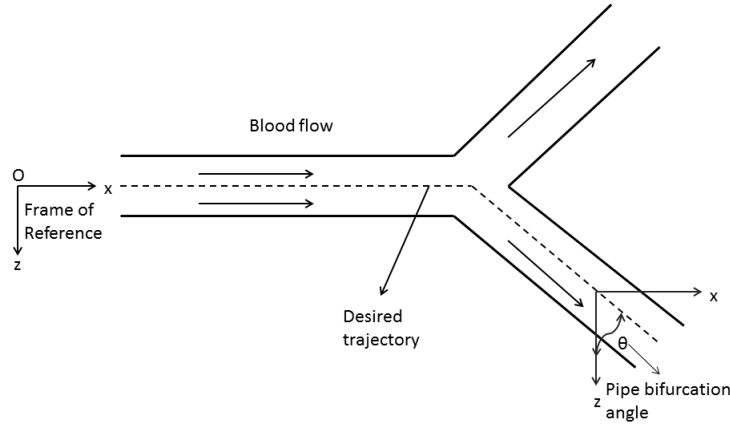
Figure 6.5: A blood vessel with bifurcation

6.7.3   Simulation study

Let the cost functions be defined as

$$J_{\mathbf{e1}} = \int_0^\infty \left(\frac{1}{2}\mathbf{e_1}^T \mathbf{e_1} + \bar{u}_{\mathbf{e1}}^2 \right) \, \mathrm{d}t \tag{6.7.11}$$

and

$$J_{\mathbf{e2}} = \int_0^\infty \left(\frac{1}{2}\mathbf{e_2}^T \mathbf{e_2} + \bar{u}_{\mathbf{e2}}^2 \right) \, \mathrm{d}t \tag{6.7.12}$$

Here $\mathbf{e_1} = [x_1 - x_{1d}(t), x_2 - \dot{x}_{1d}(t)]^T$ and $\mathbf{e_2} = [x_3 - x_{3d}(t), x_4 - \dot{x}_{3d}(t)]^T$. We use the exact reference trajectories which have been used for simulation in [7]. We have $x_{1d} = 0.01\sin(\frac{5.5t}{2})$ and $x_{3d} = 0.01\cos(\frac{5.5t}{2})$. To simplify the analysis, we assume the existence of an accurate observer which provides correct estimates of the velocity of the particle along the horizontal and vertical directions. The velocity of blood is given by

$$v = 0.035\left(1 + 1.15\sin(2\pi t)\right) \tag{6.7.13}$$

The simulation data is provided in Table 6.4.

It should be noted that M_1 and M_2 are the gains associated with the signum function. c_1 and c_2 are the sliding surface constants, and have been defined in accordance with the notation developed in this chapter. The sliding surfaces for the two subsystems are defined below

$$s_1 = e_{12} + c_1 e_{11} + \phi_1 \tag{6.7.14}$$

and

$$s_2 = e_{22} + c_2 e_{21} + \phi_2 \tag{6.7.15}$$

Table 6.4: Simulation Data

Radius of the core	r	$300\mu m$
Blood's viscosity	η	$15 \times 10^{-3} Pa.s$
Blood's density	ρ	$1060 kg.m^{-3}$
Robot's density	ρ_{sphere}	$8000 kg.m^{-3}$
Magnetization	M	$1.950 \times 10^6 A.m^{-1}$
Pipe bifurcation angle	θ	$\frac{\pi}{2}$
Controller gains	(M_1, M_2)	$(5, 5)$
Sliding surface gains	(c_1, c_2)	$(20, 20)$
Boundary layer widths	(ϵ_1, ϵ_2)	$(0.1, 0.1)$

Here, $e_{11} = \mathbf{e}_1(1)$, $e_{12} = \mathbf{e}_1(2)$, $e_{21} = \mathbf{e}_2(1)$, and $e_{22} = \mathbf{e}_2(2)$. The initial conditions of the states are $(x_{10}, x_{20}) = (0.01, 0.0025)$ and $(x_{30}, x_{40}) = (0.02, 0.01)$. The initial conditions of ϕ_1 and ϕ_2 can be obtained easily from the idea that $s_1(0) = 0$ and $s_2(0) = 0$.

The cost function for each subsystem will be approximated by Lyapunov functions. These Lyapunov functions are defined as

$$V_1 = \frac{1}{2}(w_1 e_{11} + w_2 e_{12} + w_3 \phi_1)^2 + \frac{1}{2}(w_1{}^2 + w_2{}^2 + w_3{}^2) \tag{6.7.16}$$

$$V_2 = \frac{1}{2}(w_4 e_{12} + w_5 e_{22} + w_6 \phi_2)^2 + \frac{1}{2}(w_4{}^2 + w_5{}^2 + w_6{}^2) \tag{6.7.17}$$

The initial conditions of the weights in the Lyapunov functions are $(w1, w2, w3) = (2, 5, 7)$ and $(w4, w5, w6) = (4, 5, 10)$.

6.7.4 Discussion of Results

- Table 6.5 shows the details of the simulation study. We find that the position states converge to their desired reference trajectories. This is apparent from the trajectory plots and the plots of the sliding surfaces.

- The control inputs are smooth and have magnitudes less than $80mT/m$. Thus, the practical bounds on the MRI gradients are not exceeded.

- It is seen that the control actions $\bar{u}_{\mathbf{e1}}$ and $\bar{u}_{\mathbf{e2}}$ converge to zero. This is expected at steady state when the error states converge to zero. Also, this ensures that when the transients decay, $\bar{u}_1$ becomes $\bar{u}_{d1}$ and $\bar{u}_2$ becomes $\bar{u}_{d2}$, i.e. the control inputs attain their desired values.
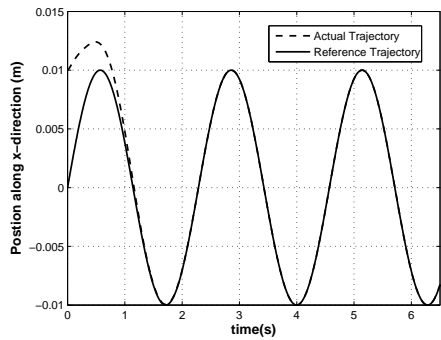
Position trajectories along x-axis
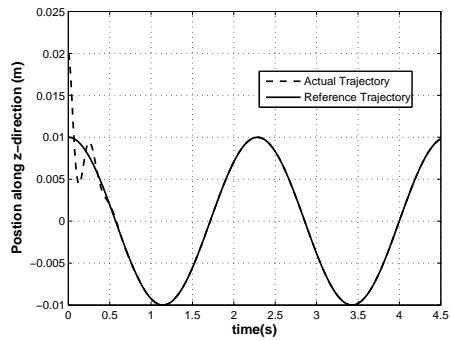
Position trajectories along z-axis
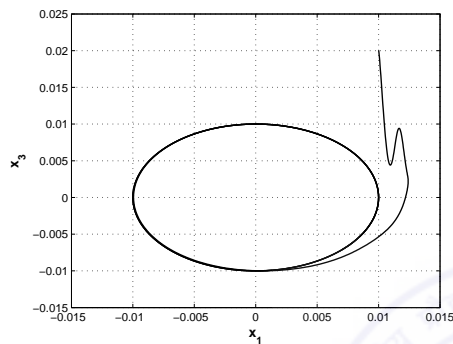
The X-Z trajectory

The Sliding Surfaces

Control input along x-direction

Control input along z-direction

Plot of $\bar{u}_{\mathbf{e1}}$
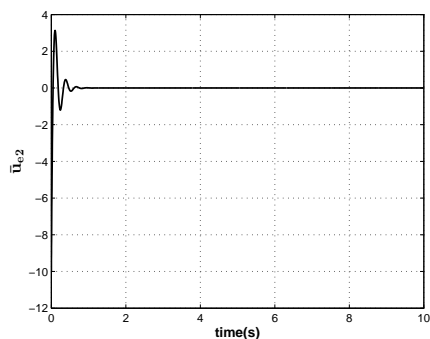
Plot of $\bar{u}_{\mathbf{e2}}$

Table 6.5: Details of the Simulation Study

Remarks-

- The simulation study which has been conducted, illustrates how a tracking problem can be solved in an optimal manner, using the algorithm developed in this chapter.

- Although the theory has been developed for a particular class of nonlinear systems, considering only a single input, the basic ideas can be extended to MIMO nonlinear systems as well.
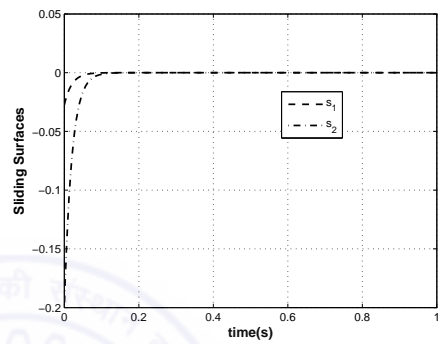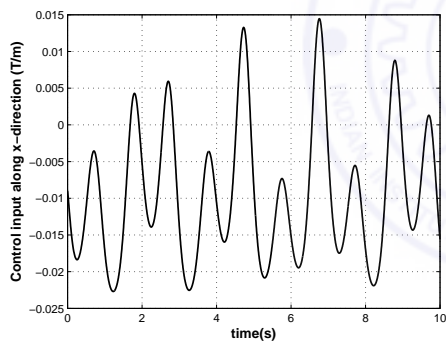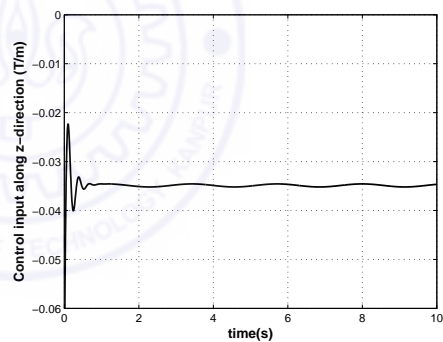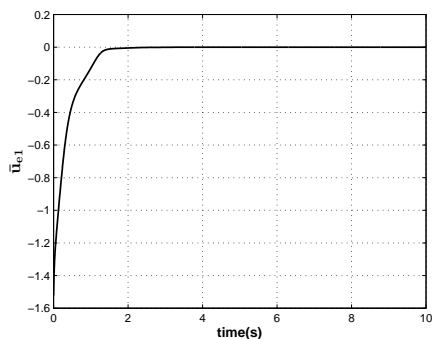
- The developed theory can be used for robotic manipulators as well. For a n-link rigid robotic manipulator, the entire system can be decomposed into n subsystems, and the theory presented can be applied to design control laws for each subsystem.

6.8   Summary

In this chapter, a novel approach for the development of an Optimal SMC has been presented using a Single Network Adaptive Critic for approximating the solution to the HJB equation. Unlike earlier approaches, the parameter ϕ of the time-varying sliding surface, which adds the extra degree of freedom, is updated online. A detailed stability analysis of the entire scheme has been performed. A systematic design procedure for implementing the proposed algorithm has been presented. The performance of the proposed control design has been studied through simulation results on first order and second order nonlinear control affine systems. It has been observed that not only is the proposed scheme far more optimal than the conventional SMC, it also guarantees asymptotic stability in the sense of Lyapunov for systems with bounded time-varying disturbances. The developed technique has then been tested for a trajectory tracking application on the MRI based micro-robot guidance system. Thus, the design motivation of merging the robustness of conventional SMC with optimal control theory has been successfully achieved with the proposed scheme.

Chapter 7

Conclusions and Future Work

7.1 Conclusion

In this thesis, we studied the feasibility of applying Sliding Mode Control (SMC) to two applications - MRI based targeted drug delivery using a ferromagnetic micro-robot, and control of a 4 DOF Barrett Whole Arm Manipulator. We started off by designing an Adaptive Fuzzy Sliding Mode Control scheme (AFSMC) for steering a micro-robot along the center-line of a human blood vessel. We used a highly nonlinear model existing in literature for the same. The design procedure and stability analysis of the proposed scheme was presented. Simulations were performed to compare our design with a state-of-the-art backstepping approach. The proposed scheme was able to achieve perfect tracking and could estimate the dielectric density of blood on-line. Moreover, the control law was smooth and did not exceed the practical bounds set for this application.

Next, we developed a rigid body model of the Barrett WAM (4 DOF) using the Newton-Euler technique. This was the first step towards its control. The model was validated through tracking experiments performed on all 4 joints, using two control strategies - Backstepping and Sliding Mode Control. Comparisons were drawn between the two techniques based on the Root Mean Square Error and Mean control effort. Conventional SMC only guarantees asymptotic stability. This motivated us to develop a Nonsingular Fast Terminal Sliding Mode Control (NFTSMC) scheme which could ensure finite time convergence of the error trajectories to zero. We presented the detailed proof of time convergence. Simulations on simple 1st and 2nd order systems were used to illustrate the main ideas. The concept was extended to the trajectory tracking problem of the WAM. A comparative study was performed between simulations and experiments conducted on the WAM, to understand the differences existing between the two environments.

Finally, we explored the concept of optimal sliding mode control. This was an effort towards fusing the inherent robustness feature of SMC with optimal control. To this end, a dynamic sliding surface was defined. The time varying parameter of the sliding surface lent the extra degree of freedom necessary to make the design optimal. This parameter was updated on-line, in an optimal manner, using the continuous time version of the Single Network Adaptive Critic (SNAC) architecture. The main design steps were outlined. Analysis of stability was presented. Comparisons were drawn with HJB based control and SMC. It was found that the developed technique was more robust as compared to a HJB based design, but less robust as compared to a conventional SMC. However, it was a more optimal design as compared to SMC, but less optimal as compared to a HJB based controller. Thus, in a sense, the proposed design can be thought of as a more optimal version of the conventional SMC which incurs less control effort. To illustrate how the optimal sliding mode control technique can be extended to a tracking problem, we considered a simplified model of the MRI based micro-robot guidance system. Simulation results were presented for this case study.

Some directions of future research are as follows

7.1.1 Future Work on the MRI-Drug Delivery System

- In our work, we assumed that a perfect imaging system already exists which provides noise-free position feedback information. Thus, the development of accurate and fast image processing algorithms is key to real time implementation of this concept. This is an area which needs a lot of exploration.

- Building a simulation environment which mimics the MRI system is necessary. This simulator should be able to replicate the closed loop feedback mechanism by making the image processing module and the control module work in tandem with minimum latency.

- A thermal modeling of the MRI cooling system can be used to frame an optimization problem which seeks to maximize the MRI gradients and the duty cycles of operation, subject to imposed conditions on the temperature limits of the cooling system. This is a very relevant problem which has not be attempted in literature.

- Variants of SMC and other robust control techniques can be developed for this model, and a comparative study among them can give a fair idea regarding the most feasible approach.

- In our study, we have not considered the design of observers. This is another area that merits further research.
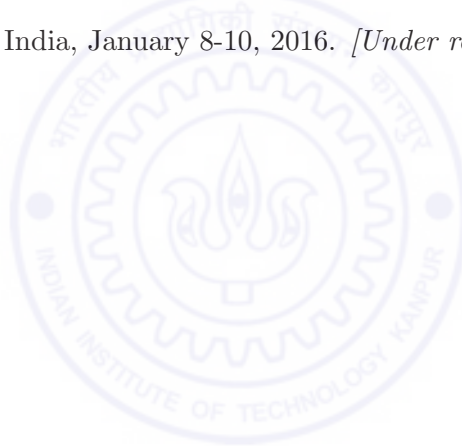
7.1.2 Future Work on Control of the WAM robot

- Firstly, the rigid body model which has been developed can be further refined. This can be achieved by either using statistical regression techniques or by using nonlinear disturbance observers based on Lyapunov theory.

- A hybrid model, based mainly on rigid body modeling and refined by using state-of-the-art online regression techniques (such as Locally Weighted Projection Regression [73]), when used in tandem with the robust SMC techniques developed in this thesis, can lead to further accuracy in tracking performance.

- Since the main goal of this work is Imitation Learning, the developed control module can be tested in real time with the Dynamic motion generator module. This would draw more attractiveness towards our work and make it more complete.

- During our experiments, we have encountered mechanical vibrations of the WAM owing to the chattering phenomenon. For simplicity, we have used the Boundary layer approach in our experiments. The Adaptive Fuzzy algorithm discussed in this thesis can be extended to the WAM model. Also, Higher Order Sliding Mode Control has been known to completely remove the chattering phenomenon [43]. These chattering removal techniques can be tested to obtain more smooth control laws.

- The Optimal sliding mode control design can be extended to the WAM model. This can be an interesting area of research.

- An important point to note is that although all the control development takes place in continuous time domain, implementations in real time always lead to discretization of these control laws. Often, numerical instability results as a consequence. To avoid this, Discrete sliding mode control (DSMC) designs can be taken up. DSMC, infact, represents the future in the area of practical implementations of SMC.

List of Publications

1. Aritra Mitra and Laxmidhar Behera, "*Development of a Fuzzy Sliding Mode Controller with Adaptive Tuning Technique for a MRI guided robot in the human vasculature*", 2015 IEEE International Conference on Industrial Informatics (INDIN 2015), Cambridge, UK, July 22-24, 2015. *[Accepted for presentation]*

2. Aritra Mitra and Laxmidhar Behera, "*Continuous-Time Single Network Adaptive Critic Based Optimal Sliding Mode Control for Nonlinear Control Affine Systems*", 2015 Chinese Control Conference (CCC 2015), Hangzhou, China, July 28-30, 2015. *[Accepted for presentation]*

3. Aritra Mitra, Niladri Das, Raj Nayan Samant and Laxmidhar Behera, "*Control of a 4 DoF Barrett WAM Robot - Modeling, Control Synthesis and Experimental Validation*", 2016 IEEE International Conference on Control, Measurement and Instrumentation, India, January 8-10, 2016. *[Under review]*

Bibliography

[1] Code repository. https://github.com/raj111samant/Model-based-control-of-4-DOF-Barrett-Wam.

[2] Maple code for deriving model of the 4 dof barrett wam. https://drive.google.com/file/d/0B1SCfVjLdPjZekFMLXJpUnRJTzg/view?usp=sharing.

[3] Video of control experiments performed on the wam. https://www.youtube.com/watch?v=AhPH4fLEGpI.

[4] Jake J Abbott, Olgaç Ergeneman, Michael P Kummer, Ann M Hirt, and Bradley J Nelson. Modeling magnetic torque and force for controlled manipulation of soft-magnetic bodies. *Robotics, IEEE Transactions on*, 23(6):1247–1252, 2007.

[5] Jake J Abbott, Marco Cosentino Lagomarsino, Li Zhang, Lixin Dong, and Bradley J Nelson. How should microrobots swim? *The international journal of Robotics Research*, 2009.

[6] L. Arcese, A. Cherry, M. Fruchard, and A. Ferreira. Dynamic behavior investigation for trajectory control of a microrobot in blood vessels. In *Intelligent Robots and Systems (IROS), 2010 IEEE/RSJ International Conference on*, pages 5774–5779, Oct 2010.

[7] L. Arcese, M. Fruchard, and A. Ferreira. Nonlinear modeling and robust controller-observer for a magnetic microrobot in a fluidic environment using mri gradients. In *Intelligent Robots and Systems, 2009. IROS 2009. IEEE/RSJ International Conference on*, pages 534–539, Oct 2009.

[8] Laurent Arcese, Ali Cherry, Matthieu Fruchard, and Antoine Ferreira. High gain observer for backstepping control of a mri-guided therapeutic microrobot in blood vessels. In *Biomedical Robotics and Biomechatronics (BioRob), 2010 3rd IEEE RAS and EMBS International Conference on*, pages 349–354. IEEE, 2010.

[9] Laurent Arcese, Matthieu Fruchard, Felix Beyeler, Antoine Ferreira, and Bradley J Nelson. Adaptive backstepping and mems force sensor for an mri-guided microrobot in the vasculature. In *Robotics and Automation (ICRA), 2011 IEEE International Conference on*, pages 4121–4126. IEEE, 2011.

[10] Laurent Arcese, Matthieu Fruchard, and Antoine Ferreira. Endovascular magnetically guided robots: navigation modeling and optimization. *Biomedical Engineering, IEEE Transactions on*, 59(4):977–987, 2012.

[11] Haruhiko Asada and J-JE Slotine. *Robot analysis and control*. John Wiley & Sons, 1986.

[12] Karl J Åström and Björn Wittenmark. *Adaptive control*. Courier Corporation, 2013.

[13] Raj Bawa. Nanoparticle-based therapeutics in humans: a survey. *Nanotech. L. & Bus.*, 5:135, 2008.

[14] Karim Belharet, David Folio, and Antoine Ferreira. 3d mri-based predictive control of a ferromagnetic microrobot navigating in blood vessels. In *Biomedical Robotics and Biomechatronics (BioRob), 2010 3rd IEEE RAS and EMBS International Conference on*, pages 808–813. IEEE, 2010.

[15] AE Bryson. Yc ho applied optimal control. *New York: Blaisdell*, 1969.

[16] JA Burton and Alan SI Zinober. Continuous approximation of variable structure control. *International journal of systems science*, 17(6):875–885, 1986.

[17] Ik Hyeon Choi and Cheol Ho Lim. Low-velocity impact analysis of composite laminates using linearized contact law. *Composite structures*, 66(1):125–132, 2004.

[18] John J Craig. *Introduction to robotics: mechanics and control*, volume 3. Pearson Prentice Hall Upper Saddle River, 2005.

[19] Alex G Cuenca, Huabei Jiang, Steven N Hochwald, Matthew Delano, William G Cance, and Stephen R Grobmyer. Emerging implications of nanotechnology on cancer diagnostics and therapeutics. *Cancer*, 107(3):459–466, 2006.

[20] Christian Dahmen, David Folio, Tim Wortmann, Alexander Kluge, Antoine Ferreira, and Sergej Fatikow. Evaluation of a mri based propulsion/control system aiming at targeted micro/nano-capsule therapeutics. In *Intelligent Robots and Systems (IROS), 2012 IEEE/RSJ International Conference on*, pages 2565–2570. IEEE, 2012.

[21] T Dierks and Sarangapani Jagannathan. Optimal control of affine nonlinear continuous-time systems. In *American Control Conference (ACC), 2010*, pages 1568–1573. IEEE, 2010.

[22] Rui Dong, Hong-Wei Gao, and Quan-Xiang Pan. Optimal sliding mode control for nonlinear systems with uncertainties. In *Control and Decision Conference (CCDC), 2011 Chinese*, pages 2098–2103, May 2011.

[23] R Featherstone. Robot dynamics algorithms kluwer academic publishers. *Boston, MA*, 1987.

[24] Yong Feng, Xinghuo Yu, and Zhihong Man. Non-singular terminal sliding mode control of rigid manipulators. *Automatica*, 38(12):2159–2167, 2002.

[25] Michael Basin Alejandra Ferreira Leonid Fridman. Lqg-robust sliding mode control for linear stochastic systems with uncertainties. 2006.

[26] Katsuhisa Furuta. Sliding mode control of a discrete system. *Systems & Control Letters*, 14(2):145–152, 1990.

[27] Weibing Gao and James C Hung. Variable structure control of nonlinear systems: a new approach. *Industrial Electronics, IEEE Transactions on*, 40(1):45–55, 1993.

[28] GT Gillies, RC Ritter, WC Broaddus, MS Grady, MA Howard III, and RG McNeil. Magnetic manipulation instrumentation for medical physics research. *Review of Scientific Instruments*, 65(3):533–562, 1994.

[29] Andrew D Grief and Giles Richardson. Mathematical modelling of magnetically targeted drug delivery. *Journal of Magnetism and Magnetic Materials*, 293(1):455–463, 2005.

[30] Philip Hartman. Ordinary differential equations. *Classics in Applied Mathematics*, 38, 1964.

[31] Ibrahim Haskara. On sliding mode observers via equivalent control approach. *International Journal of control*, 71(6):1051–1067, 1998.

[32] DA Hays. Electrostatic adhesion of nonuniformly charged dielectric spheres. In *Institute of Physics Conference Series*, number 118, pages 223–228. IOP PUBLISHING LTD TEMPLE CIRCUS, TEMPLE WAY, BRISTOL BS1 6BE, ENGLAND, 1991.

[33] Dan A Hays. Role of electrostatics in adhesion. In *Fundamentals of Adhesion*, pages 249–278. Springer, 1991.

[34] Herman Høifødt. Dynamic modeling and simulation of robot manipulators: the newton-euler formulation. 2011.

[35] Yueming Hu, Shuzhi Sam Ge, and Chun-Yi Su. Stabilization of uncertain non-holonomic systems via time-varying sliding mode control. *Automatic Control, IEEE Transactions on*, 49(5):757–763, 2004.

[36] John Y Hung, Weibing Gao, and James C Hung. Variable structure control: a survey. *Industrial Electronics, IEEE Transactions on*, 40(1):2–22, 1993.

[37] Kenji Iimura, Satoshi Watanabe, Michitaka Suzuki, Mitsuaki Hirota, and Ko Higashitani. Simulation of entrainment of agglomerates from plate surfaces by shear flows. *Chemical Engineering Science*, 64(7):1455–1461, 2009.

[38] Ralf Kehlenbeck and Renzo Di Felice. Empirical relationships for the terminal settling velocity of spheres in cylindrical columns. *Chemical engineering & technology*, 22(4):303–308, 1999.

[39] Jeffrey D Kingsley, Huanyu Dou, Justin Morehead, Barrett Rabinow, Howard E Gendelman, and Christopher J Destache. Nanotechnology: a focus on nanoparticles as a drug delivery system. *Journal of Neuroimmune Pharmacology*, 1(3):340–350, 2006.

[40] A Jafari Koshkouei and ASI Zinober. Robust frequency shaping sliding mode control. *IEE Proceedings-Control Theory and Applications*, 147(3):312–320, 2000.

[41] Miroslav Krstic, Petar V Kokotovic, and Ioannis Kanellakopoulos. *Nonlinear and adaptive control design*. John Wiley & Sons, Inc., 1995.

[42] Swagat Kumar, Radhakant Padhi, and Laxmidhar Behera. Continuous-time single network adaptive critic for regulator design of nonlinear control affine systems. In *Proceedings of 17th World Congress of the International Federation of Automatic Control*, 2008.

[43] A Levant. Higher order sliding modes and arbitrary-order exact robust differentiation. In *Proceedings of the European Control Conference*, pages 996–1001. Citeseer, 2001.

[44] Xiaoqiu Li and Stephen Yurkovich. Sliding mode control of delayed systems with application to engine idle speed control. *Control Systems Technology, IEEE Transactions on*, 9(6):802–810, 2001.

[45] F-J Lin and S-L Chiu. Adaptive fuzzy sliding-mode control for pm synchronous servo motor drives. In *Control Theory and Applications, IEE Proceedings-*, volume 145, pages 63–72. IET, 1998.

[46] Sylvain Martel, Jean-Baptiste Mathieu, Ouajdi Felfoul, Arnaud Chanu, Eric Aboussouan, Samer Tamaz, Pierre Pouponneau, LHocine Yahia, Gilles Beaudoin, Gilles Soulez, et al. Automatic navigation of an untethered device in the artery of a living animal using a conventional clinical magnetic resonance imaging system. *Applied physics letters*, 90(11):114105, 2007.

[47] Jean-Baptiste Mathieu, Gilles Beaudoin, and Sylvain Martel. Method of propulsion of a ferromagnetic core in the cardiovascular system through magnetic gradients generated by an mri system. *Biomedical Engineering, IEEE Transactions on*, 53(2):292–299, 2006.

[48] Jean-Baptiste Mathieu and Sylvain Martel. In vivo validation of a propulsion method for untethered medical microrobots using a clinical magnetic resonance imaging system. In *Intelligent Robots and Systems, 2007. IROS 2007. IEEE/RSJ International Conference on*, pages 502–508. IEEE, 2007.

[49] Constantinos Mavroidis and Antoine Ferreira. *Nanorobotics: Current Approaches and Techniques.* Springer Science & Business Media, 2013.

[50] Cedomir Milosavljevic. General conditions for the existence of a quasi-sliding mode on the switching hyperplane in discrete variable structure systems. *Automation and Remote Control*, 46(3):307–314, 1985.

[51] Russel G Morgan and Ümit Özgüner. A decentralized variable structure control algorithm for robotic manipulators. *Robotics and Automation, IEEE Journal of*, 1(1):57–65, 1985.

[52] Rainer H Muller and Cornelia M Keck. Challenges and solutions for the delivery of biotech drugs–a review of drug nanocrystal technology and lipid nanoparticles. *Journal of biotechnology*, 113(1):151–170, 2004.

[53] D Subbaram Naidu. *Optimal control systems.* CRC press, 2002.

[54] Reshma R Nair, Laxmidhar Behera, Vipin Kumar, and Mo Jamshidi. Multisatellite formation control for remote sensing applications using artificial potential field and adaptive fuzzy sliding mode control. 2015.

[55] Duy Nguyen-Tuong, Jan R Peters, and Matthias Seeger. Local gaussian process regression for real time online model learning. In *Advances in Neural Information Processing Systems*, pages 1193–1200, 2009.

[56] Duy Nguyen-Tuong, Matthias Seeger, and Jan Peters. Computed torque control with nonparametric regression models. In *American Control Conference, 2008*, pages 212–217. IEEE, 2008.

[57] Gorka Orive, Rosa María Hernández, Alicia R Gascón, and José Luis Pedraz. Micro and nano drug delivery systems in cancer therapy. *Cancer Therapy*, 3(1):131–8, 2005.

[58] Yuri V Orlov. Discontinuous unit feedback control of uncertain infinite-dimensional systems. *Automatic Control, IEEE Transactions on*, 45(5):834–843, 2000.

[59] Radhakant Padhi, Nishant Unnikrishnan, Xiaohua Wang, and SN Balakrishnan. A single network adaptive critic (snac) architecture for optimal control synthesis for a class of nonlinear systems. *Neural Networks*, 19(10):1648–1660, 2006.

[60] Haiping Pang and Luping Wang. Global robust optimal sliding mode control for a class of affine nonlinear systems with uncertainties based on sdre. In *Computer Science and Engineering, 2009. WCSE '09. Second International Workshop on*, volume 2, pages 276–280, Oct 2009.

[61] Wilfrid Perruquetti and Jean-Pierre Barbot. *Sliding mode control in engineering.* CRC Press, 2002.

[62] AR Pries, TW Secomb, and P Gaehtgens. Biophysical aspects of blood flow in the microvasculature. *Cardiovascular research*, 32(4):654–667, 1996.

[63] Jean-Jacques E Slotine, Weiping Li, et al. *Applied nonlinear control*, volume 199. Prentice-hall Englewood Cliffs, NJ, 1991.

[64] Mark W Spong, Seth Hutchinson, and Mathukumalli Vidyasagar. *Robot modeling and control*, volume 3. Wiley New York, 2006.

[65] CY Su, TP Leung, and QJ Zhou. A novel variable structure control scheme for robot trajectory control. *Proc. IFAC Triennial World Congr*, 5:117–120, 1990.

[66] Samer Tamaz, Richard Gourdeau, Arnaud Chanu, Jean-Baptiste Mathieu, and Sylvain Martel. Real-time mri-based control of a ferromagnetic core for endovascular navigation. *Biomedical Engineering, IEEE Transactions on*, 55(7):1854–1863, 2008.

[67] Martin Uecker, Shuo Zhang, Dirk Voit, Alexander Karaus, Klaus-Dietmar Merboldt, and Jens Frahm. Real-time mri at a resolution of 20 ms. *NMR in Biomedicine*, 23(8):986–994, 2010.

[68] Kathryn E Uhrich, Scott M Cannizzaro, Robert S Langer, and Kevin M Shakesheff. Polymeric systems for controlled drug release. *Chemical reviews*, 99(11):3181–3198, 1999.

[69] Ajay Ummat, Atul Dubey, and Constantinos Mavroidis. Bionanorobotics: a field inspired by nature. *Bar Cohen, Biommetics: Biologically Inspired Technologies DK3163 c007*, pages 2001–226, 2005.

[70] Vadim I Utkin. *Sliding modes in control and optimization.* Springer Science & Business Media, 2013.

[71] Panagiotis Vartholomeos, Matthieu Fruchard, Antoine Ferreira, and Constantinos Mavroidis. Mri-guided nanorobotic systems for therapeutic and diagnostic applications. *Annual Review of Biomedical Engineering*, 13:157–184, 2011.

[72] Sethu Vijayakumar, Aaron D'souza, and Stefan Schaal. Incremental online learning in high dimensions. *Neural computation*, 17(12):2602–2634, 2005.

[73] Sethu Vijayakumar and Stefan Schaal. Locally weighted projection regression: An o (n) algorithm for incremental real time learning in high dimensional space. In *International conference on machine learning, proceedings of the sixteenth conference*, 2000.

[74] Rong-Jong Wai. Fuzzy sliding-mode control using adaptive tuning technique. *Industrial Electronics, IEEE Transactions on*, 54(1):586–594, 2007.

[75] Paul J Werbos. Approximate dynamic programming for real-time control and neural modeling. *Handbook of intelligent control: Neural, fuzzy, and adaptive approaches*, 15:493–525, 1992.

[76] FM White. Viscous fluid flow, 1991. *MacGraw, New York*, pages 335–393, 1991.

[77] Yuqiang Wu, Xinghuo Yu, and Zhihong Man. Terminal sliding mode control design for uncertain dynamic systems. *Systems & Control Letters*, 34(5):281–287, 1998.

[78] Rong Xu. *Optimal sliding mode control and stabilization of underactuated systems.* PhD thesis, The Ohio State University, 2007.

[79] Rong Xu and U. Ozguner. Optimal sliding mode control for linear systems. In *Variable Structure Systems, 2006. VSS'06. International Workshop on*, pages 143–148, June 2006.

[80] Liang Yang and Jianying Yang. Nonsingular fast terminal sliding-mode control for nonlinear dynamical systems. *International Journal of Robust and Nonlinear Control*, 21(16):1865–1879, 2011.

[81] K Berk Yesin, Karl Vollmers, and Bradley J Nelson. Modeling and control of untethered biomicrorobots in a fluidic environment using electromagnetic fields. *The International Journal of Robotics Research*, 25(5-6):527–536, 2006.

[82] K David Young and Ü Özgüner. Co-states for sliding mode design in linear systems. *Systems & control letters*, 27(4):233–242, 1996.

[83] K David Young, Vadim I Utkin, and Umit Ozguner. A control engineer's guide to sliding mode control. *IEEE transactions on control systems technology*, 7(3):328–342, 1999.

[84] Kar-Keung Young, P. Kokotovic, and V. Utkin. A singular perturbation analysis of high-gain feedback systems. *Automatic Control, IEEE Transactions on*, 22(6):931–938, Dec 1977.

[85] Shuanghe Yu, Xinghuo Yu, Bijan Shirinzadeh, and Zhihong Man. Continuous finite-time control for robotic manipulators with terminal sliding mode. *Automatica*, 41(11):1957–1964, 2005.

[86] X Yu and Z Man. Fast terminal sliding mode control for single input systems. In *Proceedings of 2000 Asian control conference, Shanghai, China*, 2000.

[87] Xinghuo Yu and Man Zhihong. On finite time mechanism: Terminal sliding modes. In *Variable Structure Systems, 1996. VSS'96. Proceedings., 1996 IEEE International Workshop on*, pages 164–167. IEEE, 1996.

[88] Xinghuo Yu and Man Zhihong. Fast terminal sliding-mode control design for nonlinear dynamical systems. *IEEE Transaction on Circuits and Systems^{2}I: Fundemental Theory and Applications*, 49(2), 2002.

[89] Shuo Zhang, Nikolaus Gersdorff, and Jens Frahm. Real-time magnetic resonance imaging of temporomandibular joint dynamics. 2011.

[90] Man Zhihong, AP Paplinski, and HR Wu. A robust mimo terminal sliding mode control scheme for rigid robotic manipulators. *Automatic Control, IEEE Transactions on*, 39(12):2464–2469, 1994.

[91] Man Zhihong and Xing Huo Yu. Terminal sliding mode control of mimo linear systems. In *Decision and Control, 1996., Proceedings of the 35th IEEE Conference on*, volume 4, pages 4619–4624. IEEE, 1996.